THE HONG KONG POLYTECHNIC UNIVERSITY
香港理工大學

DEPARTMENT OF MECHANICAL ENGINEERING

Prediction of Noise Generation by using Modeled Boltzmann Equation (BE)

Kam Wing Sze Elizabeth

A thesis submitted in partial fulfilment of the requirements for the Degree of Doctor of Philosophy

October 2007

Certificate of originality

I hereby declare that this thesis is my own work and that, to the best of my knowledge and belief, it reproduces no material previously published or written, nor material that has been accepted for the award of any other degree or diploma, except where due acknowledgement has been made in the text.

Kam Wing Sze Elizabeth

Abstract

One-step CAA methods aim at resolving the flow and the acoustic fields simultaneously. A set of unsteady compressible Navier-Stokes (NS) Equations are solved in order to capture both the sound generated mechanism and the fluid-sound interaction at the near field. The physical challenge of aeroacoustics simulation comes from the disparity of aerodynamic and acoustic scales. Since the smaller acoustic scale has to be taken account for throughout the simulation, it is computational costly to solve the nonlinear NS Equations. As a result, the direct methods, although accurate, are limited to simple cases.

Instead of solving a set of nonlinear NS equations, the particle distribution function is being tracked by solving the Modeled BE with BGK model. The desirable macroscopic properties in both the aerodynamic and acoustic scales can be obtained by taking moment of the particle distribution function.

The accuracy and robustness of Modeled BE for CAA studies depends on

1. An appropriate non-reflecting boundary conditions for aeroacoustics simulations
2. The ability and extent of the Modeled BE to recover the unsteady compressible NS equations (Recovery of transport coefficients in macroscopic equations)

In this thesis, the Modeled Boltzmann Equation (BE) as a One-Step Computational Aeroacoustics (CAA) method has been studied and analyzed with respect to the above aspects.

First of all, an appropriate non-reflecting boundary condition is crucial for CAA studies, since the rebound waves from boundaries would contaminate the computational domain and drive the solutions to a non-physical one. In this thesis, different types of non-reflecting boundary conditions are studied and compared, with respect to two benchmarked aeroacoustics problems.

Physically, the particle distribution function in the Boltzmann Equation can be expanded to recover the unsteady compressible NS equations via Chapman-Enskog procedure. However, there exist limitations on application by using different numerical schemes. The corresponding limitations are analyzed in the first aspect.

The macroscopic transport coefficients are closely related to the relaxation of particle collision. Therefore, the transport coefficients should be recovered by physical laws via the relaxation of particle collision. The first coefficient of viscosity related to momentum relaxation has been recovered by Sutherland's Law by Li et al. (2006). In this thesis, the coefficient of thermal conductivity is recovered by Eucken's model, with respect to the energy relaxation. Case studies of aeroacoustics problems with thermal effect are presented accordingly.

Publications Arising from the Thesis

1. Kam, E. W. S., Li, X. M., Leung, R. C. K., and So, R. M. C., "Development of Non-Reflecting Boundary Condition for One Step LBM Aeroacoustics Simulation," Book of Abstracts of the Second International Conference for Mesoscopic Methods in Engineering and Science, Hong Kong, 2005, p. 66.

2. Kam, E. W. S., Leung, R. C. K., and So, R. M. C., "Non-Reflecting Boundary Conditions for One-Step LBM Simulation of Aeroacoustics," The Twelfth AIAA/CEAS Aeroacoustics Conference (Twenty Seventh AIAA Aeroacoustics Conference), Cambridge, Massachusetts, U.S.A., 2006, Paper No. 2006-2416.

3. Leung, R. C. K., So, R. M. C., Kam, E. W. S. and Li. X. M.," An Attempt to Calculate Acoustic Directivity Using LBM," The Twelfth AIAA/CEAS Aeroacoustics Conference (Twenty Seventh AIAA Aeroacoustics Conference), Cambridge, Massachusetts, U.S.A., 2006, Paper No. 2006-2574.

4. Leung, R. C. K., Kam, E. W. S. and So, R. M. C., "Recovery of Transport Coefficients in Navier-Stokes Equations from Modeled Boltzmann Equation," AIAA Journal, Vol. 45, No. 4, 2007, pp. 737-739.

5. Kam, E. W. S., Leung, R. C. K. and So, R. M. C., "Lattice Boltzmann Method Simulation of Aeroacoustics and Non-reflecting Boundary Conditions," AIAA Journal, Vol. 45, No. 7, 2007, pp. 1703-1712.

6. Kam, E. W. S., Leung, R. C. K., So, R. M. C. and Li, X. M., "A Lattice Boltzmann Method for Computation of Aeroacoustic Interaction," International Journal of Modern Physics C, Vol. 18, No. 4, 2007, pp. 463-472.

Acknowledgement

I would like to express my gratitude to my two academic supervisors, Dr. LEUNG, C K Randolph (Chief supervisor) and Prof. SO, M C Ronald (Co-supervisor). The completion of my PhD thesis within such a short official time frame is not owe to a miracle, but to their patience, continuing guidance and encouragement in every stage in my PhD studies. I am grateful to Dr. Leung who supervised me with enthusiasm. On the other hand, I would never forget those innovative ideas and advices on research as well as the interesting stories and adventures in life from Prof. So.

Special thanks to "Research Student Attachment Program" organized by the Hong Kong Polytechnic University and Prof. So, who introduced to me a cutting-edge research group in Department of Mathematics, Florida State University (FSU), leaded by Prof. TAM, K W Christopher. I gratefully acknowledge Prof. Tam for his patient guidance and inspiring advice on the thermal acoustic scattering problem and the computing resources from the Department of Mathematics, FSU. During my research visit to FSU, the constructive conversation and useful advice by Dr. PASTOUCHENKO, Nikolai and Dr. JU, Hongbin has made the journey to FSU fruitful and unforgettable.

I am indebted to Prof. XU, Kun for his striking advice as well as his inspiring lectures on gas-kinetic scheme. His generosity on sharing his knowledge and insight on research is gratefully acknowledged.

Here I would also like to express my gratefulness to Prof. XIANG, Yang and Prof. ZHANG, Zhaoqing for their impressive lectures during my PhD studies.

I would like to thank Prof. LESCHZINER, Michael A for his friendship and encouragement. The conversation with him impressed me a lot and gave me courage to explore and take challenges in my life.

Apart from the above, I would like to thank my true friends, Mac and Dr. CHEN, Lu, and my sister Liza for their caring, support and encouragement whenever I am in need.

Here I would like to take this chance to express my deepest gratitude to my mother, as well as my father in heaven. Without their endless love and support in every aspect, this thesis would never be accomplished.

Finally, funding support from the Research Grants Council of the Government of the Hong Kong Special Administrative Region given under Grant Nos. PolyU5174/02E, PolyU5303/03E, and PolyU1/02C is gratefully acknowledged.

Table of Content

List of Tables

List of Figures

Chapter 1

Introduction

1.1 Background

Reduction of noise has been an important issue in engineering design in transportation and many other industries. Active research in computational aeroacoustics (CAA) has been promoted in order to meet the increasingly stringent noise regulations, as well as to advance noise reduction and its associated technology.

Numerical prediction of noise radiation associated with unsteady fluid flows involves capturing of waves in both aerodynamic and acoustic scales. Two major approaches to tackle aeroacoustic problems are commonly used; namely, hybrid or two-step method and direct aeroacoustic simulation (DAS) or one-step method (Colonius and Lele 2004).

Hybrid method resolves the unsteady compressible flow and the radiated sound field in two steps (Colonius and Lele 1993). In the first step, the unsteady aerodynamic field is either computed by a direct numerical simulation (DNS) scheme or by a large eddy simulation (LES) method. The solution is then treated as the source term for noise propagation prediction in the second step. The noise calculation in the far field is usually achieved by invoking Lighthill's acoustic analogy (Lighthill 1952) or its derivative (Ffowcs Williams and Hawkings 1969), or by solving the linearized Euler equation (LEE) (Bogey, Baily and Juvé 2002), or by using the acoustic/viscous decomposition techniques (Jardin and Pope 1994; Shen and Sorensen 1999). Noise thus generated in the far field can be calculated;

however, the interaction between fluid flow and the acoustic disturbances in the near field could not be resolved by any of these hybrid methods. As a result, the noise calculated in the far field might not be exactly correct in terms of the frequency contents and this could give incorrect information for the design of noise control methodologies.

On the other hand, a DNS scheme has been developed for a one-step method (Lele 1992; Colonius and Lele 2004). The method solves a set of nonlinear unsteady compressible Navier-Stokes (NS) equations using a sixth-order finite-difference scheme; therefore, it is capable of capturing both the aerodynamic and acoustic disturbance fields. Consequently, the scheme is able to calculate the sound generated mechanism and the fluid-sound interaction in the near field. However, computational accuracy and disparity of aerodynamic and acoustic scales require fine meshes, and long running time with small time steps. Large computational cost thus results from solving a mixed set of scalar, vector and tensor equations involved in a DNS scheme with demanding spatial and temporal discretization. Therefore, DNS scheme is limited to problems with relatively simple flow configurations and is not entirely suitable for calculating aeroacoustics problems involving complicated flows and/or geometries.

In order to extend the direct methods to study more complicated aeroacoustics problems, it is necessary to ease or eliminate the burdens of numeric accompanied by the solution of a full set of Euler or NS Equations. In view of this, recent effort has been focused on introducing an alternative numerical scheme for CAA studies. This scheme is based on solving a

modeled Boltzmann Equation (BE) which only involves one single scalar equation, as compared to a set of six scalar, vector and tensor equations in the case of a three-dimensional flow.

1.2 Introduction to Modeled Boltzmann Equation (BE)

The Boltzmann Equation describes the time evolution of mesoscopic particle velocity distribution function, $f(x,\xi,t)$, in a continuous velocity space (also known as phase space), through the motion of particles composed of free streaming and collision between particles (Harris 1971). The macroscopic physical properties, such as density, momentum, kinetic and internal energy, energy flux, etc. can be retrieved by integrating the moments of f over the particle velocity space.

The dimensional continuous form of the BE without external body force is given by

$$\frac{\partial f}{\partial t} + \boldsymbol{\xi} \cdot \nabla f = Q(f, f) \quad , \tag{1.1}$$

where t is time, $\boldsymbol{\xi}$ is the particle velocity vector and Q is the collision integral defined as

$$Q(f, f) = \int d^3\boldsymbol{\xi} \int d\Omega \sigma(\Omega) |\boldsymbol{\xi} - \boldsymbol{\xi}_*| \left[f(\boldsymbol{\xi}') f(\boldsymbol{\xi}_*') - f(\boldsymbol{\xi}) f(\boldsymbol{\xi}_*) \right] \quad , \tag{1.2}$$

Bold letters are used to denote vectors, and the integral is performed over the whole particle velocity space. Streaming of particles is accounted for by the left hand side, while $Q(f, f)$ on the right hand side represents a two-body particle collision integral. The complicated mathematical structure of $Q(f, f)$ makes it very difficult to resolve, thus rendering a direct solution of Eq. (1.1)

extremely difficult, if not impossible. Therefore, attempts have been made to simplify the collision term and that leads to a modeled BE. The rationale for the simplification is based on the disparity of timescale between evolution of f and the corresponding changes in macroscopic properties. Since the BE has a much smaller timescale than the NS Equations, it is possible to assume that the macroscopic properties is insensitive to individual collisions between particles and deviation of gas particles from their local equilibrium state is sufficiently small (Bhatnagar, Gross and Krook 1954). Under these assumptions, Bhatnagar, Gross and Krook (1954) proposed a simple model for Q and the resulting equation is widely known as the BE with a BGK-type model (Cercignani 1988).

1.2.1 Governing equation of modeled BE and its connection to macroscopic properties

The dimensionless form of the modeled BE is given by

$$\frac{\partial f}{\partial t} + \boldsymbol{\xi} \cdot \nabla f = -\frac{1}{\tau}\left(f - f^{eq}\right), \tag{1.3}$$

where τ is the time taken for f to relax from non-equilibrium to a Maxwellian-Boltzmann equilibrium state f^{eq}. All variables in Eq. (1.3) are appropriately normalized using relevant characteristics length, velocity and time scales. The collision integral, $Q(f, f)$, is represented by the simple BGK model given by $-\frac{1}{\tau}\left(f - f^{eq}\right)$. The macroscopic measurable properties are connected to the mesoscopic variable via the integrals of the moments of f or f^{eq} over the velocity space.

Similar to the continuous BE, the macroscopic conservation equations can be derived from the BGK-type modeled BE (hereafter simply stated as modeled BE in this thesis) by introducing five collision invariants φ_α $(\alpha = 0,1,2,3,4)$, $\varphi_0 = 1; \varphi_{1,2,3} = \xi; \varphi_4 = \xi^2$ (Cercignani 1988). The modeled BE is multiplied by φ_α and then integrated over the velocity space. Five equations of the macroscopic hydrodynamic theory for mass, momentum and energy conservation are obtained with thirteen variables. In this case, the hydrodynamic description deduced from the modeled BE is not self-contained (Harris 1971). The equations are then closed by invoking different assumptions that lead to the Euler or NS Equations. To achieve this, a standard multi-scale Chapman-Enskog expansion is undertaken (Chapman 1916, 1918; Enskog 1917), in which both spatial and temporal dimensions are rescaled with a small Knudsen number, ε.

With this modeled BE, albeit improved from the original BGK-type modeled BE, there still exist certain shortcomings which prohibit its application to meaningful physical problems.

First of all, τ, being regarded as the relaxation time of particle to relax to its equilibrium state after collision, should vary with the molecular velocity which is related directly to the temperature. According to the kinetic theory of gas, τ is physically important if a correct derivation of the transport coefficients, such as the first and second coefficient of viscosity, μ and λ, and the thermal conductivity, κ, were to be realized. However, it was made constant locally in the BGK model. Secondly, the Prandtl number Pr thus derived was found to have the value $Pr = 1$ which mismatches with both the

true BE and the experimental data for real gas ($Pr = 2/3$ for monatomic gas and $Pr = 5/7$ for diatomic gas). Thus modeled, the BE still cannot be solved analytically; it needs to be solved numerically. Various numerical schemes are available and a few of the more relevant schemes are discussed below.

1.2.2 Different numerical schemes for modeled BE

Two different types of numerical schemes are available for the solution of the modeled BE. They are of slightly different character; one is known as the gas-kinetic scheme and the other is based on particle velocity lattice. The latter scheme is commonly known as the lattice Boltzmann method (LBM). These two schemes have been proposed as alternatives to conventional computational fluid dynamics (CFD) methods where the full Euler or NS equations are solved. These two different numerical schemes used to solve the modeled BE are briefly discussed below in order to identify an appropriate scheme for the present study.

1.2.2.1 Gas-kinetic scheme

Based on the gas-kinetic theory for compressible flow simulations, gas-kinetic scheme has drawn much attention in the shock capturing community in the past few decades. Originally, many numerical schemes were developed by solving the collisionless Boltzmann Equation (Pullin 1980; Mandal and Deshpande 1994). Artificial "collisions" were added to reduce the numerical dissipations in these numerical schemes. Xu (1993) proposed a new gas-kinetic scheme (named as BGK scheme) by solving the modeled BE with a BGK-type model. Numerical fluxes on cell interfaces were calculated

by a finite volume method. Since particle collisions during the gas evolution stage are included in Xu's scheme, the entropy condition across shock is satisfied automatically in the relaxation process of the particle distribution function from non-equilibrium to an equilibrium state.

Recently, the BGK-type scheme has been extended to study low Mach number viscous flows (Su, Xu and Ghidaoui 1999). A two-dimensional lid-driven cavity flow was studied and the results were in good agreement with Ghia's experimental data (1982).

1.2.2.2 Lattice Boltzmann method (LBM)

According to Wolf-Gladrow (2000), in general, the LBM is regarded as an extension of lattice gas automata (LGA) or lattice gas cellular automata (LGCA). In LBM, the modeled BE invoking either the BGK-type model or its variant is solved. Therefore, the tracking of an individual particle motion and particle-particle collisions as in LGA or LGCA is replaced by a single-particle distribution function as in the BGK-type modeled BE (McNamara and Zanetti 1988). More than a decade ago, LBM has been proposed as an alternative to CFD techniques (Chen and Doolen 1998). It has been developed to study a variety of CFD problems. For example, LBM is proposed to study single component hydrodynamics, multiphase and multi-component flows, flows through porous media, micro-flows, reaction-diffusion systems and particulate suspensions in fluid, etc (Succi 2001).

On the other hand, LBM with discrete lattice velocities can be obtained from the modeled BE. By expanding the Maxwellian-Boltzmann

equilibrium distribution function, f^{eq} with low Mach number approximation (He and Luo 1997, Abe 1997), the corresponding discrete lattice velocities can be calculated. Apart from the low Mach number approximation, the discrete lattice velocities are directly related to a fixed speed of sound according to the lattice model being proposed. The rationale behind is that the true macroscopic hydrodynamic conditions have to be well represented by the selected lattice velocities. In kinetic theory of gases, sound must be transmitted by the motions of individual particles with the same order of magnitude as that of the mean speed of particles (Chapman and Cowling 1970).

Being a simplified version of the modeled BE, the conventional LBM is able to recover the NS Equations in the asymptotic limit of Knudsen number going to zero, i.e., the dense gas assumption (Chen, Chen and Maatthaeus 1992; Qian, d'Humières and Lallemand 1992; Frisch, Hasslacher and Pomeau 1986; Frisch, d'Humières, Hasslacher, Lallemand and Pomeau 1987). Consequently, LBM is confined to low Mach number flows within the incompressible limit and isothermal flows, due to the expansion of f^{eq} in LBM and the fixed speed of sound selected for the lattice model.

Attempts have been made to relax the thermal constraint. For example, Sun (1998) introduced a prescribed potential energy term to retrieve an arbitrary specific heat ratio, γ, for a perfect gas locally for a fluid particle while τ was fixed to unity in the calculation. On the other hand, Palmer and Rector (2000) modeled the internal energy as a scalar field by using a second distribution function to incorporate the thermal effect, while treating τ as a

numerical parameter and its physical implication was not accounted for. Tsutahara et al. (2002) and Kang et al. (2003) included the particle rotational degree of freedom in calculating the specific heat ratio, γ. However, a numerical parameter, the relaxation time factor, φ, was introduced into the μ, λ and κ calculation, while the physical significance of τ was not explicitly addressed.

Recently, the LBM has been modified and extended to deal with DAS problems. Li et al. (2006) adopted the finite difference LBM for aeroacoustics simulations. Unlike the conventional LBM, time step of the finite difference LBM (Reider and Sterling 1995) was independent of the lattice size, as node-to-node movement of particles in conventional LBM was no longer a requirement for the finite difference LBM. Also, Li et al. (2006) incorporated several remedies in the proposed LBM model. Firstly, by introducing a two-relaxation-time model, the first coefficient of viscosity, μ was correctly recovered by using the Sutherland Law as an additional constraint. Thus modified, the dependence of μ on temperature is correctly modeled. Secondly, the equation of state was explicitly recovered through a redefinition of internal energy by invoking a collision model that considers rotational degree-of-freedom as well as the translational degree-of-freedom assumed in the BGK-type model. As a result, γ is found to depend on the translational and rotational degree-of-freedom only and not on the dimensions of the problem as the traditional BGK model would give. This formulation gives a γ = 1.4 exactly for diatomic gas. Three cases were selected to validate the one-step LBM aeroacoustics simulation; they were the one-dimensional acoustic

pulse propagation, the circular acoustic pulse propagation, and the propagation of acoustic, vorticity and entropy pulses in a uniform stream. It was shown that the modified LBM gave identical results as those obtained from the solution of the NS equations using DNS.

1.3 Problems Facing Modeled BE in DAS Studies

In spite of Li et al.'s improvement (2006) on the LBM for DAS studies, there still exist important hurdles on extending the modeled BE to tackle DAS problems. Some of these hurdles are high speed flow, thermal acoustics and other flow complexities, and open and wall boundaries. In numerical aeroacoustics simulations involving open boundaries, quite often truncated computational boundaries have to be implemented in order that the simulations can be carried out in finite computational domain that is of a manageable size. Thus nonreflecting boundary conditions are required at these boundaries if the internal acoustics field were not to be contaminated by spurious reflected waves at the computational boundaries. Conventional nonreflecting boundary conditions used in the solution of the Euler or NS equations are not necessarily applicable to the solution of the particle distribution function f (Poinsot and Lele 1992; Colonius, Lele and Moin 1993; Ta'asan and Nark 1995; Freund 1997; Kim and Lee 2000; Hu 2001). Further, in spite of several nonreflecting boundary conditions being proposed for the LBM (Chen, Martinez and Mei 1996; Maier, Bernard and Grunau 1996; Yu, Mei and Shyy 2005), their suitability for the current modified LBM needs to be investigated. It is not feasible to tackle all problems associated with the use of LBM for DAS within the limited time frame of this thesis work,

therefore, a choice has to be made on the more relevant issues to be treated first. In the present study, it is deemed more appropriate to examine the nonreflecting boundary conditions for *f* and to extend the formulation of Li et al. (2006) to include the thermal effect in the calculation of aeroacoustics.

1.3.1 Non-reflecting boundary conditions (NRBC) for CAA studies

Most aeroacoustic simulation problems are concerned with open boundaries. In reality, the aerodynamic and acoustic disturbances propagate to infinity. However, it is necessary to invoke truncated boundaries for numerical simulations, due to limited computational resources. The artificial or computational boundaries, in this case, should allow both aerodynamic and acoustic waves passing through with minimal reflection. Otherwise, the spurious erroneous waves reflecting from the computational boundaries could contaminate the numerical simulations, decrease the computational accuracy and might even drive the solutions towards a wrong time-stationary state. Consequently, nonreflecting boundary conditions (NRBC) are required for DAS be it carried out by LBM or DNS schemes.

Numerous attempts have been made to develop NRBC for DNS scheme. The classical 1-D nonreflecting characteristics-based boundary condition (NSCBC) is the most widely used because of its simplicity. Different NSCBC schemes have been proposed (Roe 1986, Giles 1990, Poinsot and Lele 1992, Colonius, Lele and Moin 1993, Kim and Lee 2000). Another NRBC is the absorbing boundary conditions (ABC) (Engquist and Majda 1977, Ta'asan and Nark 1995, Freund 1997). A convective term was added to the linear Euler equations, thereby forcing the solution to become

supersonic at the border of the computational domain (Ta'asan and Nark 1995). An alternative proposal was to recast the Navier–Stokes equations with additional damping terms so that all flow unsteadiness were suppressed and the flow was forced towards a prescribed uniform flow in a buffer zone beyond the physical or computational domain (Freund 1997). This proposal has one drawback though, because it requires an a priori knowledge of the outlet flow. Others not as commonly used boundary treatment methods include the filtering method (FM) applied to the whole spatial field (Gaitonde and Visbal 1999, 2001), the perfectly matched layer (PML) method (Hu 2001), and the $C1$ continuity preservation method (Loh 2003, Loh and Jorgenson 2005). All these methods are successful for some types of problems and are less so for others.

Similar to DNS schemes, NRBC for open boundaries have to be formulated for LBM. All the boundary treatment schemes mentioned in the preceding paragraphs have been applied to DNS calculations only; few have been extended to LBM. Instead, extrapolation method (EM) is applied to the zeroth or first order of f by Li et al. (2006). In the study of Tsutahara et al. (2002), a prescribed boundary condition is specified for the density, but no details on implementation have been given. On the other hand, Kang et al. (2003) stipulates NSCBC boundary conditions along the line of Poinsot and Lele (1992). Again, no details were provided on how to implement the NSCBC.

The improved LBM (Li et al. 2006) with zero f gradients (ZFG) assumed at open boundaries was used to simulate three benchmark

aeroacoustic problems. Its computational accuracy was established by comparing the results of the three benchmark simulations with those obtained from DNS. In the DNS calculations, the errors arising from reflection at the boundaries were minimized by adopting a relatively large domain with damping region in the simulation. The results show that the LBM calculations (Li et al. 2006) with a smaller domain are just as accurate as those obtained using DNS with a larger computational domain. However, their study did not examine the merits of other types of NRBC; therefore, the relative merits and accuracy of the respective boundary treatments on LBM aeroacoustic simulations need further investigation.

1.3.2 Incapability of revealing correct thermal effect

The macroscopic transport coefficients such as the first and second coefficient of viscosity, μ and λ, and also the coefficient of thermal conductivity, κ, are specified in the solution of the NS Equations. However, in the kinetic theory of gases, these coefficients are part of the solution of the modeled BE. In order to extend the modeled BE to study DAS problems, it is necessary to modify the equation so that it can fully recover the complete set of compressible NS equations, that is, the mass, momentum and energy conservation equations with the correct transport coefficients, and the gas equation of state.

As mentioned in the previous section, in the BGK-type model, recovery of the Euler or NS equations, the Prandtl number, $\mathrm{Pr} = \mu c_P / \kappa = 1$, is inherent in the formulation even when the first coefficient of viscosity, μ is

correctly recovered. This incorrect value of *Pr* implies that the thermal energy exchange between particles has not been replicated properly and the Li et al. (2006) modified BGK model needs further improvement to account for the thermal energy exchange during the collision process.

The incorrect value of Pr could be traced to the single-relaxation-time (SRT) model invoked in the modeled BE. Under this model, the additional time required for the relaxation of thermal energy after collision is neglected. In view of this, numerous attempts have been made to extend LBM to solve thermal problems based on a multi-speed model. Alexander (1993) proposed a 2-D thermal LBM for monatomic gas. However, the resulting Pr obtained has a value of 1/2 which is inconsistent with real gas. Chen et al. (1994) employed a higher-order velocity expansion for f^{eq} to correct the viscous stress and the heat flux; however, details of the Pr correction were not mentioned. Multi-speed models proposed by McNamara et al. (1995) and Teixeira el al. (2000) allowed variation of Pr, while it is numerically unstable due to the violation of a global H-theroem (Chen et al. 2000). Lallemand et al. (2003) decoupled the shear and energy modes of the linearized evolution operator to improve the numerical stability, while physical background of the modification was not highlighted. A passive scalar approach by Shan (1997) introduced an additional distribution function to solve the energy equation separately. However, a much higher computational cost is required for this thermal LBM model in comparison with the isothermal one.

So far much attention has been given to numerical treatment on thermal LBM rather than to recognize the physical significance of a correct

deviation of Pr for a diatomic gas. This thesis proposes to examine the possibility of putting forward a physical model to recover a correct Pr for the finite difference LBM proposed by Li et al. (2006).

The associated wall boundary conditions for thermal LBM also require further consideration. No-slip boundary conditions are implemented in conventional LBM (isothermal) schemes via the bounce-back rule (Wolfram 1986, Cornubert et al. 1991) or more elaborated methods based on the bounce-back rule (Ziegler 1993, Skordos 1993, Noble et al. 1995, Inamuro et al. 1995, Maier et al. 1996, Zou and He 1997) were adopted. The possibility of extending these wall boundary conditions methods to thermal LBM has not been examined. Further, it has been shown that most of these proposed methods are of first- or second-order accuracy for the conventional LBM. Improvement in accuracy is necessary if the proposed methods were to be useful in any finite difference LBM schemes (an example is the scheme of Li et al. 2006) for aeroacoustics studies.

1.4 Objectives of the Present Thesis

From the discussion above, it is now clear what the objectives of this thesis should be. This thesis aims to extend the modeled BE to simulate aeroacoustics problems in a more complete manner. This involves finding appropriate nonreflecting boundary conditions for the modeled BE and to extend the work of Li et al. (2006) to further recover the thermal conductivity correctly. Therefore, there are two objectives in this thesis.

Firstly, non-reflecting boundary conditions (NRBC) are proposed and formulated for the modeled BE, based on viable NRBC for DNS schemes.

Among all schemes examined, the extrapolation method (EM) is applied to the distribution function or its derivative; the C^1 continuity preservation method and the absorbing boundary conditions (ABC) are also extended to Li et al.'s improved LBM for investigation. Two cases are selected to validate the proposed NRBC. They are the one-dimensional acoustic pulse propagation and the propagation of acoustic, vorticity and entropy pulses in a uniform stream.

Secondly, a physical model is proposed to recover the thermal conductivity, κ, based on a multiple-relaxation-time approach. Based on Eucken's theory of heat conduction, the correct value of Prandtl number, $Pr \approx 0.71$, is retrieved. Since μ and γ have been replicated (Li et al. 2006), a complete set of compressible NS Equations with correct transport coefficients can be fully recovered. The Eucken's model is applied to the improved LBM (Li et al. 2006) and the corresponding thermal effect on the three cases considered in their paper is investigated. Furthermore, a thermoacoustic scattering problem is simulated by the gas-kinetic scheme and its result is compared with an analytical solution obtained by solving the governing NS equations.

Once the full set of NS Equations is recovered with correct transport coefficients and an appropriate NRBC is identified, an appropriate modeled BE will be available for the study of practical aeroacoustics problems.

1.5 Outline of the Present Thesis

This thesis is organized as follows:

Chapter 2 outlines the recovery of macroscopic hydrodynamic equations from the modeled BE. Euler and Navier-Stokes (NS) Equations are recovered via first and second order Chapman-Enskog (CE) expansion. Limitation of the recovery of the transport coefficients is explicitly stated. Details of Li et al's (2006) remedy on the recovery of μ by invoking Sutherland Law would be highlighted.

Further to Li et al.'s remedy, recovery of the thermal conductivity for the modeled BE by Eucken's Model would be outlined in Chapter 3. Physical background of thermal energy relaxation in kinetic theory, importance of recovering thermal conductivity for aeroacoustic problems and the derivation of a correct thermal conductivity by Eucken's Model would be stated in details.

In Chapter 4, nonreflecting boundary conditions (NRBC) for DAS studies are proposed and formulated for the modeled BE outlined in Chapter 3. Different types of NRBC would be investigated and applied to Li et al.'s (2006) improved LBM for case study. Results would be compared with DNS solutions.

In Chapter 5, a thermoacoustics scattering problem would be studied analytically by solving the governing linearized Euler equations. Results would be compared with the numerical solution obtained by using gas-kinetic scheme with a corrected thermal conductivity in Chapter 6.

Conclusions and suggestions for possible future development of modeled BE for DAS studies would be outlined in Chapter 7.

Chapter 2

Recovery of Navier-Stokes (NS) Equations by Modeled BE

Under the assumption that a fluid can be regarded as a continuum, a direct aeroacoustic simulation (DAS) problem can be described by macroscopic measurable properties such as density, velocity and pressure, through a set of unsteady Navier-Stokes (NS) Equations. In reality, however, fluid is made up of discrete particles. It can be treated as a continuous medium only because the characteristic length scale of the macroscopic observable quantities is sufficiently large in comparison with the microscopic length scale (or mean free path) of particle motions. Therefore, it is more appropriate to study a DAS problem by considering the modeled BE, in which the time evolution of a more informative function in mesoscopic level, the particle velocity distribution function, $f(x,\xi,t)$, in a continuous velocity space (also known as phase space) is described through the motion of particles composed of free streaming and collision between particles (Harris 1971).

Since the individual motion of particles is not central, in an overall sense, to a solution of an aeroacoustic problem using DAS, it is possible to narrow down the description of f (Harris 1971) such that the macroscopic quantities are connected via integrating moments of f. Eventually, with the connection between f and the macroscopic properties, it is made possible that only one variable, f, is solved in the modeled Boltzmann equation to obtain all the macroscopic information required to describe a DAS problem.

As mentioned in Chapter 1, the macroscopic conservation equations can be derived from the modeled BE, which was commonly represented by the BGK model, by introducing five collision invariants φ_α $(\alpha = 0,1,2,3,4)$, $\varphi_0 = 1; \varphi_{1,2,3} = \xi; \varphi_4 = |\xi|^2$ (Cercignani 1988). Since the resulting laws of conservation are described by thirteen variables in five equations (Harris 1971), the system of equations needs further closure by invoking different assumptions such that the unsteady compressible Euler or NS Equations are obtained. In this case, a standard multi-scale mathematical procedure, the Chapman-Enskog (CE) expansion, is invoked. Under this expansion, both spatial and temporal dimensions are rescaled using a small parameter defined as the ratio of a microscopic to a macroscopic length scale or commonly known as the Knudsen number, ε. It should be pointed out that, by invoking the CE procedure, the unsteady compressible Euler or NS Equations are recovered with basically two limitations which prohibit its application to meaningful physical problems. Improvements or modifications have to be made to relax or eliminate these two limitations, which are elaborated below.

Firstly, the relaxation time, τ, was made constant locally in the BGK model. Physically, it should vary with the molecular velocity which is directly related to the temperature. From the kinetic theory point of view, τ is an important parameter for a correct derivation of the equation of state for a diatomic gas, or the specific heat ratio, γ. Further, it is also important for a correct derivation of the transport coefficients, the first and second coefficient of viscosity μ and λ, and the thermal conductivity, κ. In order to replicate

the correct physics of a DAS problem using a modeled BE, it is necessary that a physical model should be formulated so that τ varies with temperature, thus allowing the transport coefficients, μ and λ, to be recovered correctly.

Secondly, the thermal conductivity, κ, or its dimensionless counterpart Prandtl number, Pr, thus derived was found to give rise to the condition $\mathrm{Pr} = 1$. It is in violation of the true BE as well as the experimental data for real gases. For example, Pr should have a value of $2/3$ for a monatomic gas and 5/7 for a diatomic gas. Physically, the incorrect value of Pr implies that the thermal energy exchange between particles has not been replicated properly. In order to simulate DAS problems correctly, it is necessary that the BGK model improved to replicate γ and μ correctly should be improved to account for the thermal energy exchange during the collision process.

Recently, Li et al. (2006) proposed an improved finite difference Lattice Boltzmann Method (LBM) to solve the modeled BE numerically for DAS problems. In the proposed two-relaxation-time model, the set of unsteady compressible NS Equations for diatomic gas was recovered. In order to accomplish this objective, a rotational degree-of-freedom was considered in addition to the translational degree-of-freedom in particle-particle collisions, and the Sutherland Law was invoked so that τ could be made a function of temperature, and the first coefficient of viscosity, μ, was recovered correctly.

This chapter aims to give a brief description of the recovery of the set of unsteady NS Equations via CE expansion, in which the origin of limitations would be pointed out (Li et al. 2006). Since the ultimate objective is for DAS

studies, Li et al's model (2006) for polyatomic gas will be adopted. Details of Li et al.'s (2006) remedy on the correct recovery of μ by invoking Sutherland Law will also be highlighted. Finally, it serves as a foundation for Chapter 3 where a physical model on the correct recovery of the thermal conductivity, κ, and its corresponding dimensionless number, Pr, will be discussed.

2.1 Governing Equation for the Modeled BE and Macroscopic Properties

As a simplified version of the continuous BE (see Equation 1.1 and 1.2), the dimensionless form of the modeled BE is given by

$$\frac{\partial f}{\partial t} + \boldsymbol{\xi} \cdot \nabla f = -\frac{1}{\tau}\left(f - f^{eq}\right), \tag{2.1}$$

where τ is the time taken for f to relax from a non-equilibrium state to a Maxwellian-Boltzmann equilibrium state f^{eq}. The units of variables in equation (4.1) are as follows:

f, f^{eq} : $kg \cdot (m/s)^{-3} \cdot m^{-3}$

t, τ : s

$\boldsymbol{\xi}$: m/s

∇f : $kg \cdot (m/s)^{-3} \cdot m^{-4}$

The Maxwellian-Boltzmann equilibrium distribution function can be expressed in D spatial dimensions as

$$f^{eq} = \frac{\rho}{(2\pi\theta)^{D/2}} exp\left(-\frac{|\xi - u|^2}{2\theta}\right), \tag{2.2}$$

where $\theta = RT$. All variables in equation (2.1) are appropriately normalized using relevant characteristic length (macroscopic length), velocity (speed of

sound) and time (mean collision interval) scales. The modeled BE is a blurred image of equation (1.1) based on a simpler operator $J(f)$ where $J(f) = -\omega\left(f - f^{eq}\right)$ and the collision frequency is fixed at $\omega = 1/\tau$. In this case, only the qualitative and average properties of the true operator are retained in this equation (Cercignani 1988). This model was initially proposed by Bhatnagar, Gross, and Krook (1954) and was later designated the BGK model. Originally, the BGK model was proposed for a monatomic gas with a single-relaxation-time (SRT) model. It would be shown later that Li et al. (2006) extended the BGK model to diatomic gas, by properly accounting for the rotational degree-of-freedom of molecular motion in the proposed model.

Although the collision integral in equation (1.1) is simplified by the BGK model, f retains its probabilistic definition as that in the continuous BE. It has been defined that the mass density in physical space, ρ, is the integral of the density in the one-particle phase space, f, with respect to all possible velocities (Cercignani 1988) such that

$$\rho = \int f d\boldsymbol{\xi}, \tag{2.3}$$

The mass density is regarded as the zeroth moment of f. The first moment of f, is the macroscopic linear momentum of the gas and is expressed in the following form (the following mathematical expressions in this section are in component form):

$$\rho u_i = \int \xi_i f d\boldsymbol{\xi}, \tag{2.4}$$

where $i = 1, 2, 3$ for a 3-D problem.

The macroscopic internal energy of the fluid is defined by integrating the second moment of f over the particle velocity space. It consists of both kinetic energy of the fluid and the fluid internal energy, e. The definition of the latter needs further consideration if the dynamic motion of the gas particles were to be modeled sufficiently correctly for a diatomic gas. It has been shown in Li et al.'s (2006) model that a correct realization of the diatomic nature of the gas particles hinges on a successful recovery of the equation of state for a perfect gas, which is the key to a correct estimation of the first coefficient of viscosity for DAS studies.

For aeroacoustics computation, the fluid medium of interest is mostly air, which is mainly composed of diatomic nitrogen and oxygen gases. Generally, a polyatomic gas particle can undergo translational motion with D_T degree of freedom, with an additional D_R degree of freedom for its rotational motion. This indicates that both translational and rotational kinetic energies of polyatomic gas particles should be taken into account in a proper definition of the macroscopic internal energy. For diatomic gas like air, the total number of degrees of freedom is $D_T + D_R = 5$ (Woods 1993). From statistical mechanics theory, the kinetic energy should be equally distributed on each degree of freedom. It should be noted that the term, $\frac{1}{2}\int |\boldsymbol{\xi}|^2 f d\boldsymbol{\xi}$, represents the summation of the *translational energy* with D_T degrees of freedom, where $d\boldsymbol{\xi} = d\xi_x d\xi_y d\xi_z$. The kinetic energy on each degree of freedom may be defined as $\frac{1}{D_T}\int \frac{1}{2}|\boldsymbol{\xi}|^2 f d\boldsymbol{\xi}$. Therefore, with the total number

of degrees of freedom given by $D_T + D_R$, the internal energy of the particles can be defined as $\frac{D_T + D_R}{D_T} \int \frac{1}{2} |\boldsymbol{\xi}|^2 f d\boldsymbol{\xi}$, and the second integrating moment of f should give the macroscopic internal energy for the fluid as

$$\rho e + \frac{1}{2} \rho |u|^2 = \frac{D_T + D_R}{D_T} \int \frac{1}{2} |\boldsymbol{\xi}|^2 f d\boldsymbol{\xi}, \tag{2.5}$$

The fluid energy flux can be defined via the third integrating moment of f as follows,

$$\left(\rho e + \frac{1}{2} \rho |u|^2 + p \right) u_i = \frac{D_T + D_R}{D_T} \int \frac{1}{2} \xi_i |\boldsymbol{\xi}|^2 f d\boldsymbol{\xi}, \tag{2.6}$$

Integration of equation (2.5) suggests an explicit internal energy definition $e = (D_T + D_R) RT / 2$ for diatomic gas.

With the moments of f as given in equations (2.3) - (2.6), the Navier-Stokes (NS) equations and the equation of state for a perfect gas could be completely recovered from the modeled BE, i.e., equation (2.1), with the assumption of the BGK collision model and by invoking the Chapman-Enskog expansion (Chapman and Cowling 1970; Li 2006). Details of this derivation can be found in Li (2006); however, for the sake of completeness, a brief description will be given below.

2.2 Recovery of Navier-Stokes Equations via the Chapman-Enskog Expansion

Basically, the Chapman-Enskog procedure involves a direct expansion of the modeled BE for the moment of f (Harris 1971). The solution of the modeled BE is obtained by expanding f as

$$f = f^{eq} + f^{neq} = f^{(0)} + \varepsilon f^{(1)} + \varepsilon^2 f^{(2)} + o\left(\varepsilon^3\right), \tag{2.7}$$

where ε is the Knudsen number and is assumed to be much smaller than one, i.e., $\varepsilon << 1$. The corresponding spatial and temporal dimensions are rescaled as

$$\frac{\partial}{\partial t} = \varepsilon \frac{\partial}{\partial t_1} + \varepsilon^2 \frac{\partial}{\partial t_2}, \tag{2.8a}$$

$$\frac{\partial}{\partial x} = \varepsilon \frac{\partial}{\partial x_1}, \tag{2.8b}$$

Substitute equations (2.7), (2.8) into (2.1) and collecting terms with the same order up to the second order gives

$$o(1): \quad f^{(0)} = f^{eq}, \tag{2.9}$$

$$o(\varepsilon): \quad \frac{\partial f^{(0)}}{\partial t_1} + \xi \cdot \nabla_{x_1} f^{(0)} = -\frac{f^{(1)}}{\tau}, \tag{2.10}$$

$$o\left(\varepsilon^2\right): \quad \frac{\partial f^{(1)}}{\partial t_1} + \frac{\partial f^{(0)}}{\partial t_2} + \xi \cdot \nabla_{x_1} f^{(1)} = -\frac{f^{(2)}}{\tau}, \tag{2.11}$$

Note that the corresponding moments of f are contributed only by the equilibrium part, therefore, substituting equation (2.2) into the moments of f as given in equations (2.3)-(2.6), the resulting moments of f can be expressed as

$$\int f^{eq} d\boldsymbol{\xi} = \rho, \tag{2.12a}$$

$$\int \xi_i f^{eq} d\boldsymbol{\xi} = \rho u_i, \tag{2.12b}$$

$$\frac{D_T + D_R}{D_T} \int \tfrac{1}{2} |\boldsymbol{\xi}|^2 f^{eq} d\boldsymbol{\xi} = \rho e + \frac{1}{2} \rho |u|^2, \tag{2.12c}$$

$$\frac{D_T + D_R}{D_T}\int \tfrac{1}{2}\xi_i|\boldsymbol{\xi}|^2 f^{eq} d\boldsymbol{\xi} = \left(\rho e + \frac{1}{2}\rho|u|^2 + p\right)u_i . \tag{2.12d}$$

With the moments of f as given, the NS Equations can be obtained by multiplying the second-order equations (2.11) with five collision invariants, $\varphi_\alpha \ (\alpha = 0, 1, 2, 3, 4)$ and integrating over the velocity space. The result of this manipulation gives the following continuum conservation equations (Li 2006)

$$\frac{\partial \rho}{\partial t} + \frac{\partial(\rho u_j)}{\partial x_j} = 0 , \tag{2.13a}$$

$$\frac{\partial(\rho u_i)}{\partial t} + \frac{\partial(\rho u_i u_j)}{\partial x_j} = -\frac{\partial}{\partial x_i}\left(\frac{2}{D_T + D_R}\rho e\right) + \frac{\partial}{\partial x_j}\left[\mu\left(\frac{\partial u_j}{\partial x_i} + \frac{\partial u_i}{\partial x_j}\right)\right] + \frac{\partial}{\partial x_i}\left(\lambda \frac{\partial u_k}{\partial x_k}\right) \tag{2.13b}$$

$$\frac{\partial}{\partial t}\left[\rho\left(\tfrac{1}{2}|u|^2 + e\right)\right] + \frac{\partial}{\partial x_i}\left[u_i\left(\tfrac{1}{2}\rho|u|^2 + \rho e + \frac{2\rho e}{D_T + D_R}\right)\right] = \frac{\partial}{\partial x_i}\left(\kappa' \frac{\partial e}{\partial x_i}\right) + \frac{\partial}{\partial x_i}\left[\mu u_j\left(\frac{\partial u_j}{\partial x_i} + \frac{\partial u_i}{\partial x_j}\right)\right] + \frac{\partial}{\partial x_i}\left(\lambda \frac{\partial u_k}{\partial x_k} u_i\right). \tag{2.13c}$$

From equations (2.13b) and (2.13c), the pressure is expressed in the form of $p = 2\rho e/(D_T + D_R)$. The first and second coefficient of viscosity and the thermal diffusivity are defined as

$$\mu = (\gamma - 1)\rho e \tau \quad , \tag{2.14a}$$

$$\lambda = -(\gamma - 1)^2 \rho e \tau \quad , \tag{2.14b}$$

$$\kappa' = \gamma(\gamma - 1)\rho e \tau \quad , \tag{2.14c}$$

respectively, where γ is the specific heat ratio and is defined as $\gamma = (D_T + D_R + 2)/(D_T + D_R)$. By considering the definition of pressure and the specific heat ratio, the equation of state is fulfilled automatically as

$$p = (\gamma - 1)\rho e = \rho RT \,. \tag{2.15}$$

Combining equations (2.14a) and (2.15), the first coefficient of viscosity, μ can be expressed as $\mu = p\tau = \rho RT\tau$. It can be seen from the above derivation that the Prandtl number, $\Pr = \gamma\mu / \kappa'$ is therefore fixed to unity. A physical Eucken's model would be suggested to relax the Prandtl number restriction in the next chapter.

On the other hand, μ, λ and κ' are shown to be directly related to the relaxation time, τ and γ. Since τ is related to γ also and is locally fixed in the BGK model, it implies that the derivation of the transport coefficients are incorrect; therefore, physical models should be proposed to account for the temperature dependence of τ. Once this is successful, the corresponding transport coefficients would also have an appropriate dependence on temperature. Li et al. (2006) invoked the Sutherland law to recover μ correctly. Details of their derivation are briefly described in the following section.

2.3 Recovery of the Correct First Coefficient of Viscosity

As shown in equation (2.1), a single relaxation time is assumed in the modeled BE. According to the kinetic theory of gases, the SRT model adopted in equation (2.1) can be regarded as a rigid sphere model (Ferziger and Kaper 1972). The model assumes molecules as impenetrable billiard balls

with diameter σ, such that the mutual potential energy is given by the following equation

$$\varphi(r)=\begin{cases}\infty & r<\sigma \\ 0 & r>\sigma\end{cases} \quad . \tag{2.16}$$

Despite the simplicity of equation (2.16) in its ability to account for the attractive and repulsive forces among molecules, its Dirac-delta function behaviour leads to an inaccurate prediction of the temperature dependence of the transport and other macroscopic fluid properties. The reason could be attributed to an abrupt change in potential at $r_m \approx \sigma_m$, and the negligence of the long range part of the potential, or the weak potential.

Further, the relaxation time τ associated with the rigid sphere model can be derived as

$$\tau \approx \frac{5}{4}\bar{\tau} = \frac{5}{4}\frac{\bar{\lambda}}{\left|\bar{\xi}\right|} = \frac{5}{4}\frac{1}{\sqrt{2}\pi n\sigma_m^2\left|\bar{\xi}\right|} = \frac{5}{4\sqrt{2}}\left(\frac{1}{\pi n\sigma_m^2\sqrt{\frac{8k_BT}{\pi M_n}}}\right) \quad , \tag{2.17}$$

where $\bar{\lambda}$ is the average mean free path, $\bar{\tau}$ is the average time interval of particle collision and $\left|\bar{\xi}\right| = \sqrt{8k_BT/\pi M_n}$ is the magnitude of the mean particle velocity (n is the particle number density, M_n is the molecular mass, and k_B is the Boltzmann constant). By considering the persistence of velocities after collision in equation (2.17), τ is found to be about $5/4$ times larger than $\bar{\tau}$ and hence gives rise to an expression for μ as

$$\mu = \frac{5}{16\sqrt{\pi}}\frac{1}{\sigma_m^2}\sqrt{M_n k_B T} \quad , \tag{2.18}$$

thus giving a temperature dependence for the first coefficient of viscosity as $\mu \propto \sqrt{T}$. According to Chapman and Cowling (1960), it has been shown that the actual variation of μ is more rapid than that given by equation (2.18) for all gases. In other words, the assumed τ in equation (2.17) is inadequate in recovering the transport coefficients correctly.

In order to account for the temperature dependence of μ more accurately, the rigid sphere model was modified by Sutherland (Ferziger and Kaper 1972), in which the attractive potential was made to obey the power law as follows

$$\varphi(r) = \begin{cases} \infty & r < \sigma \\ C_1(\sigma_m / r_m)^{\nu} & r > \sigma \end{cases} \quad . \tag{2.19}$$

This model shows a correct temperature dependence of μ and can be shown to be given by (Ferziger and Kaper 1972)

$$\mu = \frac{5}{16\sqrt{\pi}} \frac{1}{\sigma_m^2} \frac{\sqrt{M_n k_B T}}{1 + S_0 / T} \approx \left(\frac{T}{T_\infty} \right)^{3/2} \frac{T_\infty / T + S_0 / T}{1 + S_0 / T} \quad , \tag{2.20}$$

where T_∞ is the reference temperature and S_0 is the Sutherland constant. It has been shown that equation (2.20) is followed closely by air (consists mainly nitrogen and oxygen) within the interested temperature range (210K - 1900K) for aeroacoustics problems.

The true relation between the relaxation time and the temperature based on Sutherland's model was developed by Li et al. (2006). In their two-relaxation-time model, an effective relaxation time, τ_{eff} was introduced to substitute for the relaxation time, τ in the modeled BE. The τ_{eff} was made up of a relaxation time τ_1 associated with the repulsive potential for the rigid

sphere and another relaxation time τ_2 associated with the weak attractive potential, which is accounted for by the Sutherland's model. Both relaxation times could be related to temperature T in the following way:

$$\tau_1 \approx \frac{5}{4}\bar{\tau} \propto 1/\sqrt{T} \text{ and } \tau_2 \propto \left|\bar{\xi}\right| \propto \sqrt{T} \quad . \tag{2.21}$$

From the above equation, the relation of τ_1, τ_2 and T can be deduced as $\frac{\tau_1}{\tau_2} \propto \frac{1}{T}$. It was therefore suggested that the effective relaxation time be given by $\tau_{eff} = \frac{\tau_1}{1+\tau_1/\tau_2}$ such that

$$\mu = p\tau_{eff} = p/\left(\frac{1}{\tau_1}+\frac{1}{\tau_2}\right) = \frac{5}{16\sqrt{\pi}}\frac{1}{\sigma_m^2}\frac{\sqrt{M_n k_B T}}{1+\tau_1/\tau_2} \quad , \tag{2.22}$$

Comparing equations (2.20) and (2.22), $\tau_1/\tau_2 = S_0/T$. Thus derived, the temperature dependence of the effective relaxation time, τ_{eff} was explicitly revealed and the first coefficient of viscosity, μ was correctly recovered.

2.4 Summary

In this chapter, an improved modeled BE is introduced for study of DAS problems. The relationship between the mesoscopic distribution function, f, and the macroscopic description of measurable properties such as density, momentum, energy and the energy flux via the moments of f is highlighted. The macroscopic conservation equations can be derived from the modeled BE by introducing five collision invariants φ_α $(\alpha = 0, 1, 2, 3, 4)$, $\varphi_0 = 1; \varphi_{1,2,3} = \xi; \varphi_4 = \left|\xi\right|^2$. The resulting conservation laws are not self-

contained, so that the system of equations is further closed by invoking different assumptions such that the Euler or NS Equations are obtained.

A full set of unsteady compressible NS Equations are obtained by invoking a standard multi-scale mathematical model, and the Chapman-Enskog (CE) expansion in which both spatial and temporal dimensions are rescaled with a small Knudsen number, ε. Since diatomic gas is commonly studied in DAS problems, the recovery of the unsteady compressible NS Equations are based on a diatomic gas model developed by Li et al. (2006). Based on the equipartition theory of energy, the molecular collision properties of the fluid was fully accounted for when the fluid internal energy, e was being considered as a component of the second moment of f.

Two important restriction of the modeled BE is outlined. Firstly, the relaxation time, τ, was made constant locally in the BGK model and its dependence on molecular velocity, thus dependence on temperature, T, was not truly revealed. As a result, the transport coefficients, such as the first and second coefficients of viscosity, μ and λ, and the thermal conductivity, κ were not correctly recovered. This limitation was relaxed by the two-relaxation-time model suggested by Li et al. (2006), in which the Sutherland law was invoked to correctly recovered μ. However, there still exists the second restriction, the incorrect value of Pr. The Prandtl number is fixed at unity which implies that the thermal energy exchange between particles has not been replicated properly. A physical model, the Eucken model, would be invoked in the next chapter to recover a correct value of Pr for diatomic gas.

Chapter 3

Recovery of Thermal Conductivity for Modeled BE by Eucken's Model

As shown in the preceding chapter, it is important to recover the full set of unsteady compressible Navier-Stokes (NS) equations from the modeled BE, as well as the associated transport coefficients correctly, if the true physics of an aeroacoustics problem were to be recovered.

In the solution of the unsteady compressible NS equations, the transport coefficients such as the first and second coefficient of viscosity, μ and λ, and the thermal conductivity, κ are specified, however, they should be part of the solution of the modeled BE via Chapman-Enskog (CE) expansion, as they depend on the relaxation time, τ explicitly. From the macroscopic point of view, the effect of μ is reflected by the Reynolds number, $Re = \rho u L / \mu$, where L is the characteristic length scale of the fluid system; and the effect of κ is reflected by the Prandtl number, $Pr = c_P \mu / \kappa$. In the unsteady compressible NS equations, however, terms associated with the second coefficient of viscosity, that is $\lambda(\partial u_k / \partial x_k)$ are generally small compared to other terms in practical flows (White 1991). Therefore, it would not be considered in the present thesis.

In addition to the Reynolds and Prandtl number, another dimensionless number, the Mach number, $M = u / c$, is also part of the solution of the modeled BE (u is the fluid velocity, c is the speed of sound and is given by $c = \sqrt{\gamma RT}$, where γ is the specific heat ratio, R is the gas constant and T is

the thermodynamic temperature of the gas). As shown in the last chapter, by appropriately considering the molecular dynamics of the fluid, a correct value of γ for diatomic gas, and thus a correct Mach number, can be obtained. Since the Reynolds, Mach, and Prandtl numbers are part of the solution of the modeled BE, their accuracies are important to a correct recovery of the solution of the NS equations from the modeled BE. This is especially true for aeroacoustic and shock-free compressible flow simulations.

In Li et al.'s (2006) two-relaxation-time model, the correct μ dependence on T has been obtained by invoking Sutherland law and the correct value of $\gamma = 1.4$ for diatomic gas has been replicated by considering the translational degree of freedom as well as the rotational degree of freedom of particle collision in the definition of internal energy of the fluid. Thus formulated, it can be shown that $\gamma = (D_T + D_R + 2)/(D_T + D_R)$, which yields $\gamma = 1.4$ correctly for diatomic gas because $D_T = 3$ and $D_R = 2$. In other words, the Reynolds and Mach number thus deduced from the solution of the modeled BE is consistent with that specified in the NS equations for diatomic gas, such as air.

In this chapter, a physical model, the Eucken model, would be invoked to recover a correct value for κ and hence a correct Prandtl number, Pr, for a polyatomic gas would be obtained. A two-relaxation-time approach based on Li et al.'s (2006) model would be adopted. Despite the fact that Li et al. (2006) applied their physical model to a lattice Boltzamann Method (LBM) to solve the modeled BE numerically, the improved modeled BE is based on

fundamental physical consideration and can be solved using different numerical schemes.

3.1 Physical Background of Thermal Energy Relaxation in Kinetic Theory

From the microscopic point of view, the phenomenon of fluid viscosity could be attributed to momentum transfer between gas particles before and after collisions. Similarly, the thermal conductivity can be regarded as the thermal energy transfer from a gas particle to another, when the gas departs slightly from its uniform steady state (represented by the Maxwellian velocity distribution function) due to collisions. All these transport phenomena, or the free-path phenomena (Chapman and Cowling 1970) in non-uniform gases show their tendencies towards uniformity of mass velocity and temperature. In order to relax to equilibrium state after collisions, gas particles have to re-distribute their momentum and thermal energy. Time required for these re-distributions is known as the relaxation time. In other words, both momentum and thermal energy relaxations should be accounted for, if a correct value of relaxation time is to be obtained.

Li et al. (2006) proposed a two-relaxation-time model, where the relaxation time for momentum alone was considered. Three cases were selected to validate the modeled BE where the equation was solved using a lattice Boltzmann numerical scheme. The three cases were the one-dimensional acoustic pulse propagation, the circular acoustic pulse propagation, and the propagation of acoustic, vorticity and entropy pulses in a uniform stream. All cases are without significant temperature gradients and

the thermal effect is therefore negligible. The modified LBM showed identical results as those obtained by solving the NS equations using DNS. However, the thermal energy relaxation was not considered in Li et al.'s (2006) model; consequently, an incorrect value of κ was obtained and the resulting Prandtl number was fixed to unity. In order to study aeroacoustic problems with thermal effect, the thermal energy relaxation should be considered in determining the relaxation time. That is, further improvement on Li et al.'s (2006) model should be carried out.

A classical relation between the thermal conductivity, κ, and the first coefficient of viscosity, μ was suggested by Maxwell (1867), thereafter different molecular models have been established to calculate the correct κ with the formula

$$\kappa = k_1 c_V \mu \quad , \tag{3.1}$$

where k_1 is an unknown to be determined in accordance with different models. For Maxwellian molecule ($\nu = 5$, i.e. repulsive force between molecules varies inversely as the 5th power of the distance), and k_1 equals to 5/2; therefore, $\kappa = 5 c_V \mu / 2$. Although $\nu > 5$ for most polyatominc gases, this value is widely applied for monatomic gas. Based on rigid sphere model for the particles, k_1 can be determined to be

$$k_1 = \left(\frac{5}{2}\right) \frac{1 + \frac{(\nu-5)^2}{4(\nu-1)(11\nu-13)} + \cdots}{1 + \frac{3(\nu-5)^2}{2(\nu-1)(101\nu-113)} + \cdots} \quad , \tag{3.2}$$

where $5 \le \nu < \infty$ (Chapman and Cowling 1970). Therefore, the value of k_1 varies from 2.5 to 2.522 for monatomic gas, and agreed well with

experimental values (Chapman 1916, 1918, Chapman and Cowling 1970). However, the application of the proposed model to equation (3.1) is only valid for monatomic gas, where the rotational energy of diatomic or polyatomic gases was not taken into account for the derivation of the equation.

It was not until Eucken (1913) who took a slightly different approach and proposed a relation linking k_1 to γ that could improve the definition for κ for polyatomic gases. In this approach, contribution of the rotational energy is taken into account to deduce heat flux. Equation (3.1) is re-written as $k_1 = \kappa / c_V \mu$, where k_1 is defined as Eucken's ratio and is denoted by f_E.

Details of Eucken's model for polyatomic gas would be outlined in the next section, with modification made by Woods (1993). The result would be implemented to the two-relaxation-time model proposed by Li et al. (2006), such that a correct thermal conductivity, κ, hence a correct value of Prandtl number would be obtained for the modeled BE.

3.2 Derivation of Correct Thermal Conductivity Using Eucken's Model

In Chapter 2, it has been shown that by introducing an effective relaxation time $\tau_{eff} = \tau_1 / (1 + \tau_1 / \tau_2)$ into the modeled BE, the temperature dependence of τ_{eff} was revealed through the use of the Sutherland Law, hence the first coefficient of viscosity, μ was recovered correctly. In an attempt to further improve the correct recovery of κ, a modification based on Eucken's theory of heat conduction (Chapman and Cowling 1970, Woods 1993) is proposed. The use of Eucken's theory to recover the Fourier law of heat

conduction has been attempted before (Rah and Eu 2001, Eu 2006) and good results were obtained. Eucken (1913) suggested splitting the thermal conductivity of a dense gas into two non-interacting parts; one is due to the transport of translational energy and the other is due to the transport of internal energy. Because only the contribution of the rotational degree of freedom to the internal energy transport is considered in the present study, the specific energy $e^{'}$ of a diatomic gas might be expressed as

$$e^{'} = e^{'}_{tran} + e^{'}_{rot} = c^{'}_{V} T + c^{''}_{V} T \quad , \tag{3.3}$$

where the specific heats at constant volume, $c^{'}_{V}$ and $c^{''}_{V}$, are given by $c^{'}_{V} = 3R/2$ and $c^{''}_{V} = D_R R/2$, respectively (Woods 1993). In general, the local heat flux $\boldsymbol{q}$ of a gas can be expressed as $\boldsymbol{q} = \boldsymbol{q}_{unc} + \boldsymbol{q}_{\text{int}}$, where $\boldsymbol{q}_{unc} = \rho \boldsymbol{u} e$ is the uncollided heat flux and $\boldsymbol{q}_{\text{int}} = \rho \boldsymbol{u} u^2/2$ is the heat flux due to particle interaction. Starting from Eucken's theory of heat conduction (Chapman and Cowling 1970, Woods 1993), it can be shown that the heat flux $\boldsymbol{q}$ is related to the local temperature gradient ∇T, as follows

$$\boldsymbol{q} = \boldsymbol{q}_{unc} + \boldsymbol{q}_{\text{int}} = -\left[\frac{5}{2} c^{'}_{V} p \tau_{eff} + c^{''}_{V} p \tau_{eff} (1+\zeta)\right] \nabla T \quad , \tag{3.4}$$

where ζ is a correction factor for thermal relaxation (Woods 1993). Using the Fourier law of heat conduction, together with expressions for gas physical properties obtained from the modified BE (Ferziger and Kaper 1975), equation (3.4) could be shown to lead to an expression for κ as follows

$$\kappa = \left| \frac{\boldsymbol{q}}{\nabla T} \right| = \frac{5}{2} c^{'}_{V} p \tau_{eff} + c^{''}_{V} p \tau_{eff} (1+\zeta)$$

$$= \frac{\mu c_V}{4}\left(9\gamma + 10\zeta - 6\gamma\zeta - 5\right)$$

$$= \frac{c_P \mu}{4\gamma}\left(9\gamma + 10\zeta - 6\gamma\zeta - 5\right) \quad . \tag{3.5}$$

Eucken suggested that the ratio $f_E = \kappa / c_V \mu$ should be constant for a specific gas. This ratio is known as Eucken's factor. For diatomic gas, its value is given by equation (3.5) as

$$f_E = \frac{\left(9\gamma - 5\right)}{4} + \frac{\zeta\left(5 - 3\gamma\right)}{2} \quad , \tag{3.6}$$

For air, $\gamma = 1.4$ and from experimental evidence $\zeta = 0.15$; this gives rise to $f_E \approx 1.96$, in agreement with the value obtained experimentally by Chapman and Cowling (1970). Consequently, the Prandtl number can be expressed in terms of f_E, as

$$\mathrm{Pr} = \frac{\mu c_P}{\kappa} = \frac{\mu\gamma c_V}{\kappa} = \frac{\gamma}{f_E} \quad . \tag{3.7}$$

According to equation (3.7) and using $f_E \approx 1.96$, $\mathrm{Pr} \approx 0.71$, thus showing that the Prandtl number is recovered using this approach to evaluate heat conduction between particles. From equation (3.5), it can be seen that the derived expression for κ is modified by the factor $\left(9\gamma + 10\zeta - 6\gamma\zeta - 5\right)/4\gamma$ compared with the uncorrected case, and this factor is only dependent on γ and a correction factor ζ for thermal relaxation. It should be noted that the expression for the thermal diffusivity κ' is given by

$$\kappa' = f_E \mu = \frac{\kappa}{c_V} = f_E\left(\gamma - 1\right)\rho e\, \tau_{eff} \quad , \tag{3.8}$$

The net result again is a correction factor given by f_E / γ.

It should be noted that the effective relaxation time τ_{eff} is also present in the correction derived for the thermal diffusivity, κ'. Therefore, this approach to model heat conduction does not require the introduction of another relaxation time to account for thermal energy exchange during the particle collision process.

3.3 Discussion – Recovery of Transport Coefficients for Modeled BE

A correct calculation of γ and the transport coefficients μ and κ is obtained by introducing τ_1 and τ_2 to account for translational, rotational, and thermal energy exchanges during the particle collision process. This indicates that the Reynolds, Mach, and Prandtl numbers can be determined correctly in the process of solving the modeled BE. The specific heat ratio γ is replicated exactly by partially taking into account the weak repulsive potential in the collision process, i.e., the rotational degree of freedom. This, together with Sutherland's law, leads to a relation between τ_1 and τ_2, with the result $\tau_{eff} = \tau_1 / (1 + S_0 / T)$. The factor $1/(1 + S_0 / T)$ can be interpreted as a correction factor for τ_1. This correction factor allows μ (or its dimensionless equivalent Reynolds number) to be recovered; whereas another correction factor given by $(9\gamma + 10\zeta - 6\gamma\zeta - 5)/4\gamma$ permits κ (or its dimensionless equivalent Prandtl number) to be replicated exactly. Physically, this means that the exchange of linear and angular momentum, and the exchange of thermal energy, occur in the same time scale τ_1; the net exchange results only differ by a correction factor. Furthermore, these results imply that the correct

calculation of γ is crucial to the recovery of the NS equations and their transport coefficients. This interpretation is drawn because of the interrelation between γ and T and the fact that T can be expressed as $c^2 / \gamma R$.

3.4 Summary

In this chapter, Eucken's model was invoked to obtain a correct value of the thermal conductivity, κ and the Prandtl number for polyatomic gas. Together with the correction of the first coefficient of viscosity, μ, the modeled BE is ready for aeroacoustic simulations.

The merit of a correct recovery of κ and the Prandtl number for the modeled BE, however, cannot be revealed by those cases studied by Li et al. (2006), since they are without significant temperature gradient. Therefore, a scattering problem caused by acoustic interaction of a line thermal disturbance would be studied by using an improved modeled BE in Chapter 5 and 6. In the next chapter, the effect of non-reflecting boundary conditions on aeroacoustic simulations would be investigated.

Chapter 4

Non-reflecting Boundary Conditions for Direct Aeroacoustics Simulations Using Modeled BE

4.1 Background

The numerical methods used to carry out direct aeroacoustic simulations have to be capable of resolving the disparity in scales between the aerodynamic and acoustic disturbances. However, they are not the only vital component that is important for an accurate resolution of the problem. Most aeroacoustic simulation problems are concerned with open boundaries. All numerical simulations have to invoke truncated boundaries because current computer capacity cannot accommodate infinite boundaries; it is most crucial that all truncated boundaries would not only allow the aerodynamic disturbances but also the acoustic waves to pass through with no reflection. Otherwise, the reflected acoustic waves would interact with the forward-going waves to produce disturbances that could be of the same order as the acoustic waves themselves. The errors thus created cannot be distinguished from the true acoustic waves and the direct aeroacoustic simulation is not reliable. Therefore, a discussion of direct aeroacoustic simulation has to address the numerical method employed as well as the nonreflecting boundary conditions (NRBC) to be invoked for the truncated open boundaries. These two components are briefly discussed in the following paragraphs.

Up to now, one-step aeroacoustic simulations have been carried out by solving the mass, momentum and energy conservation equation, and the gas equation of state. Because the acoustic field has very low-energy contents, a

low dispersive and low dissipative scheme is required if wave propagation were to be resolved accurately in a direct aeroacoustic simulation. A direct numerical simulation (DNS) scheme that satisfies these requirements have been proposed (Lele 1992) and it is made up of a sixth-order compact finite difference scheme and a fourth-order Runge–Kutta time-marching technique. The scheme was later improved (Gaitonde and Visbal 1999, Visbal and Gaitonde 2001) and the improved version has been used to study aeroacoustic problems and was found to be able to resolve the acoustic field with velocity fluctuations five orders of magnitude smaller than any mean field fluctuations (Leung et al. 2006).

The DNS scheme is numerically rather complicated. Efforts to simplify the numeric led to the exploration of an alternate numerical scheme based on the Boltzmann equation (BE) (Frisch et al. 1987, Lallemand and Luo 2000, 2003). The modeled BE is simple because it only needs to solve one transport equation for the particle distribution function $f(\boldsymbol{x}, \boldsymbol{\xi}, t)$, rather than a mixed set of tensor, vector, and scalar equations as in the case of DNS. The flow properties are obtained by integrating f over the particle velocity space. As mentioned in the first chapter, the modeled BE can be solved numerically by either the lattice Boltzmann method (LBM) or the gas-kinetic scheme. The simplicity of the modeled BE attracts researchers to extend one of the numerical scheme, the LBM to carry out one-step aeroacoustic simulationns (Ricot et al. 2002, Tsutahara et al. 2002, Kang et al. 2003, Wilde 2006). Other proposals, based on the lattice kinetic equation (Mallick 2003) and the direct simulation Monte Carlo (Danforth and Long 2004), have also been put

forward. In these methods and the LBM, it is not clear whether the speed of sound c has been recovered correctly because they follow the practice of DNS by specifying the Mach number M as an input to the problem. However, this is not necessary for a gas kinetic approach because, in principle, once f is obtained from the BE, the thermodynamic properties of the gas can be determined and hence c and M. Therefore, it is important to recover the gas equation of state correctly; that is, the specific heat ratio $\gamma = 1.4$ for air for aeroacoustic simulation. One of the reasons for this deficiency could be due to the fact that, inherent in the original LBM proposal (Lallemand and Luo 2003), the compressible form of the Navier–Stokes equations could be recovered but not the correct transport coefficients and proper gas equation of state (Tsutahara et al. 2002, Kang et al. 2003, Philippi et al. 2006). This means that the theoretical relation between c and the internal energy e of the fluid cannot be replicated. As a result, it is not sure whether M can be determined correctly over the whole flow field.

Two improvements are required before the modeled BE can be extended with confidence to simulate aeroacoustics. First, it is necessary to modify the equation so that it can fully recover the complete set of compressible Navier–Stokes equations, that is, the mass, momentum and energy conservation equations with the correct transport coefficients, and the gas equation of state (at least for a diatomic gas). Second, it is necessary to formulate appropriate NRBC for use.

As shown in the last chapter, the first improvement has been accomplished by invoking physical models. In this chapter, examination of

different types of NRBC would be carried out such that an appropriate NRBC could be identified. The improved LBM by Li et al. (2006) is chosen as the numerical scheme for investigation of various NRBC.

4.2 Importance of Appropriate Non-reflecting Boundary Conditions

For a truncated computational domain, precise boundary conditions play a key role in aeroacoustic calculation. At some boundaries, such as the inflow and outflow boundaries, the assumed computational boundaries have to allow the aerodynamic field to pass freely with minimal reflection while at the same time they should be nonreflecting for the incident acoustic waves. Otherwise, the spurious erroneous waves reflecting from the boundaries could contaminate the numerical simulations, decrease the computational accuracy, and might even drive the solutions towards a wrong time stationary state. These requirements are particularly important in one-step numerical simulation of aeroacoustics of open flows, because reflecting waves at open boundaries are strictly prohibited. Otherwise, the acoustic radiation condition will be violated. Therefore, the implementation of NRBC at the computational boundaries is not only necessary but required in the simulation of aeroacoustic problems.

4.3 An Introduction to the Lattice Boltzmann Method (LBM)

To assess the effectiveness of the different NRBC for aeroacoustic simulations using LBM, an LBM that can simulate the fluid properties correctly is required. Such an LBM has been derived by Li et al. (2006). For the sake of completeness, the inadequacy of the conventional LBM is first

pointed out and this is followed by a summary of the remedies made to correctly recover the fluid properties (Li et al. 2006). This improved LBM is used in the present study.

4.3.1 Conventional LBM

The governing equation of the LBM is the BE modeled by adopting the Bhatnagar, Gross, and Krook (BGK) (Bhatnagar et al. 1954) collision model. In this equation, the particle distribution function *f* has the dimensions of $kg \cdot (m/s)^{-3} \cdot m^{-3}$. The dimensionless form of the modeled equation is given by

$$\frac{\partial f}{\partial t} + \boldsymbol{\xi} \cdot \nabla f = -\frac{1}{\tau}\left(f - f^{eq}\right) \quad , \tag{4.1}$$

Where τ is the time taken for f to relax from non-equilibrium to an equilibrium state f^{eq}. All variables in the dimensional BE have been normalized by using a combination of the reference parameters, ρ_∞, c_∞ and *L*. Dimension of *f* is derived according to the zeroth-ordered integral moment of *f* as referred to equation (2.3). Usually, the dense gas assumption was invoked to make use of the Chapman–Enskog expansion to derive the complete set of compressible Navier–Stokes equations and their transport coefficients from the BGK-modeled BE Lallemand and Luo 2003). Only the translational degree of freedom was considered in formulating the BGK model; as a result, the particles were assumed to undergo rigid collision with a relaxation time τ. This assumption led to $\gamma = (D_n + 2)/D_n$, $\mu = \rho RT\tau$, and $\kappa = c_P \mu$, where c_P is specific heat at constant pressure. Therefore, 3-D flow of monoatomic

gases gives $\gamma = 1.67$ and 2-D flow yields $\gamma = 2$. The conventional LBM solving the BGK modeled BE was unable to replicate the full set of compressible Navier–Stokes equations with correct transport coefficients and γ, and was not appropriate for aeroacoustic simulations. Therefore, further improvements are required if γ and the transport coefficients were to be recovered correctly.

4.3.2 Improved LBM

The improved LBM (Li et al. 2006) attempts to accomplish this by following a two-step approach. The first step concentrates on the recovery of γ and μ, whereas the second step focuses on deriving κ correctly. It should be pointed out that in the present formulation, μ and κ are the dimensionless counterparts of the fluid viscosity and thermal conductivity; they are normalized by $\rho_\infty cL$. Effort to accomplish the first step has been made by including both the translational and rotational degree of freedom into the derivation of an effective relaxation time τ_{eff} to replace τ in equation (4.1). This τ_{eff}, as introduced in Chapter 2, was assumed to be made up of two relaxation times, τ_1 and τ_2. It was found that τ_1 is essentially given by the rigid-sphere collision model, that is, τ, and τ_2 can be determined exactly with no arbitrary constant by stipulating that the derived μ should obey the Sutherland law. This improvement, however, could not rectify the error in the prediction of κ, which, according to this formulation, is given by $\kappa = c_P \mu$, thus leading to a Prandtl number $\Pr = c_P \mu / \kappa = 1$ for diatomic gases.

In the preceding chapter, κ has been recovered correctly by invoking Eucken's model for the derivation of the macroscopic heat flux without an introduction of an additional relaxation time other than that proposed by Li et al. (2006). Thus derived, the improved LBM is able to replicate μ, γ and κ correctly, thus leading to a correct estimate of the Reynolds number, $\mathrm{Re} = \rho UL/\mu^*$, the Mach number $M = U/c$, and Pr, in a low- Reynolds-number, shock-free compressible flow. Here, μ^* is the dimensional μ.

4.4 Numerical Solution of the Improved LBM

The modeled equation (4.1) is solved numerically by first discretizing it in a velocity space using a finite set of velocity vectors $\{\boldsymbol{\xi}_i\}$ in the context of the conservation laws. Here, the subscript i is only an index and is not a vector or tensor notation. A local Maxwellian is used to represent f^{eq} and a Taylor expansion up to third order in $\boldsymbol{u}$ is assumed. This can be expressed in the discrete velocity space as

$$f^{eq} = \rho A_i \left\{ 1 + \frac{\boldsymbol{\xi}\cdot\boldsymbol{u}}{\theta} + \frac{1}{2}\left(\frac{\boldsymbol{\xi}\cdot\boldsymbol{u}}{\theta}\right)^2 - \frac{\boldsymbol{u}^2}{2\theta} - \frac{(\boldsymbol{\xi}\cdot\boldsymbol{u})\boldsymbol{u}^2}{2\theta^2} + O\left(\frac{(\boldsymbol{\xi}\cdot\boldsymbol{u})^3}{\theta^3}\right) \right\}, \quad (4.2)$$

where $\mathbf{u} = (u, v)$ and $\theta = RT/c^2$. The weighting factors A_i are dependent on the lattice model selected to represent the discrete velocity space. They are evaluated from the constraints of the local macroscopic variables, such as ρ, momentum $\rho\boldsymbol{u}$, internal energy e, and pressure p, given by the integrals of f and $\boldsymbol{\xi}$ over the velocity space in the lattice with N discrete velocity sets $\{\boldsymbol{\xi}_i\}$.

A discrete velocity set given by a D2Q13 (2-D with 13 velocity points) lattice model is adopted here, because D2Q13 has been shown to give very reliable and accurate results by Li et al. (2006). The velocity lattice is shown in Figure 4.1, and the discrete velocity set and weighting factors A_i are given by

$$\begin{aligned}
&\boldsymbol{\xi}_0 = 0 \\
&\boldsymbol{\xi}_i = \left\{\cos\left(\frac{\pi(i-1)}{4}\right), \sin\left(\frac{\pi(i-1)}{4}\right)\right\} \;, \quad i = 1, 3, 5, 7 \\
&\boldsymbol{\xi}_i = \sqrt{2}\left\{\cos\left(\frac{\pi(i-1)}{4}\right), \sin\left(\frac{\pi(i-1)}{4}\right)\right\} \;, \quad i = 2, 4, 6, 8 \\
&\boldsymbol{\xi}_i = 2\left\{\cos\left(\frac{\pi(i-1)}{4}\right), \sin\left(\frac{\pi(i-1)}{4}\right)\right\} \;, \quad i = 9, 10, 11, 12
\end{aligned} \qquad , \tag{4.3a}$$

$$\begin{aligned}
&A_0 = 1 - \frac{5}{2}\theta + (-\frac{3}{2} + 2\gamma)\theta^2 \\
&A_1 = A_3 = A_5 = A_7 = \frac{2}{3}\theta + (1-\gamma)\theta^2 \\
&A_2 = A_4 = A_6 = A_8 = (-\frac{3}{4} + \frac{1}{2}\gamma)\theta^2 \\
&A_9 = A_{10} = A_{11} = A_{12} = -\frac{1}{24}\theta + \frac{1}{8}\theta^2
\end{aligned} \qquad , \tag{4.3b}$$

The collision term in equation (4.1) is evaluated locally at every time step, whereas a sixth-order compact finite-difference scheme (Lele 1992) is used to evaluate the nonlinear term and a second-order Runge–Kutta method for time advancement. The lattice size δx is chosen such that $\delta x / \delta t \approx c$, where δt for the lattice motion is chosen to be the same as Δt for time marching and the grid size Δx is taken to be the same as that used in the DNS scheme. This choice of $\delta x / \delta t$ yields very stable numerical solutions for all cases investigated. On boundaries, a one sided fourth-order compact method is used to derive the first derivatives. This is essentially a low dispersive and

low dissipative scheme and is most suitable for simulation of aeroacoustic problems (Lele 1992, Gaitonde and Visbal 1999, Visbal and Gaitonde 2001).

4.5 Selection of Non-reflecting Boundary Conditions for the Improved LBM

The commonly used boundary treatment schemes for DNS are NSCBC, PML, ABC, FM, and C^1 continuity, whereas those that have been attempted only for LBM are the EM and ZFG methods. Among the various boundary treatment schemes, some proposed for DNS can be extended to LBM, whereas others cannot. For example, extension of the NSCBC scheme to LBM has been attempted (Ricot et al. 2002) previously. Unfortunately, no details were given on the implementation; therefore, it was difficult to ascertain the general applicability of such an extension. The NSCBC scheme has been carefully examined by Li (2006), who chose the propagation in a mean flow of a vortex, entropy, and an acoustic pulse to compare the performance of the NSCBC, PML, and ABC with a reference solution. The simulation was carried out using DNS and the reference solution was obtained using a much larger domain with buffer regions at the inlet and outlet. The results showed that among the schemes tested, PML and ABC gave the least error, whereas NSCBC gave the largest error compared to the reference solution. Straightly speaking, NSCBC works best with normal waves at the boundaries and this was one of the reasons why it performed the worst in this case. It is the objective of this work to seek NRBC that is applicable to all types of waves including normal waves. This shortcoming of the NSCBC

together with the assessment of Li (2006) renders it inappropriate for extension to LBM simulation.

Applying the C^1 continuity preservation scheme directly to the primitive variables is not a viable alternative for LBM; however, the concept can be extended to LBM. Applying the C^1 continuity preservation scheme concept to LBM implies that the first derivatives of f have to remain continuous across the boundaries, and the inward first derivatives of f will have to be set to zero. This is different from the EM; therefore, it should be tested as an independent method. The PML is not quite applicable for LBM because the LBM only solves a scalar equation for f and the primitive variables are obtained by integrating f over the particle velocity space $\boldsymbol{\xi}$ and an a priori solution is not known for f in any matched layer. However, the concept could be extended by requiring f to approach a target f or f^{eq} at the boundaries. When the PML is implemented this way, it is not much different from the application of ABC to LBM. As will be seen later, applying the ABC to LBM requires the specification of a target f or f^{eq} at the boundaries. In view of this similarity, only the extension of ABC and not the PML to LBM will be considered in this paper. Because the ZFG has been used before to calculate identical benchmark aeroacoustic problems and good agreement with the reference DNS solution is obtained (Engquist and Majda 1977), there is no need to repeat the same calculations here again. In fact, the ZFG can be considered a viable nonreflecting boundary treatment scheme for one-step aeroacoustic simulations of the benchmark problems tested (Li et al. 2006). As a result, three types of nonreflecting boundary treatment schemes, namely,

1) EM with or without FM,

2) C^1 continuity, and

3) ABC are tested in the present study.

Their suitability for LBM and accuracy are assessed against reference solutions obtained from DNS with a relatively large computational domain. In the DNS calculations, absorbing boundary treatments are applied. The clean solution obtained inside the larger computational domain is used as the reference solution. All error estimates of the LBM calculations are based on this reference. Each type of nonreflecting boundary treatment scheme is briefly described in the following sections.

4.5.1 Type 1: EM with or Without FM

This method is fairly easy to implement. Depending on whether zeroth- or first-order extrapolation is assumed, the method simply requires that f or its first gradient in every lattice directions at the computational boundary to be zero (Chen et al. 1996, Maier et al. 1996, Guo and Zhao 2003, Yu et al. 2005, Bennet et al. 2005). It is particularly suitable for LBM because there is only one scalar equation to solve. Of course, a buffer or damping region could be added to improve the performance of the method, but then the scheme would be quite similar to the ABC. Another alternative to improve its performance is to implement the EM with or without a FM. That way, their performance with or without FM could be assessed and compared.

The filtering scheme (Gaitonde and Visbal 1999, Visbal and Gaitonde 2001) implemented uses a 10th-order low passed filter. If there are $\boldsymbol{n}$ grid

points along the x axis, the equations of a low-passed filtered value $\hat{h}$ for any scalar h can be obtained from

$i = 1$ or $i = n$; no filtering is applied, (4.4a)

$i \in \{2,3,4\}$

$$\alpha\,\hat{h}_{i-1} + \hat{h} + \alpha\,\hat{h}_{i+1} = \sum_{j=1}^{9} a_{j,i} h_j \quad , \tag{4.4b}$$

$i \in \{n-3, n-2, n-1\}$

$$\alpha\,\hat{h}_{i-1} + \hat{h} + \alpha\,\hat{h}_{i+1} = \sum_{j=1}^{9} a_{j,n-i+1} h_{n-j+1} \quad , \tag{4.4c}$$

$i = 5$ or $i = n-4$

$$\alpha\,\hat{h}_{i-1} + \hat{h} + \alpha\,\hat{h}_{i+1} = \sum_{j=1}^{5} \frac{b_j}{2}\left(h_{i+j} + h_{i-j}\right) \quad , \tag{4.4d}$$

$i \in \{6,7,...,n-5\}$

$$\alpha\,\hat{h}_{i-1} + \hat{h} + \alpha\,\hat{h}_{i+1} = \sum_{j=1}^{5} \frac{a_j}{2}\left(h_{i+j} + h_{i-j}\right) \quad , \tag{4.4e}$$

where $\alpha = 0.49$ ($0.3 \le \alpha \le 0.5$) and the a_j, b_j, $a_{j,i}$ are given in Table 4.1. It should be noted that a 10th-order filter is applied at interior points for $i \in \{6,7,...,n-5\}$ and an eighth-order filter is applied near boundaries for $i \in \{2,...,5\}$ and $i \in \{n-4,...,n-1\}$.

The designations, EM0, EM1, EM0/FM, and EM1/FM are used to denote the following combinations of EM and FM schemes: EM0 designates zeroth-order EM without FM, EM1 designates first-order EM without FM,EM0/FM designates zeroth-order EM with FM, and EM1/FM designates first-order EM with FM.

4.5.2 *Type 2: C^1 Continuity*

The basic idea of this method, hereafter designated as C^1 continuity, is to extrapolate whatever variables (f, first derivatives of f, etc.) chosen for consideration at the computational boundary based on at least two known points inside the domain. In addition, the inward f (or first derivatives of f) in all lattice directions is assumed to be zero. Lower-order extrapolation methods (e.g., zeroth and first order) are easy to adopt for finite-difference schemes up to third order. Generally, the order of accuracy of the method should be at most one order lower than that of the finite-difference scheme used for the numerical simulation. If not, the overall order of accuracy would be lowered (Freund 1997). No filter or buffer region is added to this scheme.

4.5.3 *Type 3: ABC*

An absorbing region is established based on the addition of dissipative and convective terms to the compressible Navier–Stokes equations in the case of DNS schemes. The prescribed flow (usually uniform mean flow) is achieved on the boundary by suppressing all undesirable disturbances within the region. Therefore no reflection is detected at the boundary. This can be seen by considering a prescribed flow with properties given by a flow with target properties. This concept can be extended to LBM where the absorption is implemented in the f equation which can be written in the buffer region for a 2-D problem as

$$\frac{\partial f}{\partial t} + \boldsymbol{\xi} \cdot \nabla f + \sigma\left(f^{eq} - f_a\right) = -\frac{1}{\tau_{eff}}\left(f - f^{eq}\right) \quad , \tag{4.5}$$

where f_a has the same structure as the weighting factor A_i , $\sigma = \sigma_m \left(\delta / D\right)^2$, and σ_m is a constant to be specified. The target f_a is therefore achieved asymptotically towards the outer boundary of the absorbing region. This boundary scheme is referred to as ABC from this point on.

4.6 Case Study for Non-Reflecting Boundary Conditions by Using the Improved LBM

In the present study, an investigation into the performance of the three different nonreflecting boundary treatment schemes is carried out. The vehicles of this comparison are two classical aeroacoustic problems that have been investigated previously (Li et al. 2006). These two problems are as follows:

Case 1) propagation of a plane pressure pulse;

Case 2) propagation and interaction of an acoustic pulse with an entropy pulse and a vortex pulse.

The benchmark solutions were provided by DNS calculations assuming a much larger computational domain. The DNS computational domain and the truncated domain for LBM simulations chosen for these two cases are specified in following sections. It is sufficient to note that in the DNS calculations, no filtering or damping is applied. In the first case, the initial size of the acoustic pulse L, c_∞ , and mean density ρ_∞ are adopted as the reference quantities for normalization. The Reynolds number is defined as $Re = \rho_\infty c_\infty L / \mu_\infty$. In the second case, the initial size of the acoustic pulse L, uniform mean flow u_∞ , and mean density ρ_∞ are adopted as the reference

quantities for normalization. The Reynolds number and Mach number of the second case are defined as $Re = \rho_\infty u_\infty L / \mu_\infty$ and $M = u_\infty / c_\infty$. In both cases a uniform grid size of $\Delta x = \Delta y = 0.05$ and a time step of $\Delta t = 0.00001$ are used in all calculations for consistency of comparison.

Here, x and y are the Cartesian coordinates with the propagation direction aligned with x, and μ_∞ is the reference fluid viscosity.

To demonstrate the validity and extent of the LBM simulations, the accuracy of the solutions are evaluated against the benchmark DNS solutions obtained using the larger domain with absorbing boundary treatment applied. The setup of absorbing boundary treatment applied to LBM is the same as that applied to DNS. A measure of the error between the LBM and DNS results of a macroscopic variable b is expressed in terms of the L_P integral norm

$$\left\| L_P(b) \right\| = \left[\frac{1}{M} \sum_{j=1}^{M} \left| b_{\mathrm{LBM},j} - b_{\mathrm{DNS},j} \right|^P \right]^{\frac{1}{P}} \quad , \tag{4.6}$$

for any integer p and its maximum

$$\left\| L_\infty(b) \right\| = \max_j \left| b_{\mathrm{LBM},j} - b_{\mathrm{DNS},j} \right| \quad , \tag{4.7}$$

Errors based on equations (4.6) and (4.7) are calculated using the three NRBC outlined in the preceding sections. The error estimates for the pressure and velocity deduced from all three types of NRBC are tabulated in Tables 4.2–4.3.

4.6.1 Case 1: Propagation of a Plane Pressure Pulse

For this 1-D problem, the validity of those NRBC specified in section 4.4 is tested by applying them on both the inlet and outlet boundary, while C^1

continuity is used on the top and bottom boundaries. As demonstrated in Li et al. (2006), the large computational domain chosen for DNS simulation is $-10 \le x \le 10$ and $-1 \le y \le 1$, and the truncated size for LBM calculations is given by $-5 \le x \le 5$ and $-1 \le y \le 1$. This allows the present calculations to be compared with those presented using ZFG for boundary conditions (Li et al. 2006). In ABC, an absorbing region with a width of $D = 1$ is added to the inlet and outlet boundaries. Because $\Delta x = 0.05$, there are 20 grid points along the x direction in the absorbing region. No ABC is implemented at the top and bottom boundaries. The EM and C^1 continuity NRBC are applied to computational domains of the same size as ABC minus the absorbing region.

The initial conditions for the aerodynamic and acoustics fluctuations are specified as (Tam and Webb 1993)

$$\rho = \rho_\infty, \quad u = u_\infty, \quad v = v_\infty, \quad p = p_\infty + \varepsilon \exp(k) \quad , \tag{4.8}$$

where $k = -\ln 2 \times \left(x / 0.08 \right)^2$. For the plane pressure pulse problem considered here, $\rho_\infty = 1, u_\infty = 0, v_\infty = 0, p_\infty = 1/\gamma,$ are chosen as reference quantities, while $\mathrm{Re} = 1000$ and $\varepsilon = 0.0001$ are specified. Using these reference quantities, the initial f^{eq} is specified according to equations (4.2) and (4.3).

Calculations are carried out using the three types of boundary treatment schemes discussed in section 4.4. Four different combinations of the EM type are tested; they are the zeroth- and first-order EM with and without the use of filtering. Altogether, six different boundary conditions are investigated; they are EM0, EM0/FM, EM1, EM1/ FM,$C1$ continuity, and ABC. Although the EM boundary conditions work well for aerodynamic flow

calculations (Chen et al. 1996, Maier et al. 1996, Guo and Zhao 2003, Yu et al. 2005, Bennet et al. 2005), their suitability for one-step aeroacoustic simulations needs demonstration. These combinations of EM and FM could clearly demonstrate the necessity of having to implement FM in any one-step aeroacoustic simulations using EM and the relative merits of a zeroth- or first-order extrapolation.

Absolute integral norm error $\|L_1(p)\|$, integral root mean square (rms) error norm $\|L_2(p)\|$, and the maximum error norm $\|L_\infty(p)\|$ are calculated at $t = 9$. Norm errors for fluctuating pressure $\boldsymbol{p}$ and the streamwise velocity $\boldsymbol{u}$ are determined using equations (4.6) and (4.7) and the results for EM0, EM0/FM, EM1, EM1/FM, C^1 continuity, and ABC are tabulated in Tables 4.2 and 4.3. Among the nonreflecting boundary treatment schemes tested, three schemes give the best performance for the calculations of p and u. They are EM0/FM, EM1/FM, and ABC. Besides, ABC gives the least L_2 error among the three best performed nonreflecting boundary treatment schemes, with the same order of magnitude as previous calculations of the same pulse at $\mathrm{Re} = 5000$ (Li et al. 2006). The worst performers are EM0 and EM1. This shows that filtering is necessary for one-step aeroacoustic simulation problems if these norm errors are to be reduced to minimum. Once filtering is applied, the difference between a zeroth-order extrapolation and a first-order one is negligibly small. This is the reason why EM0/FM and EM1/FM have essentially the same performance.

The plots of $(\rho - \rho_\infty)$, $(p - p_\infty)$, and $\boldsymbol{u}$ at $t = 0$, $t = 3$, $t = 6$, and $t = 9$ for the four NRBC schemes, EM0/FM, EM1/FM, C^1 continuity, and ABC, are

shown in Figures 4.2(a), 4.3(a), 4.4(a), and 4.5(a), respectively. From the EM0 and EM1 calculations, it is obvious that at $t = 9$ the waves are reflected back from the inlet and outlet boundaries. Therefore, these results are not shown. To depict the wave behavior more clearly at the inlet and outlet boundaries, blowups of the density at these locations are given in Figures 4.2(b), 4.3(b), 4.4(b), and 4.5(b). It is clear that the errors at these boundaries are at least one order of magnitude less.

For the C^1 continuity scheme, even though the inward first derivatives of f at the boundaries are set to zero, disturbance waves are clearly visible as early as $t = 6$ (Figure 4.4(a)). As a result, numerical results deduced from these three schemes are not in agreement with the reference DNS solution and the clean exit of all waves at $t = 9$ shown in the DNS result is not replicated correctly by the three boundary treatment schemes. The calculated results given by EM0/ FM, EM1/FM, and ABC (Figures 4.2, 4.3, and 4.5) are in excellent agreement with the DNS result and they show a clean exit of all waves at $t = 9$. These results further support the conclusion drawn from a comparison of the error norm in Tables 4.2 and 4.3. Because a 10th-order filtering scheme (Gaitonde and Visbal 1999, Visbal and Gaitonde 2001) is used in the extrapolation method, the results therefore suggest that reflections from the inlet and outlet boundary are mainly due to high-frequency components in the computational domain. This explains why extrapolation method can be applied to low-order LBM schemes (Chen et al. 1996, Maier et al. 1996, Guo and Zhao 2003, Yu et al. 2005, Bennet et al. 2005), because high-frequency disturbances are not being resolved by these low-order LBM

schemes. The ABC, on the other hand, is equally applicable for low as well as high-order LBM schemes; therefore, it can be used effectively for the calculations of aerodynamic flow alone as well as for one-step aeroacoustic problems. Because ZFG has already been validated as a viable nonreflecting boundary condition for this problem (Li et al. 2006), up to this point, three different types of nonreflecting boundary treatment schemes (EM0/FM and EM1/FM can be considered as the same type) have been proven appropriate. Of these, ABC is an extension of a current scheme used in DNS to LBM.

4.6.2 Case 2: Propagation of Acoustic, Entropy, and Vortex Pulses

As before, the large computational domain is specified as $-10 \le x \le 10$ and $-10 \le y \le 10$, and the acoustic pulse is initialized at $x = -1$ and $y = 0$, whereas the entropy pulse and the vorticity pulse are initialized at $x = 1$ and $y = 0$. The truncated computational domain for EM1/FM is given by $-2.5 \le x \le 2.5$ and $-2.5 \le y \le 2.5$. In the case of the ABC, an absorbing region with $D = 1$ is specified on all boundaries. Consequently, the computational domain for the ABC boundary treatment is $-3.5 \le x \le 3.5$ and $-3.5 \le y \le 3.5$. The initial conditions for the aerodynamic and acoustics fluctuations are specified as

$$\begin{aligned} &\rho = \rho_\infty + \varepsilon_1 e^a + \varepsilon_2 e^b, \quad u = u_\infty + \varepsilon_2 e^b, \\ &v = v_\infty - \varepsilon_2 (x-1) e^b, \quad p = p_\infty + \varepsilon_1 e^a / M^2 \end{aligned} \quad , \tag{4.9a}$$

$$a = -\ln 2 \left(\frac{(x+1)^2 + y^2}{0.2^2} \right) \quad , \tag{4.9b}$$

$$b = -\ln 2\left(\frac{(x-1)^2 + y^2}{0.4^2}\right) \quad , \tag{4.9c}$$

where $\varepsilon_1 = 0.0001, \varepsilon_2 = 0.001$. For this problem, the reference quantities are specified as $\rho_\infty = 1; u_\infty = 0; v_\infty = 0$ and $p_\infty = 1/\gamma M^2$, while $\mathrm{Re} = 1000$ and $M = 0.2$ are chosen, which are the same as those previously reported (Tam and Webb 1993). Using these reference quantities, the initial f^{eq} is specified according to equations (4.2) and (4.3). The problem setup is visualized in Figure 4.6.

This problem has also been treated in Li et al. (2006), and good agreement with DNS results is obtained using the ZFG boundary treatment scheme. In the preceding example, it has been shown that among the three types of boundary treatment schemes considered, only EM/FM and ABC can reproduce the DNS results in a truncated computational domain. Even then, all six schemes are used to perform the LBM calculations of this problem and the calculated error norms are tabulated in Tables 4.4 and 4.5 for comparison. Again, $\|L_1(p)\|$, $\|L_2(p)\|$ and $\|L_\infty(p)\|$ at $t = 2.6$ for EM0, EM0/FM, EM1, EM1/FM,C^1 continuity, and ABC are calculated and shown in Tables 4.4 and 4.5. Only the norm errors of *p* and *u* are determined. As expected, EM0/FM, EM1/FM, and ABC yield the least errors, whereas the C^1 continuity scheme gives errors that are in between those of EM0 and EM1, and EM0/FM, EM1/FM, and ABC. The worst performers are EM0 and EM1. Again, ABC gives the least L_1, L_2, and L_1 error among all schemes tested.

A sample comparison of the LBM calculations invoking ABC with those of DNS for case 2 is shown in Figure 4.7. The panels under Figure 4.7(a) are pressure plots, whereas those under Figure 4.7(b) are velocity contours. Altogether four different times are shown ranging from $t = 0.1 \text{ to } t = 2.6$. The solution in the upper part of each panel is due to LBM and the lower part is the corresponding DNS simulation obtained using a larger computational domain. It can be seen that by $t = 2.6$, the pulses have completely exited the computational domain defined by $-2.5 \le x \le 2.5$ and $-2.5 \le y \le 2.5$; that is, the actual domain not counting the absorbing region assumed for the LBM simulation. The solutions obtained using both LBM and DNS are very clean and there is essentially no reflection of waves at the boundaries. It should be pointed out that the computational domain for the LBM is only $-3.5 \le x \le 3.5$ and $-3.5 \le y \le 3.5$ compared to a domain of $-10 \le x \le 10$ and $-10 \le y \le 10$ for the DNS. This shows that LBM with ABC is a viable alternative to DNS with buffer region for direct aeroacoustic simulations.

4.7 Summary and Conclusions

There are three objectives to this study. The first is to determine what commonly used NRBC for DNS simulations could be extended to LBM. The second is to ascertain whether the same accuracy could be achieved using a truncated computational domain compared to that required by DNS. The third is to identify best-performing NRBC for one-step LBM simulation of aeroacoustic problems. This investigation gives rise to three different types of NRBC schemes that could be extended to LBM and they are the filtering (FM) type, the C1 continuity type, and the absorbing (ABC) type. In addition, two other NRBC schemes that have been used previously for LBM simulations have been extended to one-step LBM aeroacoustic calculations. These are the extrapolation (EM) type and the zero f gradient (ZFG) type. The FM type and the EM type are tested in a mixed manner. Because the ZFG has already been proven to be valid for one-step LBM in Li et al. (2006), the present investigation does not include it in the final assessment.

Two aeroacoustic problems, namely, the propagation of a plane pressure pulse and the propagation of an acoustic pulse, an entropy pulse, and a vorticity pulse in a mean flow, are used as vehicles to test the different NRBC schemes. Altogether, six different schemes are tested; they are EM0, EM0/FM, EM1, EM1/FM, C1 continuity, and ABC. Of these six, only EM0/FM, EM1/FM, and ABC are capable of yielding results that are essentially identical to those deduced from a one-step DNS simulation using a much larger computational domain with no boundary treatment. Overall, ABC performs the best. This result together with the previous study using

ZFG gives four appropriate and applicable NRBC for one-step LBM simulation of aeroacoustic problems.

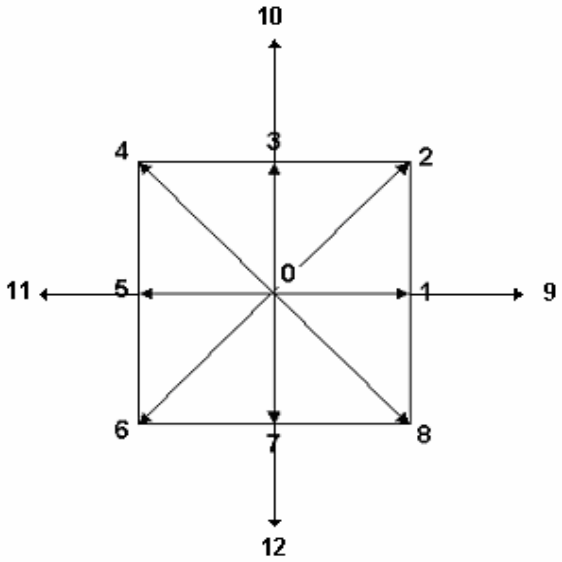

Figure 4.1 Definition of the D2Q13 lattice velocity model

Table 4.1 Values of a_j, b_j and $a_{j,i}$

	a_j	b_j	$a_{j,2}$	$a_{j,3}$	$a_{j,4}$
j=0	$\frac{193+126\alpha}{256}$	$\frac{93+70\alpha}{128}$	-	-	-
j=1	$\frac{105+302\alpha}{256}$	$\frac{7+18\alpha}{16}$	$\frac{1+254\alpha}{256}$	$\frac{-1+2\alpha}{256}$	$\frac{1-2\alpha}{256}$
j=2	$\frac{15(-1+2\alpha)}{64}$	$\frac{-7+14\alpha}{32}$	$\frac{31+2\alpha}{32}$	$\frac{1+30\alpha}{32}$	$\frac{-1+2\alpha}{32}$
j=3	$\frac{45(1-2\alpha)}{512}$	$\frac{1-2\alpha}{16}$	$\frac{7+50\alpha}{64}$	$\frac{57+14\alpha}{64}$	$\frac{7+50\alpha}{64}$
j=4	$\frac{5(-1+2\alpha)}{256}$	$\frac{-1+2\alpha}{128}$	$\frac{-7+14\alpha}{32}$	$\frac{7+18\alpha}{32}$	$\frac{25+14\alpha}{32}$
j=5	$\frac{1-2\alpha}{512}$	*0*	$\frac{7(5-10\alpha)}{128}$	$\frac{7(-5+10\alpha)}{128}$	$\frac{35+58\alpha}{128}$
j=6	-	-	$\frac{-7+14\alpha}{32}$	$\frac{7-14\alpha}{32}$	$\frac{-7+14\alpha}{32}$
j=7	-	-	$\frac{7-14\alpha}{64}$	$\frac{-7+14\alpha}{64}$	$\frac{7-14\alpha}{64}$
j=8	-	-	$\frac{-1+2\alpha}{32}$	$\frac{1-2\alpha}{32}$	$\frac{-1+2\alpha}{32}$
j=9	-	-	$\frac{1-2\alpha}{256}$	$\frac{-1+2\alpha}{256}$	$\frac{1-2\alpha}{256}$

Table 4.2 Norm error at $t = 9$ for case 1 (compared with DNS solutions): (a) pressure; (b) velocity ($\hat{p} = p - p_\infty$, $\hat{u} = u - u_\infty$; $\hat{p}_r$ and $\hat{u}_r$ are the reference solutions).

(a)

$\|L_P\| = \left(\frac{1}{n} \sum (\hat{p} - \hat{p}_r)^P \right)^{\frac{1}{P}}$ $\|L_\infty\| = \max(\hat{p} - \hat{p}_r)$	L_1	L_2	L_∞
EM0	4.2342 x 10^{-6}	7.5517 x 10^{-6}	1.9047 x 10^{-5}
EM0/FM	6.8096 x 10^{-8}	1.1516 x 10^{-7}	2.8650 x 10^{-7}
EM1	4.2377 x 10^{-6}	7.5587 x 10^{-6}	1.9064 x 10^{-5}
EM1/FM	7.2198 x 10^{-8}	9.4061 x 10^{-8}	2.1736 x 10^{-7}
C^1 Continuity	1.0677 x 10^{-6}	1.3857 x 10^{-6}	3.1877 x 10^{-6}
ABC	1.8837 x 10^{-8}	2.0648 x 10^{-8}	5.4979 x 10^{-8}

(b)

$\|L_P\| = \left(\frac{1}{n} \sum (\hat{u} - \hat{u}_r)^P \right)^{\frac{1}{P}}$ $\|L_\infty\| = \max(\hat{u} - \hat{u}_r)$	L_1	L_2	L_∞
EM0	4.2409 x 10^{-6}	7.5617 x 10^{-6}	1.9096 x 10^{-5}
EM0/FM	6.2575 x 10^{-8}	1.0379 x 10^{-7}	2.7033 x 10^{-7}
EM1	4.2451 x 10^{-6}	7.5687 x 10^{-6}	1.9113 x 10^{-5}
EM1/FM	6.7929 x 10^{-8}	1.0123 x 10^{-7}	2.6062 x 10^{-7}
C^1 Continuity	1.0357 x 10^{-6}	1.3630 x 10^{-6}	3.1571 x 10^{-6}
ABC	2.4918 x 10^{-8}	3.3341 x 10^{-8}	8.2538 x 10^{-8}

Table 4.3 Norm error at t = 2.6 for case 2 (compared with DNS solutions): (a) pressure; (b) velocity ($\hat{p} = p - p_\infty$, $\hat{u} = u - u_\infty$; $\hat{p}_r$ and $\hat{u}_r$ are the reference solutions).

(a)

$\|L_P\| = \left(\frac{1}{n} \sum (\hat{p} - \hat{p}_r)^P \right)^{\frac{1}{P}}$ $\|L_\infty\| = \max(\hat{p} - \hat{p}_r)$	L_1	L_2	L_∞
EM0	5.2606 x 10^{-5}	7.4286 x 10^{-5}	3.1617 x 10^{-4}
EM0/FM	3.1530 x 10^{-5}	3.6230 x 10^{-5}	7.5139 x 10^{-5}
EM1	5.3584 x 10^{-5}	7.525 x 10^{-5}	3.2101 x 10^{-4}
EM1/FM	5.6519 x 10^{-5}	6.9461 x 10^{-5}	1.8350 x 10^{-4}
C^1 Continuity	9.8387 x 10^{-6}	1.3297 x 10^{-5}	7.9179 x 10^{-5}
ABC	2.7005 x 10^{-6}	3.5453 x 10^{-6}	1.3460 x 10^{-5}

(b)

$\|L_P\| = \left(\frac{1}{n} \sum (\hat{u} - \hat{u}_r)^P \right)^{\frac{1}{P}}$ $\|L_\infty\| = \max(\hat{u} - \hat{u}_r)$	L_1	L_2	L_∞
EM0	1.8421 x 10^{-5}	3.2891 x 10^{-5}	2.0135 x 10^{-4}
EM0/FM	6.6930 x 10^{-6}	7.6686 x 10^{-6}	1.7774 x 10^{-5}
EM1	1.8483 x 10^{-5}	3.2924 x 10^{-5}	2.0126 x 10^{-4}
EM1/FM	1.1918 x 10^{-5}	1.4490 x 10^{-5}	3.8759 x 10^{-5}
C^1 Continuity	1.037 x 10^{-5}	2.9847 x 10^{-5}	1.9847 x 10^{-4}
ABC	1.5974 x 10^{-6}	2.1588 x 10^{-6}	1.0723 x 10^{-5}

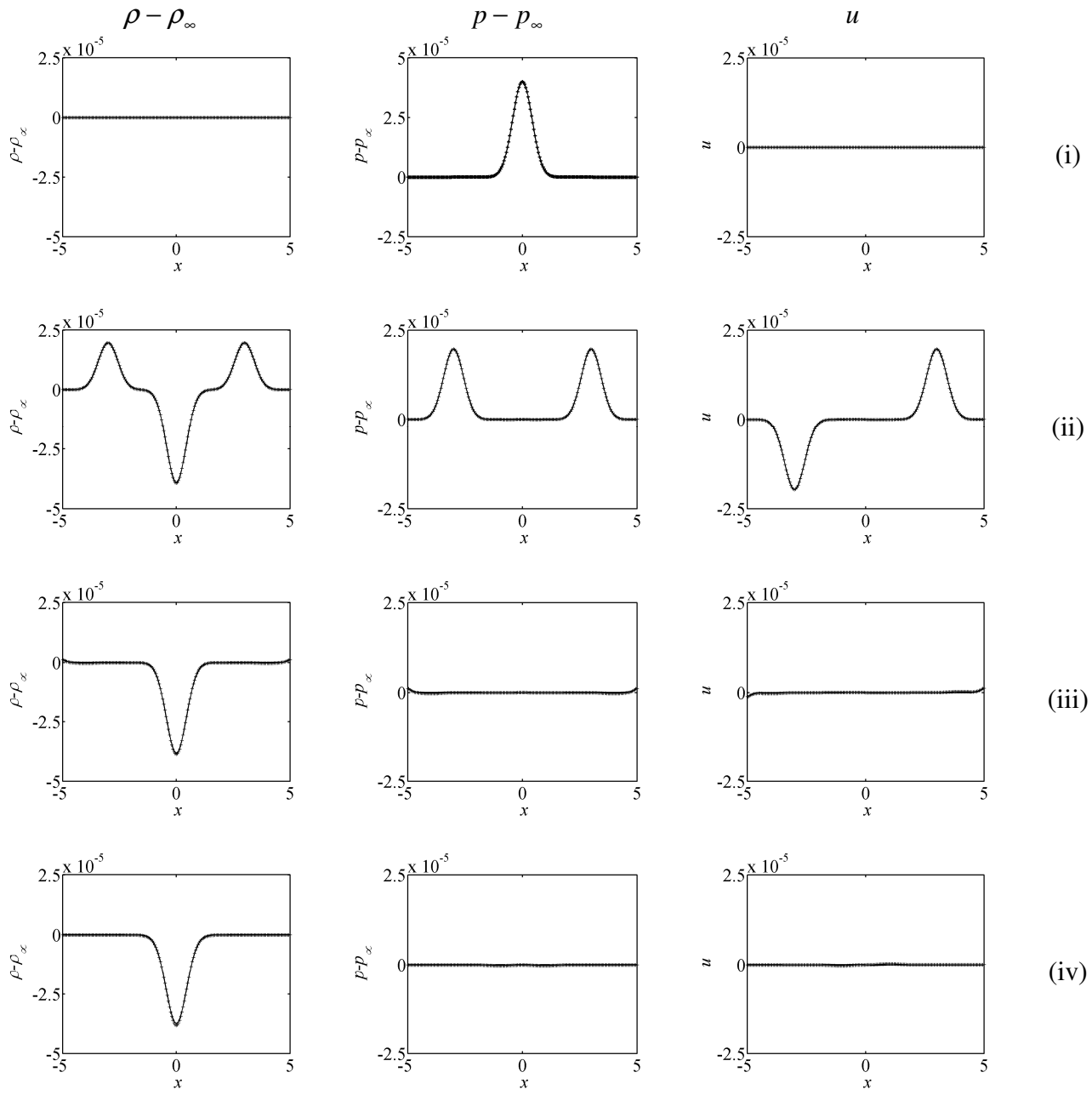

Figure 4.2(a) The density, pressure and velocity "u" fluctuations along the x-axis at four different t with zeroth-ordered extrapolation boundary conditions (with filter) EM0/FM: +, LBM; ———, DNS.

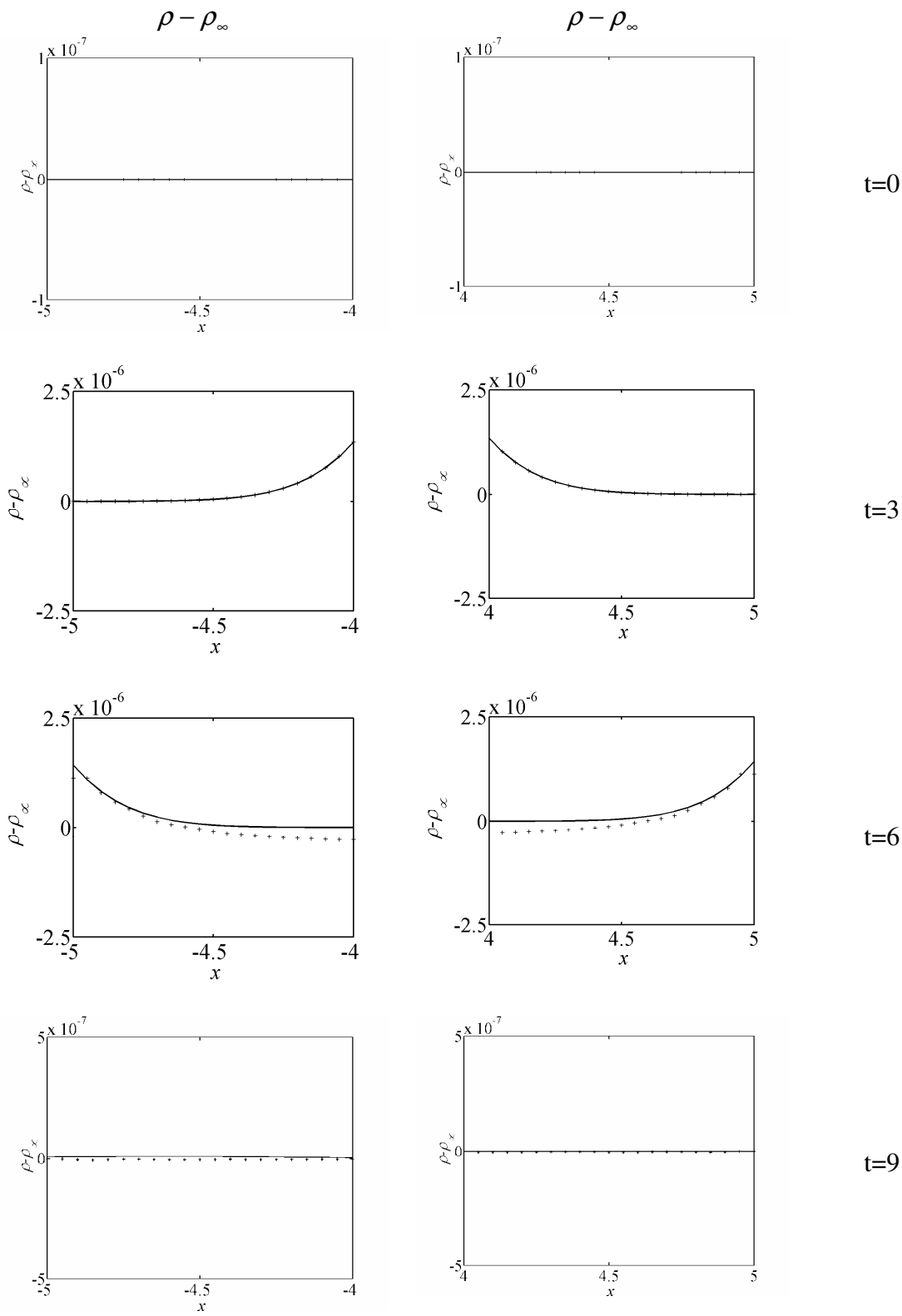

Figure 4.2(b) Enlarged snapshots of density fluctuation on left boundary, x = [-5,-4] and on right boundary, nx = [4,5] at t=0, t=3, t=6, t=9 with zeroth-ordered extrapolation boundary conditions (with filter) EM0/FM: +, LBM; ——, DNS.

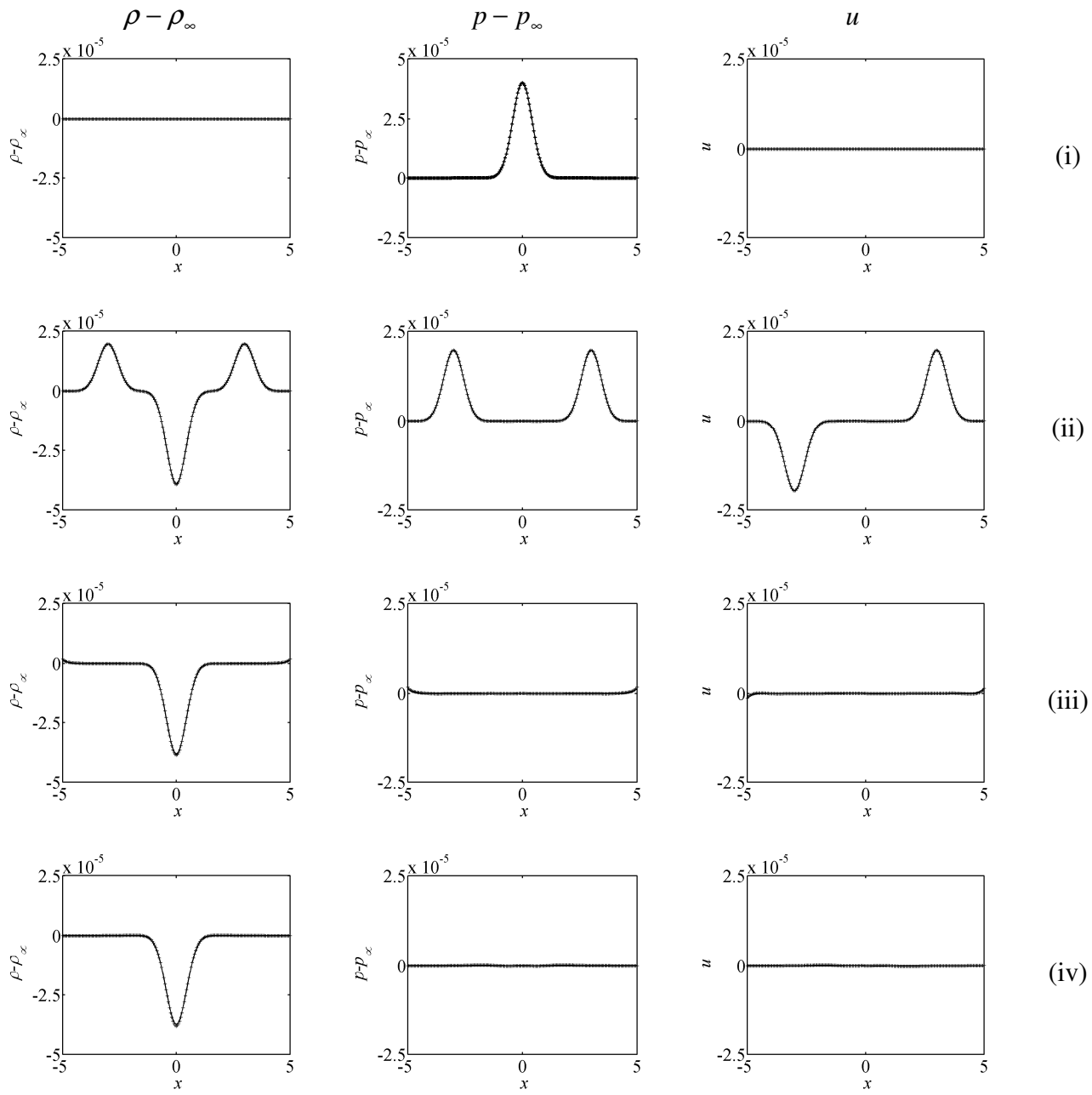

Figure 4.3(a) The density, pressure and velocity "u" fluctuations along the x-axis at four different *t* with first-ordered extrapolation boundary conditions (with filter) EM1/FM: +, LBM; ——, DNS.

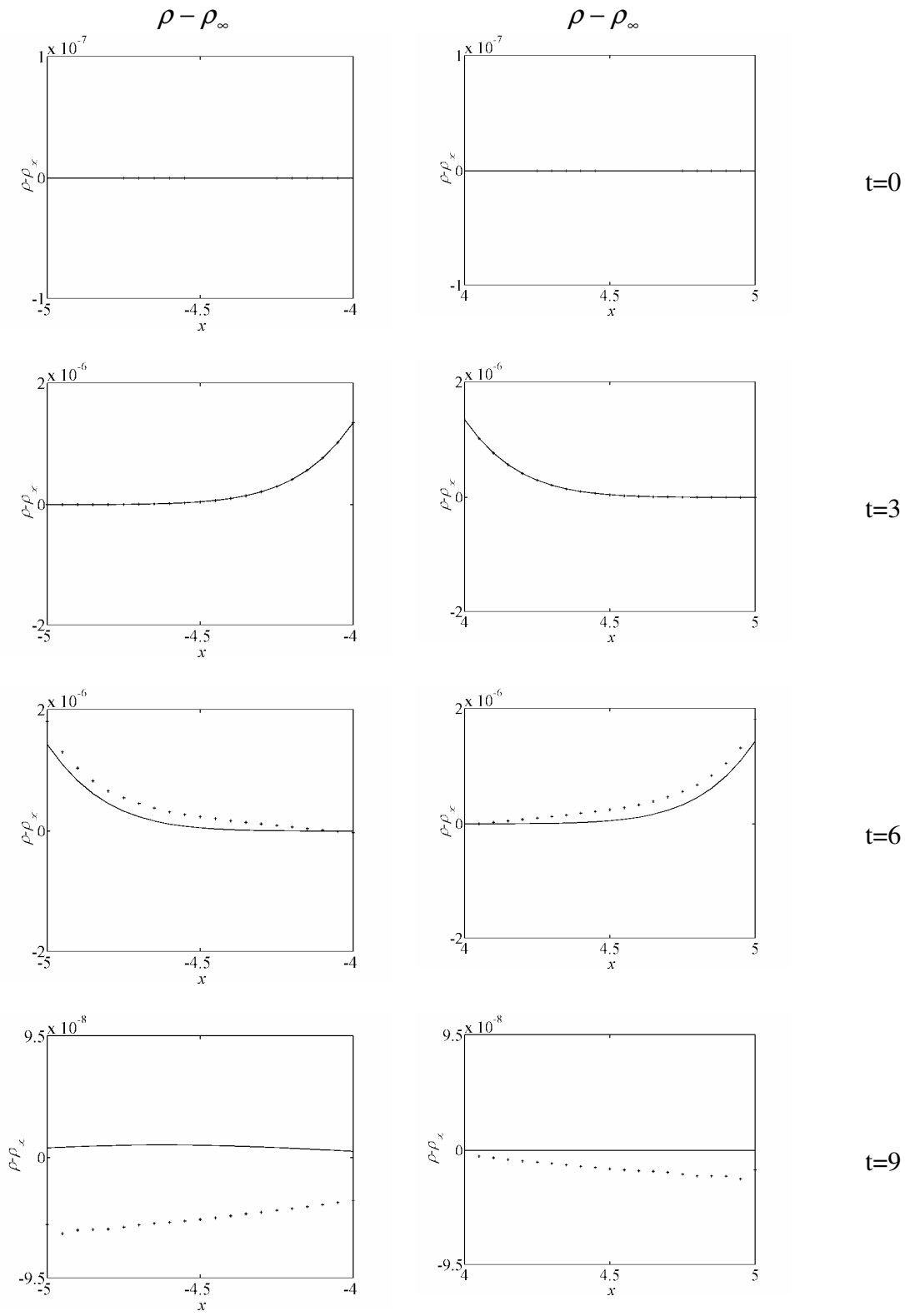

Figure 4.3(b) Enlarged snapshots of density fluctuation on left boundary, x = [-5,-4] and on right boundary, x = [4,5] at t=0, t=3, t=6, t=9 with first-ordered extrapolation boundary conditions (with filter) EM1/FM: +, LBM; ———, DNS.

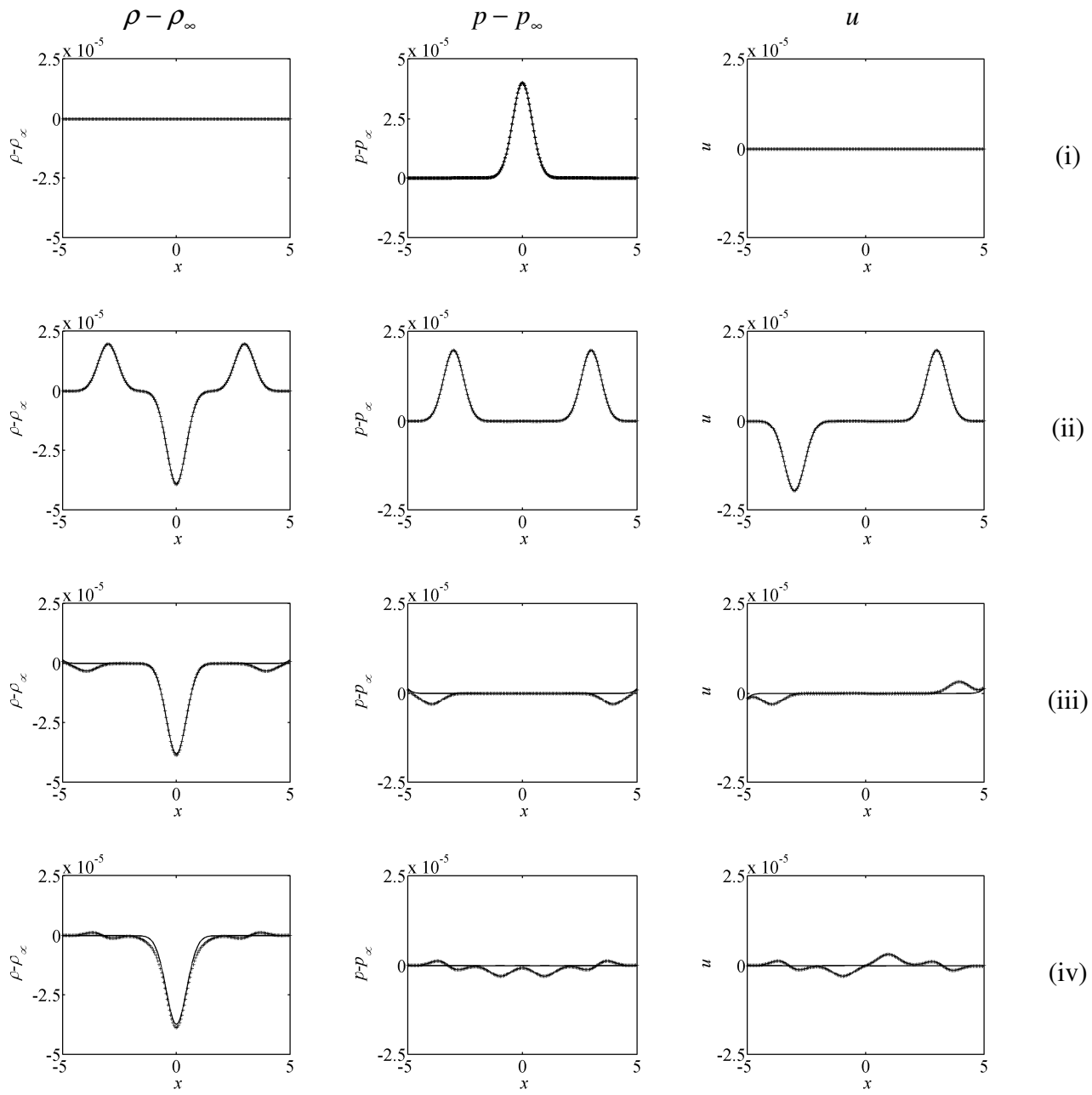

Figure 4.4(a) The density, pressure and velocity "u" fluctuations along the x-axis at four different t with C^1 boundary conditions: +, LBM; ———, DNS.

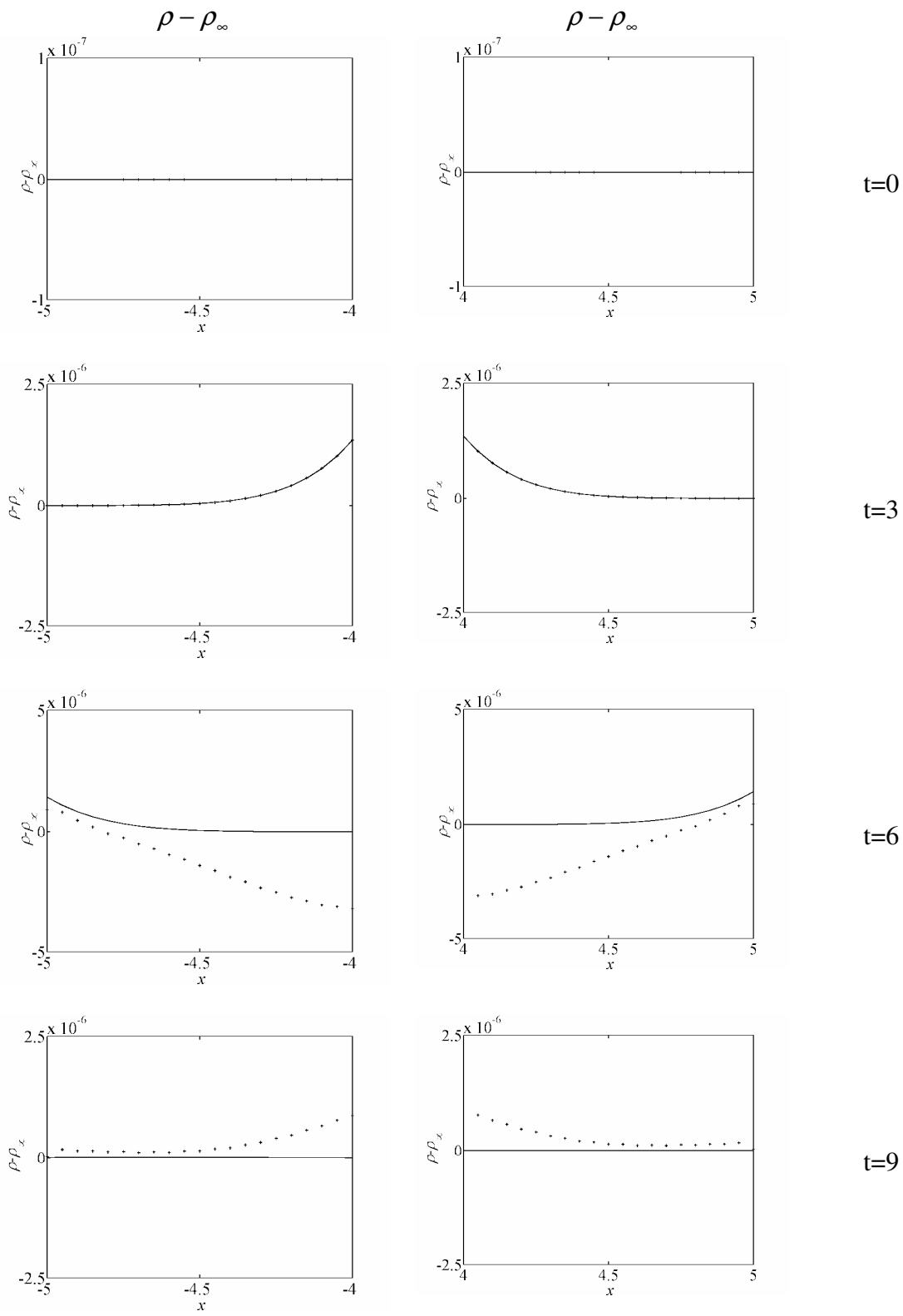

Figure 4.4(b) Enlarged snapshots of density fluctuation on left boundary, x = [-5,-4] and on right boundary, x = [4,5] at t=0, t=3, t=6, t=9 with C^1 boundary conditions: +, LBM; ——, DNS.

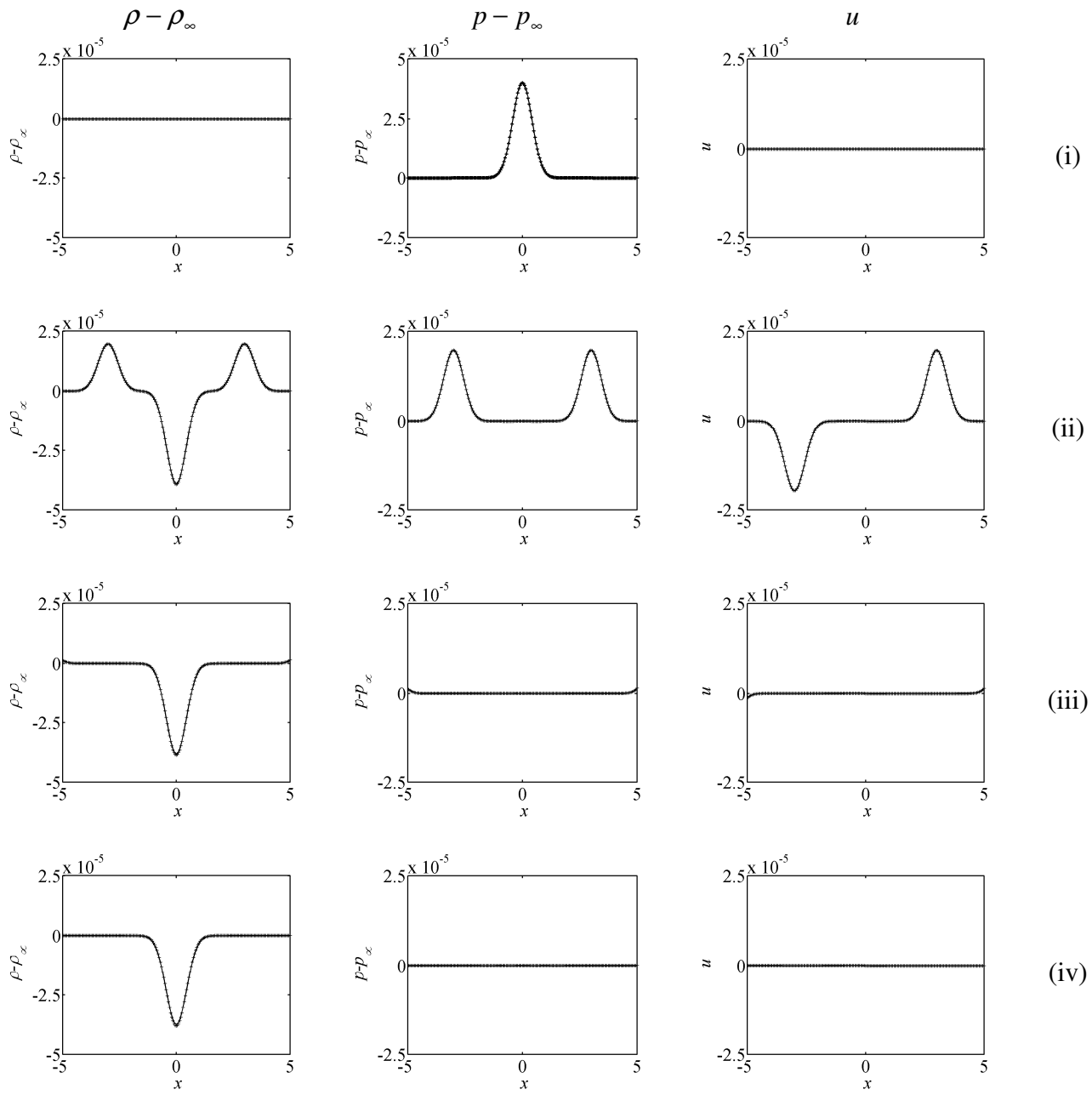

Figure 4.5(a) The density, pressure and velocity "u" fluctuations along the x-axis at four different t with absorbing boundary conditions: +, LBM; ———, DNS.

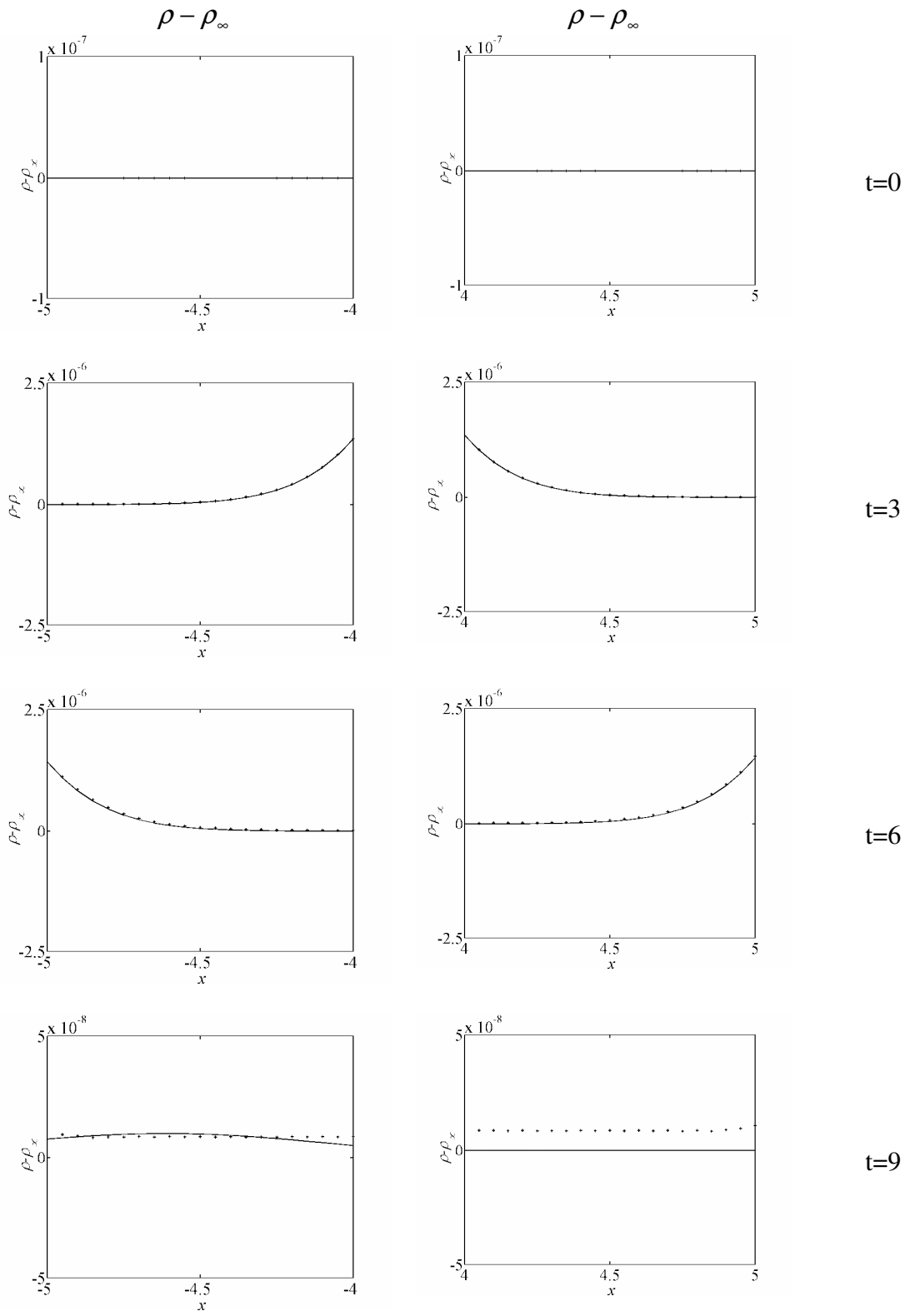

Figure 4.5(b) Enlarged snapshots of density fluctuation on left boundary, x = [-5,-4] and on right boundary, x = [4,5] at t=0, t=3, t=6, t=9 with absorbing boundary conditions: +, LBM; solid line, DNS.

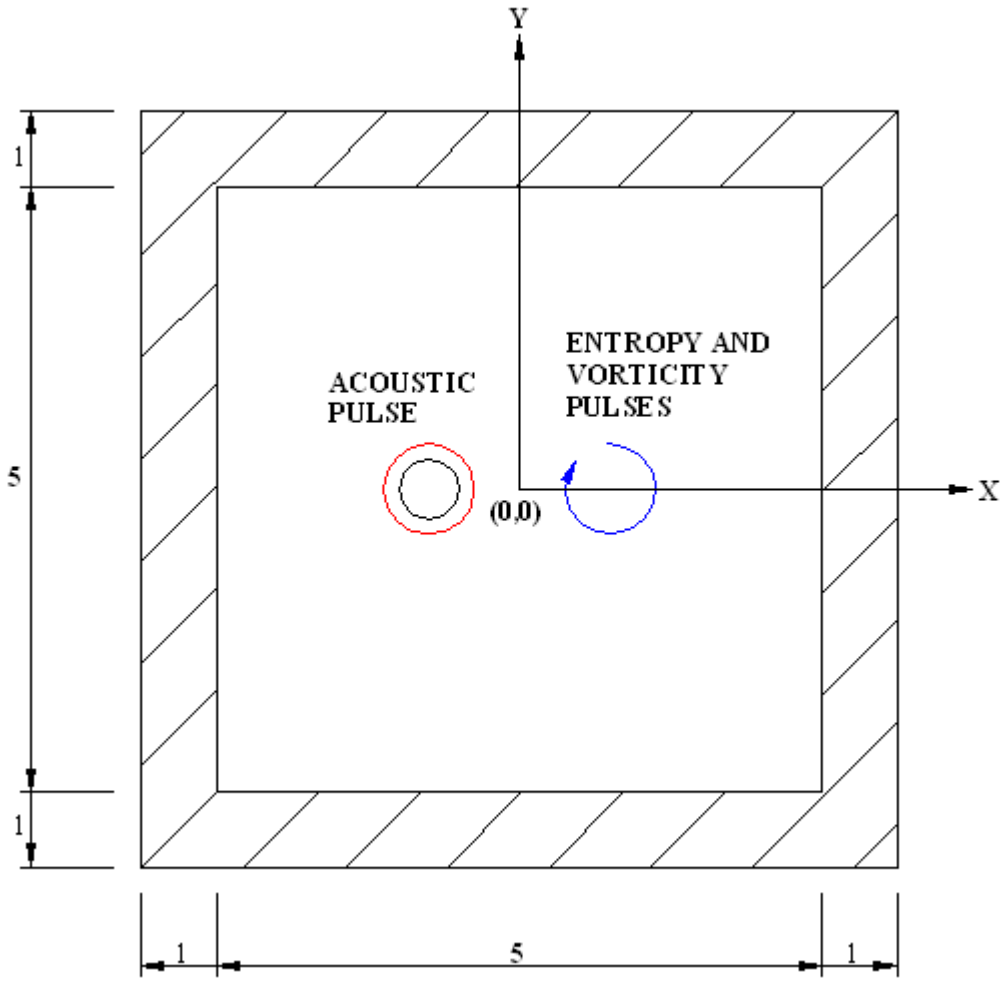

Figure 4.6 The acoustic, entropy and vorticity pulse propagation in a uniform stream configuration for Case 2 (hatched area as buffer region).

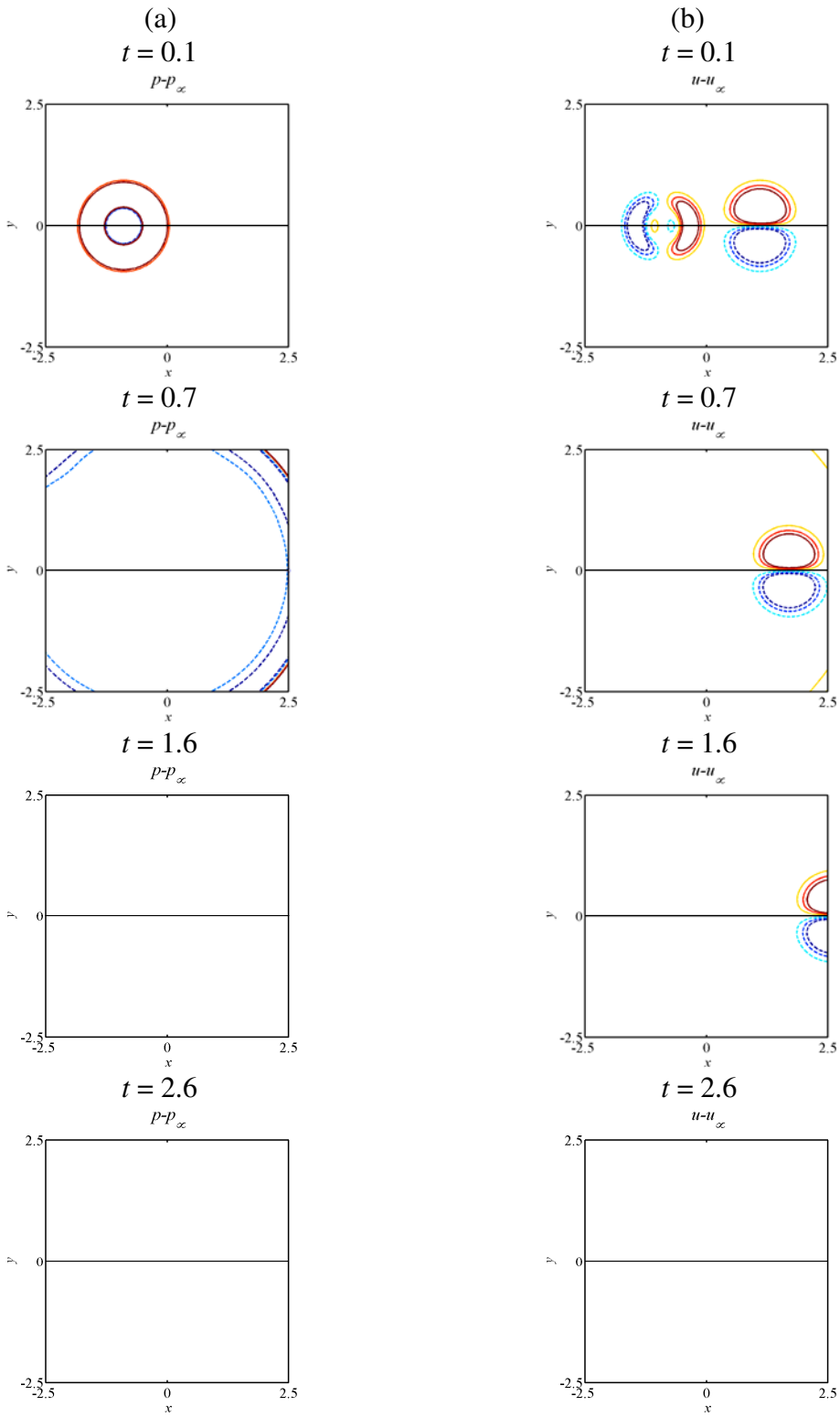

Figure 4.7 Comparison of LBM solutions using ABC (upper half) with DNS solutions (lower half): (a) pressure fluctuation (6 contours equally distributed between -5×10^{-5} and 5×10^{-5}); (b) streamwise velocity fluctuation (6 contours equally distributed between -6×10^{-5} and 6×10^{-5}).

Chapter 5

Theoretical Solution for Sound Scattering by a Localized Thermal Disturbance

5.1 Background

In the preceding chapters, physical models have been invoked for the correct recovery of the transport coefficients from the modeled BE. The correct values of the transport coefficient (μ, γ and κ) and their equivalent dimensionless numbers (Re, M and Pr) lead to recovery of the NS equations from the modeled BE. With appropriate specification of non-reflecting boundary conditions, the modeled BE is ready for use to solve practical aeroacoustic problems.

The improved modeled BE has been validated against aeroacoustic problems with no temperature variation in the flow medium (Li et al. 2006), and using different non-reflecting boundary conditions in Chapter 4. In these validations, the Re and M are recovered correctly. However, up to this point, the modeled BE has not been validated against any aeroacoustic problem where there is a temperature gradient in the flow medium. Therefore, it is not possible at this point to claim that the improved modeled BE could also replicate κ or Pr correctly. In view of this, an acoustic scattering problem with significant thermal gradient would be selected for investigation, from which the ability to resolve thermal effect by the modeled BE could be investigated.

In general, there are three modes of motion in a slightly disturbed viscous heat conducting gas (Trilling 1955); namely acoustic (pressure),

entropy (thermal) and vorticity (velocity) waves. Among these, the flow-sound interaction involved in the scattering of sound waves by vortices has received great attention. Numerous attempts have been made to study sound scattering by vortices and the corresponding experimental, analytical and numerical results are well documented (Georges 1972, Müller and Matschat 1959, Morse and Uno Ingard 1968, Colonius et al. 1994). According to Colonius et al. (1994), the ratio of the incident acoustic wavelength to the size of the vortex is a critical parameter that has substantial effect on the scattered field. Two types of limit are discovered based on this ratio (Ford and Llewellyn Smith 1999). If the incident acoustic wavelength is small compared with the size of the vortex, it is referred to as the WKB limit, while it is referred to as the Born limit if the opposite is true. With reference to Morse and Uno Ingard (1968), scattered wave is defined as the wave given rise by the difference of two waves; one resulting from the interaction between the acoustic wave and the obstacle, and the other is the undisturbed wave in the absence of the obstacle. If scattering by an obstacle is closed to the WKB limit, only half of the scattered wave spreads out nearly isotropically from the obstacle, the other half interferes destructively with the incident plane wave behind it to form a sharp-edged shadow. On the other hand, if it is closed to the Born limit, all of the scattered wave spreads out in every directions and no sharp-edged shadow is observed. However, different scattered fields can be obtained if the incident acoustic wavelengths lie between the two limits; these scattering results are known as the intermediate cases. The interaction for all three cases is non-linear in nature; however, it is

the most vigorous for the intermediate cases, as the incident acoustic wavelengths are comparable with the size of the obstacle.

Study of sound scattering in the two limits has been carried out by various researchers. Georges (1972) used high frequency ray tracing techniques for the WKB limit, while Müller and Matschat (1959) considered the Born limit using a distributed vortex with velocity discontinuities. Their study was followed by the investigations of Ferziger (1974), O'Shea (1975), Howe (1975), Yates (1978) and Candel (1979). Numerical and analytical solutions of the NS equations were obtained by Colonius et al. (1994) using distributed vortices with and without circulation. Furthermore, Ford and Llewellyn Smith (1999) investigated the scattering of a plane acoustic wave by an axisymmetric vortex with localized vorticity, arbitrary circulation and small Mach numbers.

On the other hand, thermal-acoustic interaction has drawn much attention among researchers in the aerospace industry. This is due to the fact that instability can be introduced into the flow by a fluctuating transfer of heat (Mawardi 1956), causing and maintaining oscillation. For example, the Rijke phenomenon. Sound attenuation under favorable heat conditions (Bass 1981) is also made possible. Most of the problems being studied, however, are concentrated in thermal induced noise or computation of thermal effect on the absorption ability of air (Bass 1981). Trilling (1955) showed that an instantaneous temperature rise due to an infinitely long plane wall could induce an acoustic wave. Farouk et al. (2000) investigated numerically a thermally induced acoustic wave in a two-dimensional cavity by either heating

up or cooling down the vertical walls of the cavity. The Rijke phenomenon (1859), where sound is generated by airflow through a sufficiently long vertical open-ended tube with a hot wire net in its lower part, has been studied qualitatively by Rayleigh (1945) and quantitatively by Landa (1996).

Apart from the above cases, sound scattering due to thermal acoustic interaction has not gained much attention, especially in a flowing medium. In view of this, the ability of the improved modeled BE to correctly resolve the thermal scattering effect in a problem similar to the one of acoustic wave scattering by a zero circulation vortex in a quiescent medium will be investigated. The thermal problem is set up by considering acoustic waves propagating towards a localized thermal disturbance with zero heat gain/loss. Thus, the scattering of the acoustic waves will be affected by the thermal disturbance alone. Since there is no mean flow present, the scattering effect is purely due to the thermal field generated by the localized thermal disturbance. Therefore, this problem is set up with much similarity to the scattering of acoustic waves by a zero circulation vortex.

In principle, this problem could be made even simpler by considering the line heat source to extend to infinity, thus the problem will become 2-D in nature and by further assuming the quiescent medium to be isothermal. Thus formulated, the thermal acoustic scattering problem is very similar to the vortex scattering problem treated by numerous researchers and briefly discussed above. Furthermore, the heat conduction solution in the absence of an incident acoustic wave could be obtained and the thermal effect on the scattering of the acoustic wave could be easily delineated. One would have

thought that a classic solution of this relatively simple problem would be available in the literature; however, after extensive search, no such solution was found. In order to verify the numerical solution obtained by solving the modeled BE, an analytical solution would be most desirable. Therefore, this chapter and the succeeding one would be devoted to a search for an analytical solution of this thermal scattering of acoustic waves by a localized thermal disturbance. These two chapters are organized as follows. A theoretical solution of the acoustic scattering problem will be attempted in this chapter and serves as a foundation for the validation of the improved modeled BE. The numerical solution of the modeled BE using either the lattice method or gas-kinetic method would be obtained for comparison in the chapter following this one.

5.2 Theoretical Solution of the Acoustic Scattering Problem

The acoustic scattering problem consists of two main components: the localized thermal disturbance and the incident acoustic waves. Originally, a line heat source was assumed for the acoustic scattering problem. Difficulties were encountered in the course of attempting to obtain an analytical solution to the steady state thermal problem. The theoretical solution proofed to be quite difficult, if not impossible. In the following, it would be shown that a line heat source is not quite suitable for the acoustic scattering investigation, because a steady state solution to the thermal problem could not be obtained analytically. Consequently, a distributed thermal disturbance was attempted. A distributed thermal disturbance is obtained by structuring the temperature distribution, such that the overall heat loss/gain would be zero (similar to the

case of a zero circulation vortex where lift is absent), and the distributed thermal disturbance is therefore stationary with respect to time for the ease of steady state solution calculation. This model for the thermal disturbance proofed to be quite manageable for the acoustic scattering problem and it was feasible to derive a steady state solution for the thermal problem. The corresponding sketch for the acoustic scattering problem is shown in Figure 5.1.

In the following analysis, the variables are made dimensionless using the following characteristic scaling parameters (dimensional quantities are denoted by an asterisk, *):

Length scale: wavelength of the incident pressure disturbance, L

Velocity scale: speed of sound, a_∞ where $a_\infty^2 = \gamma R T_\infty = \dfrac{\gamma P_\infty}{\rho_\infty}$

Time scale: $\dfrac{L}{a_\infty}$

Temperature scale: T_∞

Density scale: ρ_∞

With these characteristic scaling parameters, the following dimensionless variables can be defined. They are

Density: $\rho = \dfrac{\rho^*}{\rho_\infty}$

Temperature: $T = \dfrac{T^*}{T_\infty}$

Pressure: $P = \dfrac{P^*}{\rho_\infty a_\infty^2}$

Two regions can be identified for the acoustic scattering problem, namely the inner or scattered region, and the outer or incident wave region. The theoretical solution would be obtained by asymptotic analysis, in which the inner solution is matched with the outer one at the interface. The corresponding regions are analyzed in the following subsections.

5.2.1 Theoretical Solution for a Localized Thermal Disturbance in a Quiescent Environment

In a quiescent environment, the localized thermal disturbance is governed by a set of time independent non-dimensional conservation laws; these are the conservation laws for mass, linear momentum and energy. In 2-D polar coordinates, they can be written as

$$\frac{\partial(\rho v_r)}{\partial r} + \frac{\rho v_r}{r} = 0 \quad , \tag{5.1}$$

$$\rho v_r \frac{\partial v_r}{\partial r} = -\frac{\partial p}{\partial r} + \frac{\partial \sigma_{rr}}{\partial r} + \frac{\sigma_{rr}}{r} \quad , \tag{5.2}$$

$$c_v \rho v_r \frac{\partial T}{\partial r} = -p\left(\frac{\partial v_r}{\partial r} + \frac{v_r}{r}\right) + \kappa \nabla^2 T + Q \quad , \tag{5.3}$$

where ρ is density, v_r is the radial velocity, p is pressure, σ_{rr} is the shear stress, T is temperature, κ is the coefficient of heat conduction, and $Q = Q(r)$ is the thermal disturbance distribution.

The steady state solution of equations (5.1), (5.2) and (5.3) can be assumed to be

$$v_r = 0\,;\ p = p_\infty\,;\ T = \overline{T}(r);\ \rho = \overline{\rho}(r) = \frac{p_\infty}{R\overline{T}(r)} \quad . \tag{5.4}$$

It can be shown that equations (5.1) and (5.2) are identically satisfied and equation (5.3) is reduced to

$$\nabla^2\left(\overline{T}(r)\right) = -\frac{Q(r)}{\kappa} \qquad \text{or} \qquad \frac{1}{r}\frac{d}{dr}\left(r\frac{d\left(\overline{T}(r)\right)}{dr}\right) = -\frac{Q(r)}{\kappa}$$

Integrating once gives

$$r\frac{d\overline{T}(r)}{dr} = -\int_0^r \frac{Q(r')}{\kappa} r' dr'$$

Integrating again gives

$$\overline{T}(r) = -\int_0^r \frac{1}{r'}\int_0^{r'} \frac{Q(r'')}{k} r'' dr'' + \int_0^{\infty} \frac{1}{r'}\int_0^{r'} \frac{Q(r'')}{k} r'' dr'' + T_{\infty}$$

$$= -\int_r^{\infty} \frac{1}{r'}\int_0^{r'} \frac{Q(r'')}{k} r'' dr'' + T_{\infty} \quad . \tag{5.5}$$

For a line heat source,

$$Q(r) = \frac{\delta(r)}{4\pi r} \quad . \tag{5.6}$$

Substitute equation (5.6) into equation (5.5) gives

$$\overline{T}(r) = \int_r^{\infty} \frac{1}{r'}\frac{1}{4\pi\kappa} dr' + T_{\infty} = \frac{1}{4\pi\kappa} ln(r)\Big|_r^{\infty} + T_{\infty} \quad .$$

As $r \to \infty$, $ln(r)$ becomes unbounded and therefore the steady state solution cannot be obtained by assuming a line heat source given by equation (5.6), or $Q(r) = \frac{\delta(r)}{4\pi r}$.

In order to avoid the divergence as $r \to \infty$, a distributed thermal disturbance with total source strength given by

$$\int_0^{\infty} Q(r) r dr = 0 \quad , \tag{5.7}$$

is assumed. After some tedious algebra, the corresponding distributed thermal disturbance, $Q(r)$, can be determined to be given by the following expressions (the corresponding distributions are shown in Figure 5.2):

$$Q(r)=\begin{cases} Q_1(r)=1 & ,r\le r_1 \\ Q_2(r)=C_0+(1-C_0)e^{-\left(\frac{r-r_1}{b_1}\right)^2} & r_1\le r\le r_2 \\ Q_3(r)=C_1\left(1-e^{\left(\frac{r_3-r_2}{b_2}\right)^2-\left(\frac{r-r_3}{b_2}\right)^2}\right) & r_2\le r\le r_3 \\ Q_4(r)=C_3e^{\left(\frac{r_3-r_2}{b_2}\right)^2-\left(\frac{r-r_3}{b_3}\right)^2} & r_3\le r \end{cases} , \tag{5.8}$$

where $r_1=0.5;\ r_2=1.5;\ r_3=2.0;$

$b_1=1.0;\ b_2\approx 0.6401;\ b_3=0.5;$

$C_0=e^{-1}/\left(e^{-1}-1\right)\approx 0.5820;\ C_1\approx 0.4769;\ C_3\approx 0.2178$

In order to visualize sound scattering by this localized thermal disturbance, $Q(r)$ is taken to be bounded at about $r=3.0$. The corresponding temperature distribution is therefore determined by equation (5.5) and is shown in Figure 5.3; the density distribution is derived from $\overline{\rho}=\overline{\rho}(r)=\frac{p_\infty}{R\overline{T}(r)}$ and is shown in Figure 5.4. Thus derived, the localized thermal disturbance is without singularity at origin, and the divergency as $r\to\infty$ is avoided.

5.2.2 Theoretical Solution for Acoustic Scattering by a Localized Thermal Disturbance

In the absence of acoustic waves, the mean thermal field due to a localized heat source is given by

$$\bar{v}_r = \bar{v}_\phi = 0\,;\ \bar{p} = p_\infty\,;\ \bar{\rho} = \bar{\rho}(r) = \frac{p_\infty}{R\bar{T}(r)}$$

The acoustic field is governed by the linearized Euler Equations (LEE). It is assumed that the distributed thermal disturbance is not affected by the incident acoustic waves. In other words, the non-linear interaction between the incident sound waves and the localized thermal disturbance is assumed to be negligible, such that the LEE is valid for the theoretical analysis. In polar coordinates, macroscopic properties (ρ, v_r, v_ϕ, p) in the LEE can be expressed as

$$\frac{\partial \rho}{\partial t} + \bar{\rho}\frac{\partial v_r}{\partial r} + v_r\frac{\partial \bar{\rho}}{\partial r} + \bar{\rho}\frac{v_r}{r} + \frac{\bar{\rho}}{r}\frac{\partial v_\phi}{\partial \phi} = 0 \quad , \tag{5.9}$$

$$\bar{\rho}\frac{\partial v_r}{\partial t} = -\frac{\partial p}{\partial r} \quad , \tag{5.10}$$

$$\bar{\rho}\frac{\partial v_\phi}{\partial t} = -\frac{1}{r}\frac{\partial p}{\partial \phi} \quad , \tag{5.11}$$

$$\frac{\partial p}{\partial t} + \gamma p_\infty\left(\frac{\partial v_r}{\partial r} + \frac{v_r}{r} + \frac{1}{r}\frac{\partial v_\phi}{\partial \phi}\right) = 0 \quad . \tag{5.12}$$

Suppose the incident acoustic waves have a single frequency ω, a separation of variable technique can be used to factor out the time dependence. Consequently, ρ, v_r, v_ϕ and p can be expressed as

$$\begin{bmatrix} \rho \\ v_r \\ v_\phi \\ p \end{bmatrix} = Re\left\{\begin{bmatrix} \hat{\rho}(r,\phi) \\ \hat{v}_r(r,\phi) \\ \hat{v}_\phi(r,\phi) \\ \hat{p}(r,\phi) \end{bmatrix} e^{-i\omega t}\right\} \quad , \tag{5.13}$$

where $\hat{\rho}$, $\hat{v}_r$, $\hat{v}_\phi$ and $\hat{p}$ are the total fluctuation of density, velocities in polar co-ordinates and pressure, respectively. Equations (5.10), (5.11) and (5.12) form a closed system and $\left(\hat{v}_r, \hat{v}_\phi, \hat{p}\right)$ are expressed as

$$\hat{v}_r = \frac{1}{i\omega\bar{\rho}}\frac{\partial \hat{p}}{\partial r} \quad , \tag{5.14}$$

$$\hat{v}_\phi = \frac{1}{i\omega\bar{\rho}r}\frac{\partial \hat{p}}{\partial \phi} \quad , \tag{5.15}$$

$$-i\omega\hat{p} + \gamma p_\infty\left(\frac{\partial \hat{v}_r}{\partial r} + \frac{\hat{v}_r}{r} + \frac{1}{r}\frac{\partial \hat{v}_\phi}{\partial \phi}\right) = 0 \quad . \tag{5.16}$$

where $\hat{\rho}$ can be determined subsequently by substituting the solution of $\hat{v}_r, \hat{v}_\phi, \hat{p}$ into equation (5.10). A single equation for $\hat{p}$ can be obtained by substituting equations (5.14) and (5.15) into equation (5.16); the result is

$$\frac{\partial^2 \hat{p}}{\partial r^2} + \left(\frac{1}{r} - \frac{1}{\rho}\frac{d\rho}{dr}\right)\frac{\partial \hat{p}}{\partial r} + \frac{1}{r^2}\frac{\partial^2 \hat{p}}{\partial \phi^2} + \frac{\rho\omega^2}{\gamma p_\infty}\hat{p} = 0 \quad . \tag{5.17}$$

As $r \to \infty$, $\rho \to \rho_\infty$, equation (5.17) can be written as

$$\frac{\partial^2 \hat{p}}{\partial r^2} + \frac{1}{r}\frac{\partial \hat{p}}{\partial r} + \frac{1}{r^2}\frac{\partial^2 \hat{p}}{\partial \phi^2} + \frac{\omega^2}{a_\infty^2}\hat{p} = 0 \text{ where } a_\infty^2 = \frac{\gamma p_\infty}{\rho_\infty} \quad . \tag{5.18}$$

In Cartesian coordinates, equation (5.18) becomes

$$\frac{\partial^2 \hat{p}}{\partial x^2} + \frac{\partial^2 \hat{p}}{\partial y^2} + \frac{\omega^2}{a_\infty^2}\hat{p} = 0 \quad . \tag{5.19}$$

For a plane incident wave with amplitude *A* propagating in the *x*-direction, the incident pressure can be written as

$$\hat{p}_i = Ae^{i\frac{\omega}{a_\infty}x} \text{ (Cartesian coordinates)} \quad , \tag{5.20a}$$

$$\hat{p}_i = Ae^{i\frac{\omega}{a_\infty} r\cos\varphi} = A\sum_{m=0}^{\infty} i^m \varepsilon_m J_m\left(\frac{\omega r}{a_\infty}\right)\cos m\varphi \text{ (Polar coordinates), (5.20b)}$$

where $J_m\left(\frac{\omega r}{a_\infty}\right)$ is the Bessel function of order m, $\varepsilon_0 = 1; \varepsilon_m = 2; m = 1, 2, 3,\ldots$.

The solution for $\hat{p}$ in equation (5.17) can be obtained in three regions as follows:

5.2.2.1 Solution for $\hat{p}$ in region I - $0 < r \le r_1$, $(r_1 << 1)$

Suppose $\hat{p}_s$ is the scattered waves. The solution for equation (5.17) can therefore be expanded in a Fourier series as

$$\hat{p} = \hat{p}_i + \hat{p}_s = \sum_{m=0}^{\infty} D_m f_m(r)\cos m\varphi \quad . \tag{5.21}$$

In order to determine $f_m(r)$, equation (5.21) is substituted into equation (5.17), with the coefficient of the Fourier cosine series set to zero. The result is

$$\frac{d^2 f_m}{dr^2} + \left(\frac{1}{r} - \frac{1}{\bar{\rho}}\frac{d\bar{\rho}}{dr}\right)\frac{df_m}{dr} + \left(\frac{\rho\omega^2}{\gamma p_\infty} - \frac{m^2}{r^2}\right) f_m = 0 \quad , \tag{5.22}$$

where f_m must be finite as $r \to 0$.

In region I, equation (5.22) is further reduced to

$$\frac{d^2 f_m}{dr^2} + \frac{1}{r}\frac{df_m}{dr} + \left(\omega_0^2 - \frac{m^2}{r^2}\right) f_m = 0 \quad , \tag{5.22a}$$

where $\omega_0^2 = \frac{\rho(0)\omega^2}{\gamma p_\infty}$ with solution for f_m is expressed as

$$f_m(r) = r^m, \tag{5.22b}$$

which is used as the starting value for marching the solution from $r = r_1$ to $r = r_2$. Note that there is an arbitrary constant factor taken to be equal to 1 in this solution for f_m, with the consequence being absorbed to the coefficient D_m which has to be determined.

5.2.2.2 Solution for $\hat{p}$ in region II - $r_1 < r \le r_2$

In this region, r_2 is taken to be greater than, but close to 3.0, where the thermal disturbance is localized at $r \le 3$ and the density is essentially at its uniform value outside this region. Again, $\hat{p}$ can be expressed as equation (5.21) and f_m is obtained by solving equation (5.22).

5.2.2.3 Solution for $\hat{p}$ in region III - $r_2 < r < \infty$

In this region, the scattered waves should be an outgoing wave which can be expressed as

$$\hat{p}_s = A\sum_{m=0}^{\infty} i^m \varepsilon_m f_m(r) \cos m\varphi \quad , \tag{5.23}$$

where

$$f_m = B_m H_m^{(1)}\left(\frac{\omega r}{a_\infty}\right) \quad . \tag{5.24}$$

Here, B_m is a constant to be determined for every mode and $H_m^{(1)}$ is the Hankel function of the first kind (Abramowitz and Stegun 1965). Therefore, $\hat{p}$ in equation (5.17) is in the form:

$$\hat{p} = \hat{p}_i + \hat{p}_s = A\sum_{m=0}^{\infty} i^m \varepsilon_m \left[J_m\left(\frac{\omega r}{a_\infty}\right) + B_m H_m^{(1)}\left(\frac{\omega r}{a_\infty}\right)\right] \cos m\varphi \quad . \tag{5.25}$$

Since $\overline{\rho}(r) \approx \rho_\infty$ in this region, equation (5.22) is reduced to

$$\frac{d^2 f_m}{dr^2} + \frac{1}{r}\frac{df_m}{dr} + \left(\omega_1^2 - \frac{m^2}{r^2} \right) f_m = 0 , \tag{5.26}$$

where $\omega_1^2 = \dfrac{\rho(r_2)\omega^2}{\gamma p_\infty}$ at $r = r_2$, providing an initial data for determining the constant B_m.

5.2.2.4 Patching of solutions for $\hat{p}$ at $r = r_2$

The solution of $\hat{p}$ in equation (5.17) can be determined by patching the corresponding solutions obtained in region II and region III at $r = r_2$, where r_2 is defined such that $\rho = \overline{\rho}(r_2) \approx \rho_\infty$. Combining equations (5.21) and (5.25), $\hat{p}$ becomes

$$\hat{p} = \hat{p}_i + \hat{p}_s = \begin{cases} \displaystyle\sum_{m=0}^{\infty} D_m f_m(r) \cos m\varphi & , \quad r \le r_2 \\ \displaystyle A\sum_{m=0}^{\infty} i^m \varepsilon_m \left[J_m\left(\frac{\omega r}{a_\infty}\right) + B_m H_m\left(\frac{\omega r}{a_\infty}\right) \right] \cos m\varphi & , \quad r \ge r_2 \end{cases} .$$

At $r = r_2$, f_m and df_m / dr should be continuous, and the coefficients on the left hand side (LHS) and right hand side (RHS) of the cosine series should be equal for every mode. Therefore, for $0 \le m < \infty$,

$$D_m f_m = i^m \varepsilon_m A \left(J_m\left(\frac{\omega r}{a_\infty}\right) + B_m H_m^{(1)}\left(\frac{\omega r}{a_\infty}\right) \right) \quad , \tag{5.26}$$

$$D_m \frac{df_m}{dr} = i^m \varepsilon_m A \left(\frac{dJ_m\left(\dfrac{\omega r}{a_\infty}\right)}{dr} + B_m \frac{dH_m^{(1)}\left(\dfrac{\omega r}{a_\infty}\right)}{dr} \right) \quad . \tag{5.27}$$

In order to evaluate f_m, the initial value problem is solved numerically using a 4th order Runge-Kutta Scheme. At $r = r_1$, the solution of f_m and df_m / dr are obtained from equation (5.22b) and are used as initial values for marching to $r = r_2$.

At $r = r_2$, both the Bessel function and the Hankel function can be determined, so that the unknown constants B_m and D_m are computed for every mode by solving equations (5.26) and (5.27). The result is

$$B_m = \frac{\left(J_m'\left(\frac{\omega r}{a_\infty}\right) \cdot \frac{\omega}{a_\infty} \cdot f_m - J_m\left(\frac{\omega r}{a_\infty}\right) \frac{df_m}{dr} \right)}{H_m^{(1)}\left(\frac{\omega r}{a_\infty}\right) \frac{df_m}{dr} - H_m^{(1)'}\left(\frac{\omega r}{a_\infty}\right) \cdot \frac{\omega}{a_\infty} \cdot f_m} \quad , \tag{5.31}$$

$$D_m = \frac{i^m \varepsilon_m A \left[\left(J_m \cdot H_m^{(1)'}\left(\frac{\omega r}{a_\infty}\right) \cdot \frac{\omega}{a_\infty} - J_m' \cdot \frac{\omega}{a_\infty} \cdot H_m^{(1)'}\left(\frac{\omega r}{a_\infty}\right) \right) \right]}{f_m H_m^{(1)'}\left(\frac{\omega r}{a_\infty}\right) \cdot \frac{\omega}{a_\infty} - \frac{df_m}{dr} H_m^{(1)}\left(\frac{\omega r}{a_\infty}\right)} \quad . \tag{5.32}$$

The corresponding f_m is therefore determined for every mode ($0 \le m < \infty$), and the pressure distribution $\hat{p}(r)$ can be calculated.

5.3 Discussion of Results

Two limiting cases with different wavelengths, λ^*, are attempted for the sound scattering problem. Here, λ^* is taken to be a dimensional parameter. For acoustic scattering problems, the resulting scattering pattern can be classified by the ratio between the incident acoustic wavelength, λ^*, and the characteristic length of the obstacle (in this case the obstacle is the distributed

thermal disturbance). In general, it can be defined by the Helmholz number $H_n = kl$, where $k = 2\pi / \lambda^*$ is the wavenumber and l is the characteristic length of the thermal disturbance. Therefore, the two cases chosen are Case (1) $\lambda = \lambda^* / l = 2\pi / H_n = 1/3$ and Case (2) $\lambda = \lambda^* / l = 2\pi / H_n = 10/3$.

Since the distributed thermal disturbance is bounded at $r = 3.0$, the appropriate characteristic length for the thermal disturbance should be $l = r$. The incident acoustic wavelength is λ^*, therefore, H_n for Case (1) is $H_n = 3(2\pi) = 6\pi$ and its corresponding value for Case (2) is $H_n = 3\pi/5 = 0.6\pi$. The first case can be regarded as the short-wavelength (or high frequency) limit or the WKB limit, and the second case can be referred to as the long-wavelength (or low frequency) limit or the Born limit. Since the non-linear interaction is not accounted for by the theoretical solution, the intermediate cases, whose non-linear interaction should be taken account for, are not presented in this chapter. The theoretical solution for the acoustic scattering problem is obtained numerically with incident acoustic wave amplitude specified as $A = 1\times10^{-4}$. The centre of the distributed thermal disturbance is located at $(x, y) = (0, 0)$ as shown in Figure 5.1. Since the wavelength of the incident acoustic wave is the characteristic length, cases with different λ^* are made by re-scaling the size of the distributed thermal disturbance computationally. Therefore, sizes of the computational domain should be the same for both cases, while the physical phenomena illustrated by different λ are accomplished by re-scaling the size of the distributed thermal disturbance. However, the computational domain has to be big

enough to allow the solution to be resolved accurately. These two cases are discussed below.

Case (1) $\lambda = 1/3$

The grid sizes are specified as $\Delta x = \Delta y = 5\times10^{-2}$ and there are a total number of grid points of 400×400 in the computational domain. This choice is equivalent to a physical domain size of $-10 \le x \le 10; -10 \le y \le 10$. The incident acoustic wave is specified at $x = -10$. The initial conditions of the pressure and density of the incident acoustic waves, $\hat{p}_i$ and $\hat{\rho}_i$, are shown in Figure 5.5(a) and 5.6(a), respectively.

In this case, the radius of the distributed thermal disturbance is 3 times the incident acoustic wavelength, i.e., $\lambda^* / r = 1/3$; therefore, it can be regarded as the WKB limit**.** According to Morse and Uno Ingard (1968), this is not a common case in sound scattering. However, it is expected that the scattering behavior would be distinct from that for long wavelength limit. It is therefore worth study both short and long wavelength limit for better understanding of this acoustic scattering problem.

The contour of the resulting pressure fluctuation $\hat{p}$ is shown in Figure 5.7(a). As shown in Figure 5.7(a), a sharp-edged shadow is created behind the distributed thermal disturbance for this short-wavelength scattering problem. The presence of a sharp-edged shadow in the forward scattering direction (downstream direction) agreed with the theoretical prediction of sound scattering in the short-wavelength limit (Morse and Uno Ingard 1968). It is stated that for this short-wavelength limit (WKB limit), the sharp-edged

shadow formed behind the obstacle (distributed thermal disturbance) is resulted from the interaction between the scattered wave and the undisturbed plane acoustic waves behind the obstacle. The scattered wave is defined as the "interfering wave", which interferes destructively with the undisturbed plane acoustic waves downstream. This interfering wave makes up half of the total scattered wave, where the other half regarded as "reflected waves" spread out nearly uniformly in all directions.

The contour of the resulting density fluctuation $\hat{\rho}$ is shown in Figure 5.8(a). With reference to equations (5.9) to (5.12) $\hat{p} = a_\infty^2 \hat{\rho}$, therefore, the scattering pattern of $\hat{\rho}$ is the same as that for $\hat{p}$. The contour of the resulting temperature fluctuation $\hat{T}$ is obtained via the equation of state and is shown in Figure 5.9(a).

The 2-D contours and the directivity pattern of the scattered pressure level $\hat{p}_s$ are shown in Figures 5.10(a) and 5.11(a), respectively. The corresponding variation of the scattering amplitude from $\theta = 0$ to $\theta = \pi$ along radii originated from the center of the thermal disturbance is illustrated in Figures 5.12(a) to 5.12(g). It can be clearly seen that peak scattering occurs along the axis of symmetry of the distributed thermal disturbance, accompanied by secondary peaks at approximately $\theta = \pm\frac{\pi}{6}$, with scattering amplitudes about half of that along the axis of symmetry. The reflection of the scattering waves is not significant for this WKB limit.

The 2-D contours and the directivity pattern of the scattered density level $\hat{\rho}_s$ are shown in Figures 5.14(a) and 5.15(a), respectively.

Since $\hat{p} = \hat{p}_i + \hat{p}_s$, $\hat{\rho} = \hat{\rho}_i + \hat{\rho}_s$ and $\hat{p}_i = a_\infty^2 \hat{\rho}_i$, the resulting directivity of $\hat{\rho}_s$ has the same amplitude as that for $\hat{p}_s$.

The 2-D contours and the directivity pattern of the scattered temperature level $\hat{T}_s$ are shown in Figures 5.16(a) and 5.17(a), respectively. The corresponding variation of the scattering amplitude from $\theta = 0$ to $\theta = \pi$ along radii originated from the center of the thermal disturbance is illustrated in Figures 5.18(a) to 5.18(g). The directivity pattern for $\hat{T}_s$ is similar to that for $\hat{p}_s$ and $\hat{\rho}_s$. However, the order of magnitude of the scattered temperature is 10^{-5}, which is 10^{-4} times the temperature variation of the distributed thermal disturbance (where the thermal difference within the distributed thermal disturbance has an order of magnitude of 10^{-1}).

The directivity pattern for the short-wavelength limit is found to be similar to that of sound scattering by a vortex pair composed of two Oseen vortices of opposite circulation (Berthet et al. 2000). However, no details of the theoretical derivation of the corresponding sound scattering problem was given in their paper, therefore, a quantitative comparison is not possible at this time.

Case (2) $\lambda = 10/3$

The grid sizes are given by $\Delta x = \Delta y = 5 \times 10^{-2}$ with a specified number of grid points 400×400 inside the computational domain. Re-scaling the size of the distributed thermal disturbance by 1/10 times that for Case 1, therefore, the computational domain represents a physical domain with size given by

$-100 \le x \le 100; -100 \le y \le 100$. The incident acoustic wave is specified at $x = -100$. The pressure and density of the incident acoustic waves, $\hat{p}_i$ and $\hat{\rho}_i$, are illustrated in Figure 5.5(b) and 5.6(b), respectively.

In this case, the radius of the distributed thermal disturbance is about 0.3 times the incident acoustic wavelength and can be regarded as the long wavelength limit, i.e. the Born limit. According to Morse and Uno Ingard (1968), this is often the case for sound scattering. Therefore, it is of interest to study this long wavelength limit for practical reasons.

Unlike Case (1) for short wavelength, the scattered waves spread out in all directions as "reflected waves". Since the interfering wave is negligible in this long wavelength limit, no sharp-edged shadow is expected in the scattered field. The corresponding contour of the resulting fluctuation of pressure $\hat{p}$, density $\hat{\rho}$ and temperature $\hat{T}$ are shown in Figures 5.7(b), 5.8(b) and 5.9(b) respectively. It can be seen from the figures that the fluctuations are quite uniform.

The scattered pressure $\hat{p}_s$ and the corresponding directivity pattern are shown in Figure 5.10(b) and 5.11(b). The scattered pressure spreads more or less uniformly in all directions, with the peak amplitude at the immediate wake region of the distributed thermal disturbance. As shown in the 2-D contour plots, there is a phase change at $\theta = \pm\frac{\pi}{2}$. Maximum amplitudes are reported at around $\theta = 0$ and decreases to its minimum at $\theta = \pm\frac{\pi}{2}$ and increases again to its secondary peak at $\theta = \pi$. This indicates that the

"reflected" portion of the scattered wave is significant for this long wavelength limit or Born limit. Along the axis of symmetry of the distributed thermal disturbance in the forward scattering direction, there is a noticeable drop in $\hat{p}_s$. This "dip" in $\hat{p}_s$ is detected throughout the *x*-axis downstream of the distributed thermal disturbance. A directivity plot for $r/\lambda^* = 3$ for $\hat{p}_s$ is shown on figure 5.11(c). It shows that as r/λ^* decreases, more "dips" are detected around the *x*-axis downstream of the distributed thermal disturbance.

The 2-D contours and the directivity pattern of the scattered density $\hat{\rho}_s$ are illustrated in Figures 5.14(b) and 5.15(b), respectively. Again, similar fluctuation pattern is expected for $\hat{\rho}_s$ and $\hat{p}_s$, in accordance with the isentropic relations $\hat{p} = a_\infty^2 \hat{\rho}$ and $\hat{p}_i = a_\infty^2 \hat{\rho}_i$.

The scattered temperature $\hat{T}_s$ is obtained by the equation of state. The corresponding 2-D contours and the directivity plot are shown in Figures 5.16(b) and 5.17(b), respectively. Again, the scattered waves spread out uniformly with maximum amplitude around $\theta = 0$ with a drop at $\theta = 0$. There is a noticeable phase change at $\theta = \pm\frac{\pi}{2}$. The scattered amplitude decreases to its minimum at $\theta = \pm\frac{\pi}{2}$ and increases again to its secondary peak at $\theta = \pi$. Similar to the explanation for the scattered pressure and density, there is significant "reflection" of scattered waves for this long wavelength limiting case. As for the scattered pressure, $\hat{p}_s$, more "dips" are detected around $\theta = 0$ as r/λ^* decreases, as shown in Figure 5.17(c).

5.4 Summary

In this chapter, the theoretical solution for sound scattering by a distributed thermal disturbance with zero heat loss/gain is obtained by patching method. The distributed thermal disturbance was so structured that a steady state solution can be obtained for this acoustic scattering problem. Two cases, namely the short wavelength or WKB limit, and the long wavelength or Born limit, are investigated. Different scattering pattern were obtained for both limits, due to the difference in scattered waves distributed in all directions resulting from the interaction between the incident sound waves and the distributed thermal disturbance.

For the former case, a shadow with sharp edge is observed behind the distributed thermal disturbance along its x-axis of symmetry in the forward scattering direction, while it is absent in the latter one. The difference was shown clearly on the directivity plots, in which reflection is insignificant for the short wavelength limit case while important for the long wavelength limit one.

As seen in 5.2.2.4, patching was carried out by choosing r_2, where r_2 was taken to be greater than, but close to 3.0. In this chapter, r_2 was chosen to be 5 for patching. To ensure that the theoretical solution is not sensitive to the selected value of r_2, patching was accomplished by using r_2 equals to 7 and 10, and no significant difference could be detected for the results obtained.

In the next chapter, the same cases would be studied numerically by solving the modeled BE. The heat resolving ability of the modeled BE could then be validated.

Acknowledgement

A grateful acknowledgement is made to Professor TAM, K W Christopter of the Department of Mathematics, Florida State University, for his guidance and advice on the theoretical solution of the thermal acoustic scattering problem.

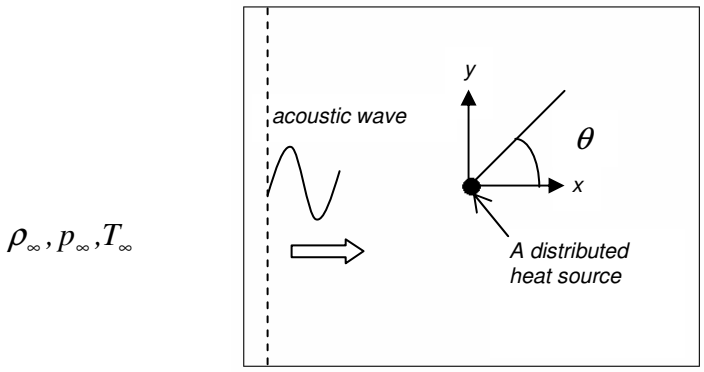

Figure 5.1 Sketch of the acoustic scattering problem

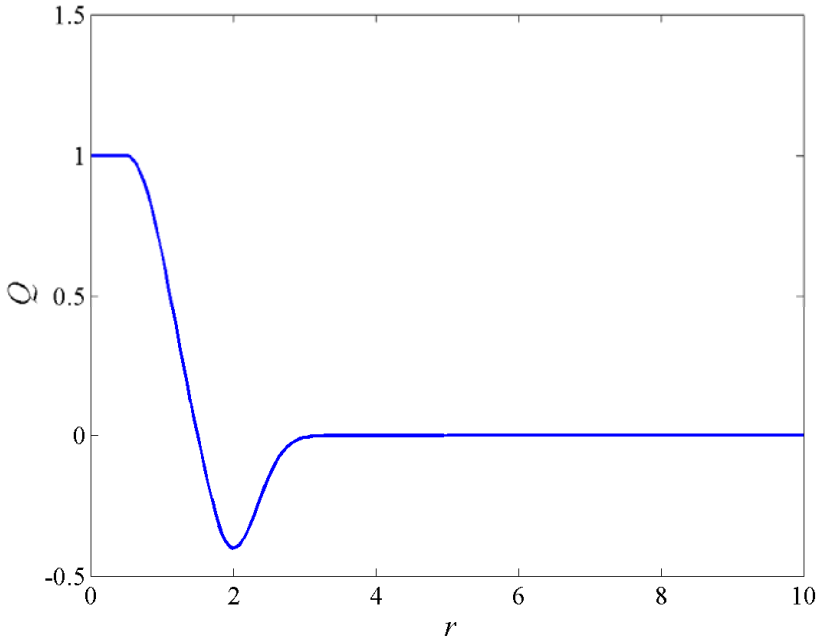

Figure 5.2 Thermal disturbance distribution along a radial direction (dimensionless)

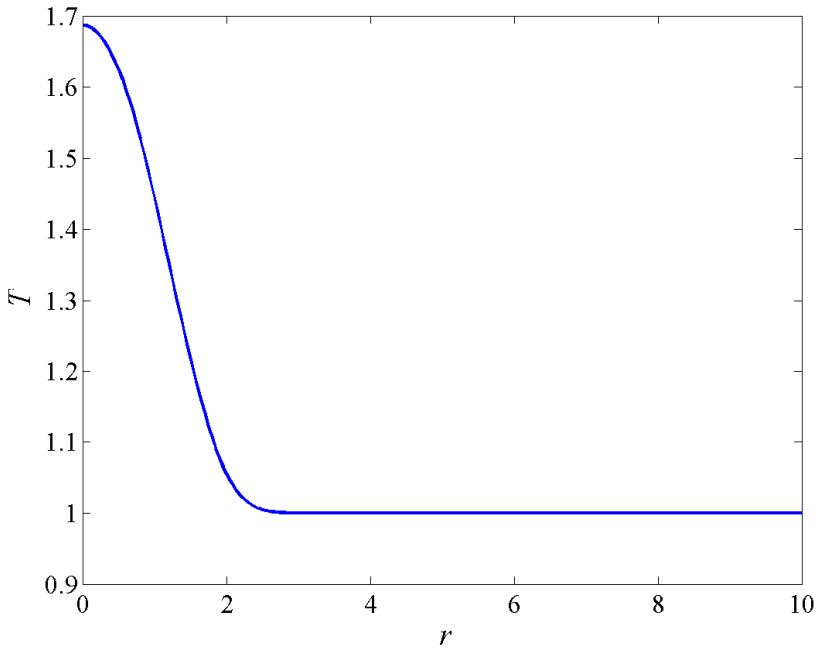

Figure 5.3 Temperature distribution of the distributed thermal disturbance along a radial direction (dimensionless)

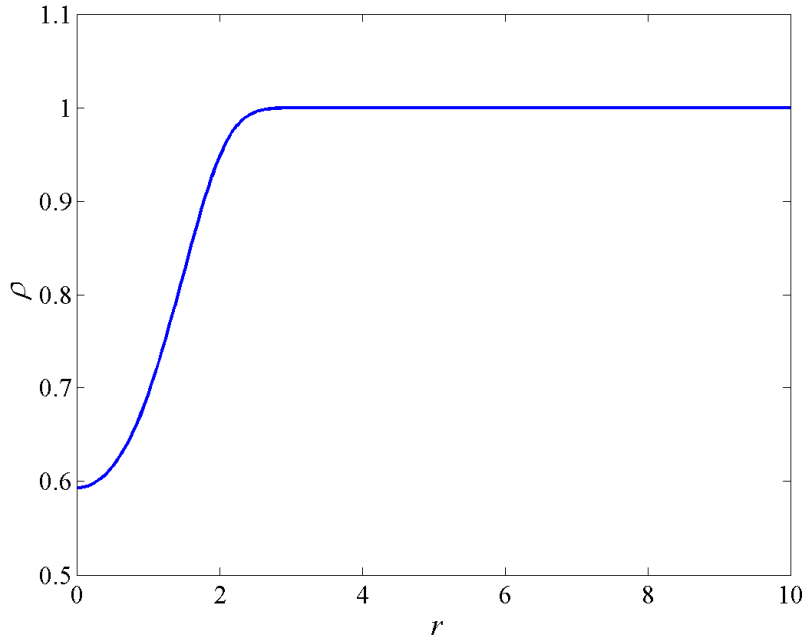

Figure 5.4 Density distribution of the distributed thermal disturbance along a radial direction (dimensionless)

(a)

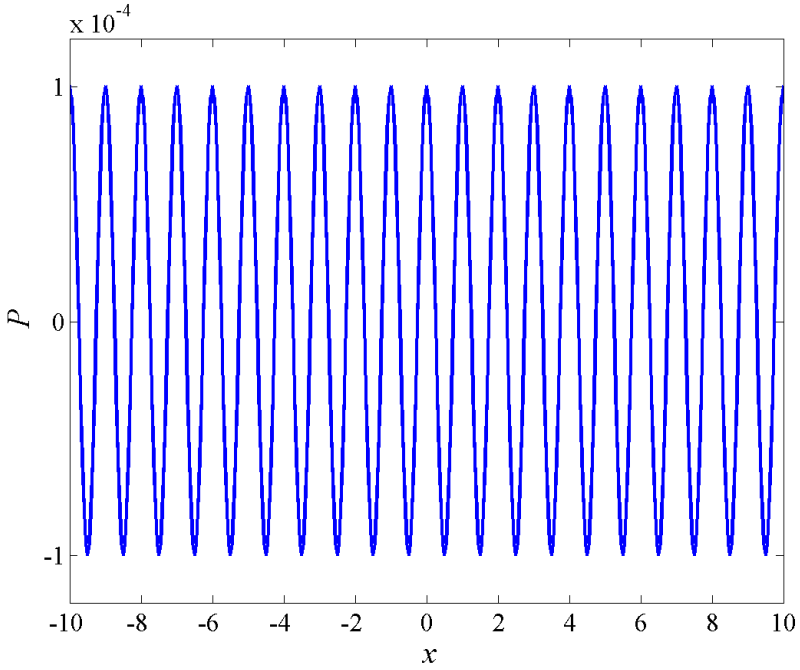

(b)

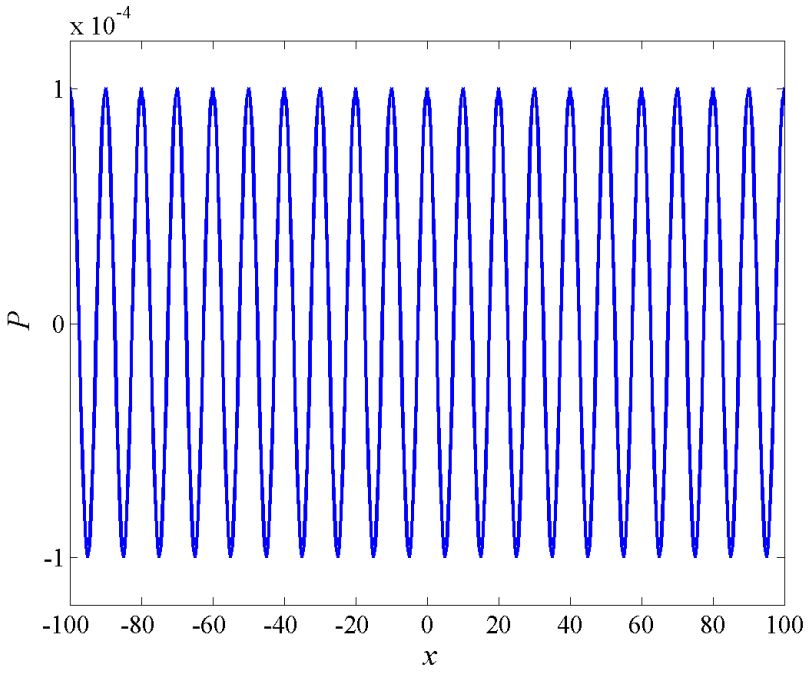

Figure 5.5 Pressure distribution of the incident acoustic wave along x-axis (dimensionless) (a) $\lambda = 1/3$; (b) $\lambda = 10/3$.

(a)

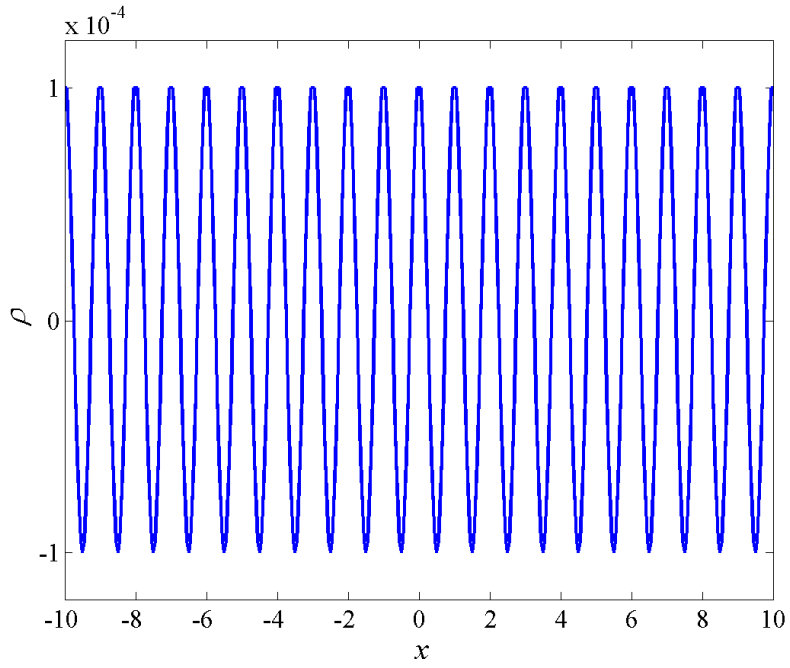

(b)

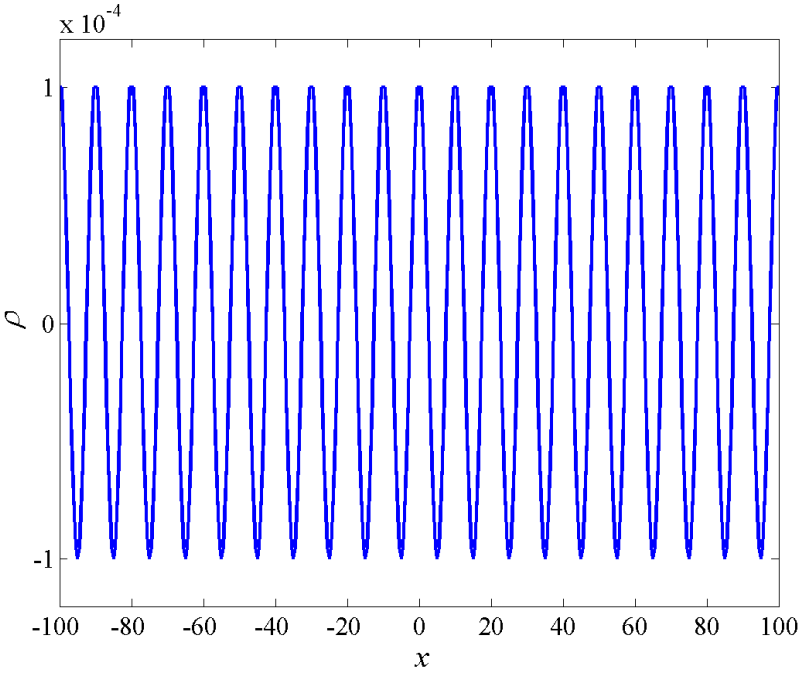

Figure 5.6 Density distribution of the incident acoustic wave along x-axis (dimensionless) (a) $\lambda = 1/3$; (b) $\lambda = 10/3$

(a)

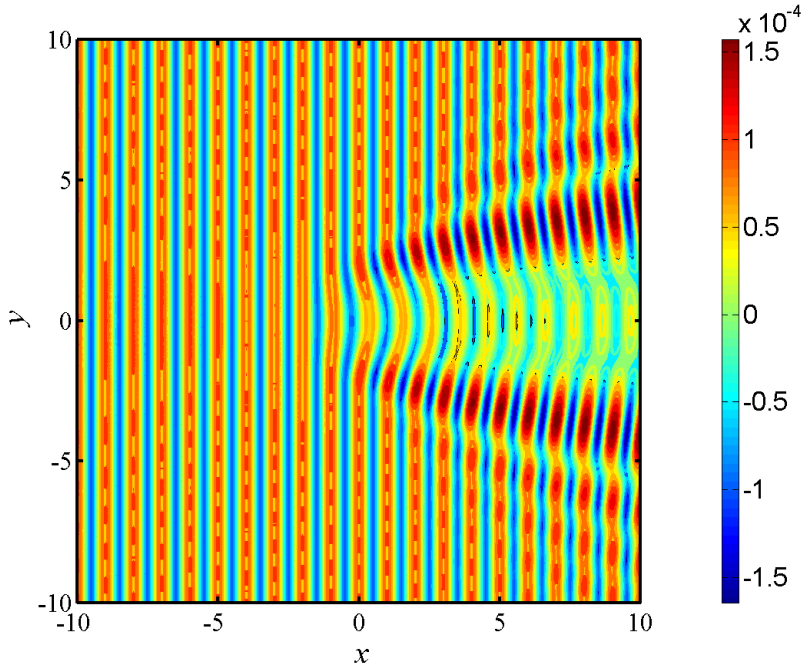

(b)

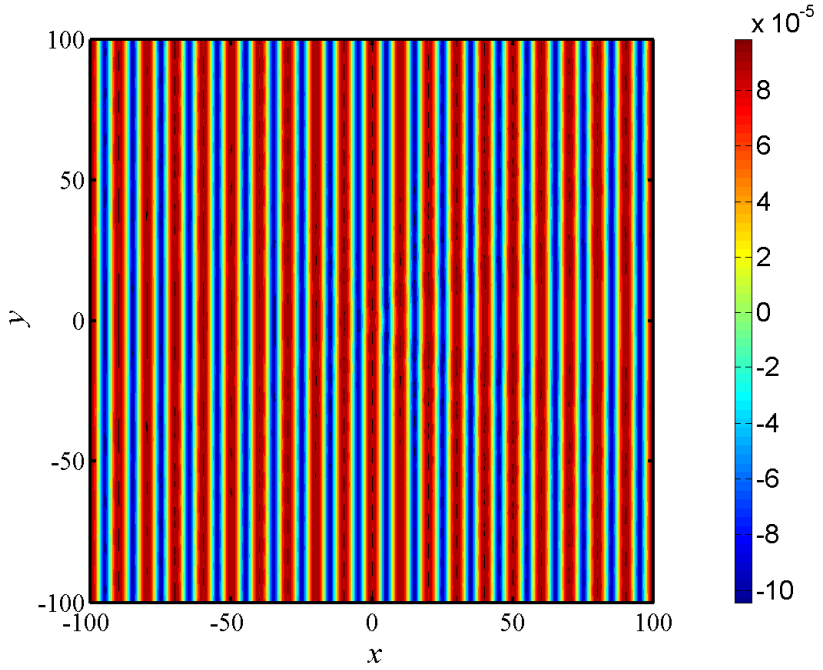

Figure 5.7 Pressure fluctuation of the acoustic scattering problem, $\hat{p}$ (a) $\lambda = 1/3$; (b) $\lambda = 10/3$

(a)

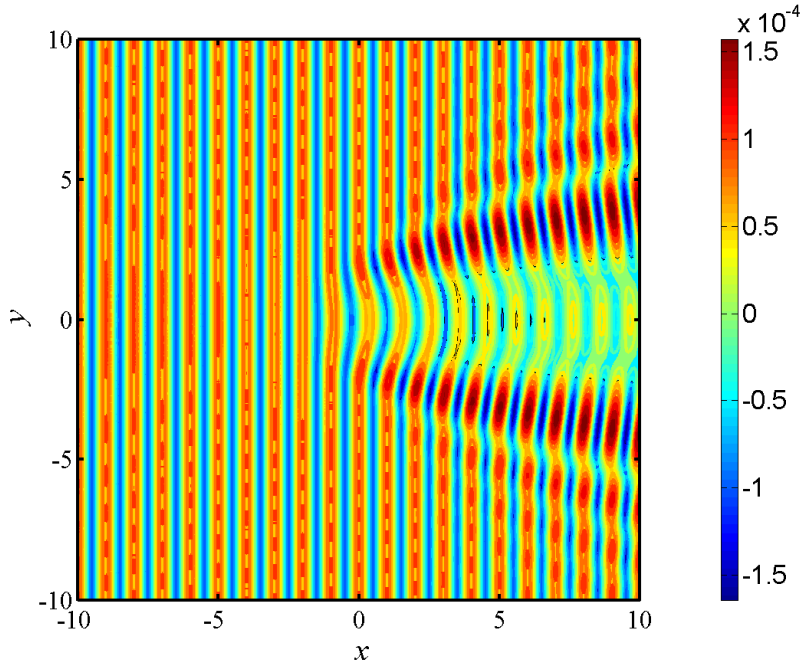

(b)

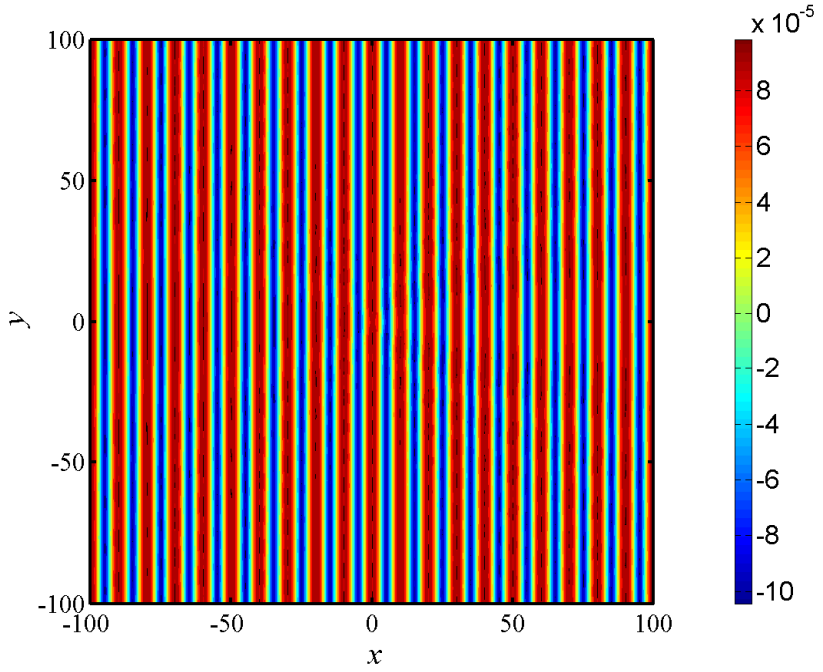

Figure 5.8 Density fluctuation of the acoustic scattering problem, $\hat{\rho}$ (a) $\lambda = 1/3$; (b) $\lambda = 10/3$

(a)

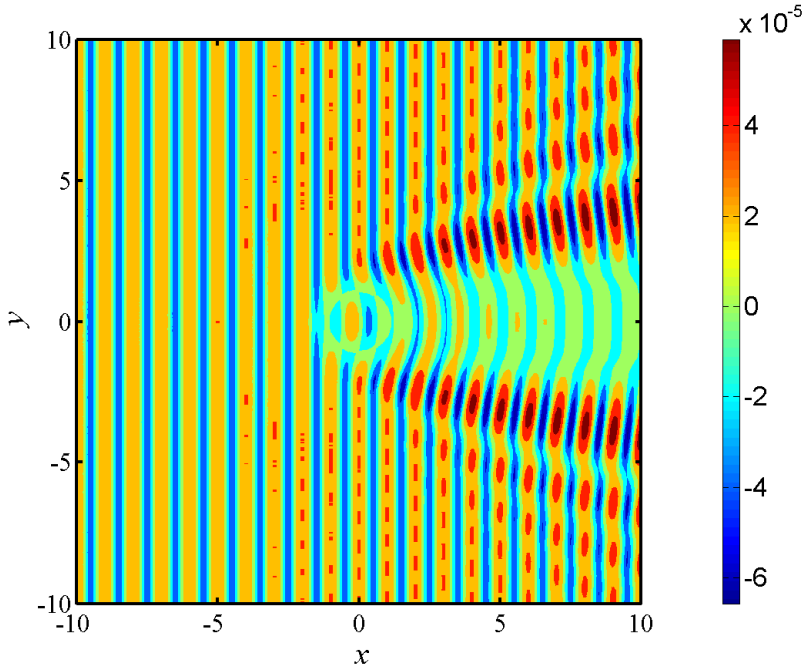

(b)

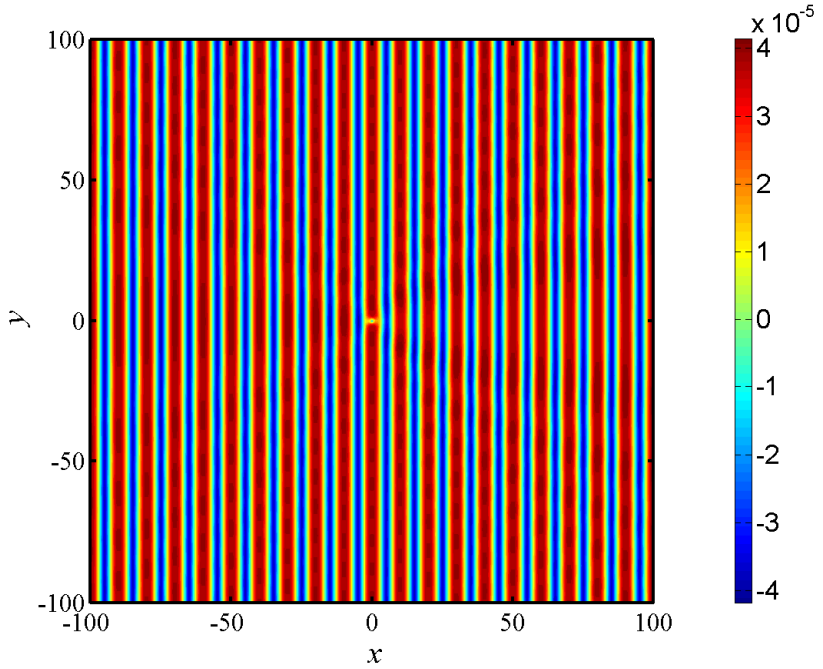

Figure 5.9 Temperature fluctuation of the acoustic scattering problem, $\hat{T}$
(a) $\lambda = 1/3$; (b) $\lambda = 10/3$

(a)

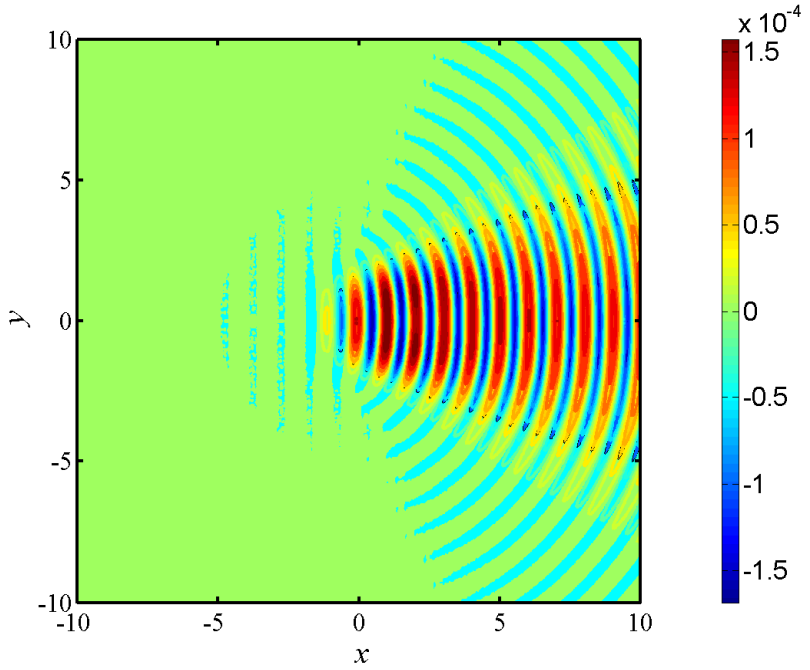

(b)

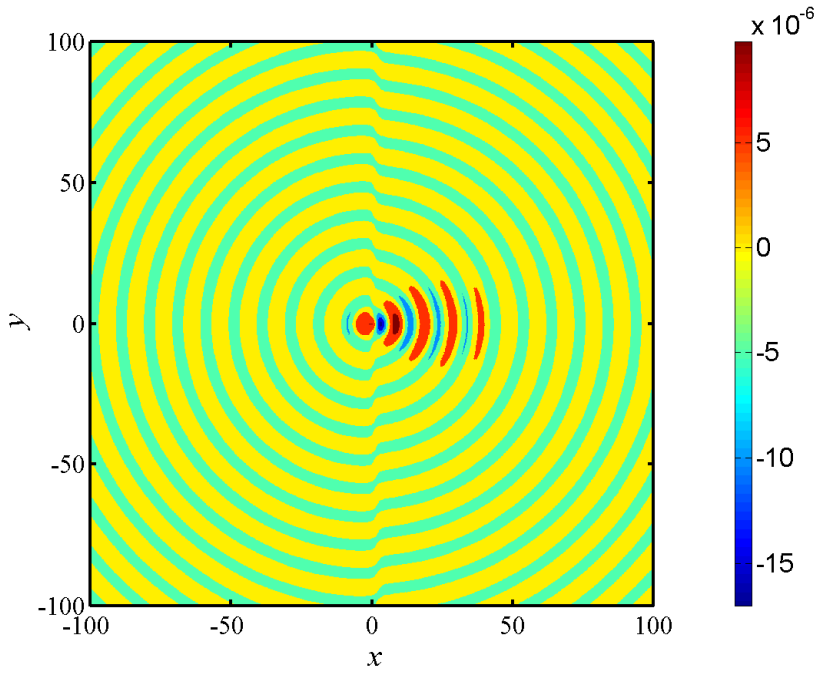

Figure 5.10 Scattered pressure distribution, $\hat{p}_s$ (2D contour) (a) $\lambda = 1/3$; (b) $\lambda = 10/3$

(a)

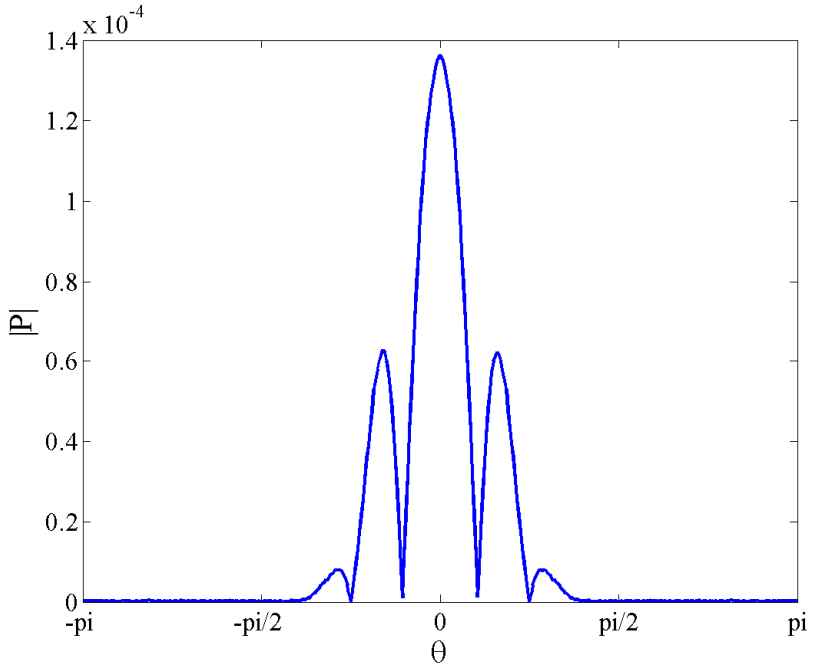

(b)

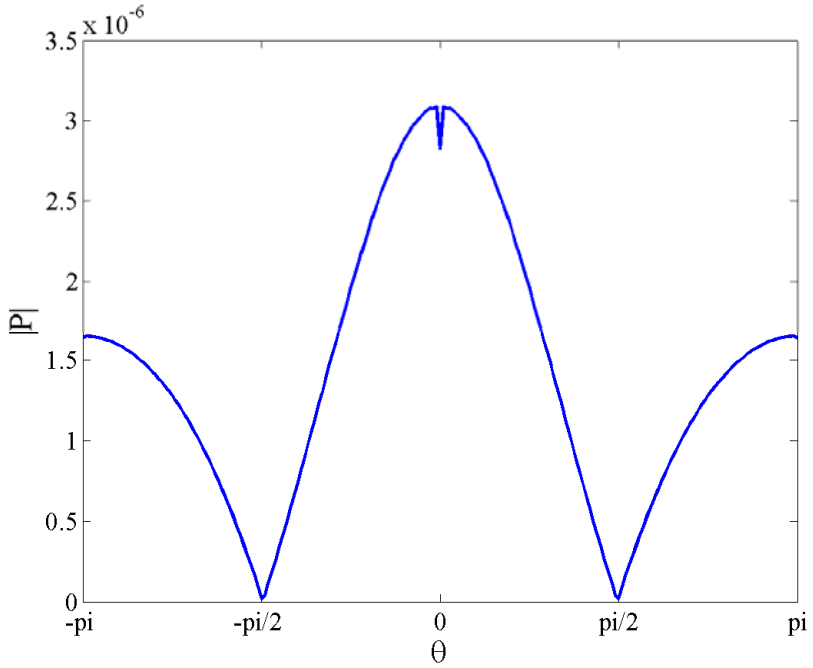

Figure 5.11 Scattered pressure level of the acoustic scattering problem, $\hat{p}_s$ at $r/\lambda^* = 7$ (a) $\lambda = 1/3$; (b) $\lambda = 10/3$

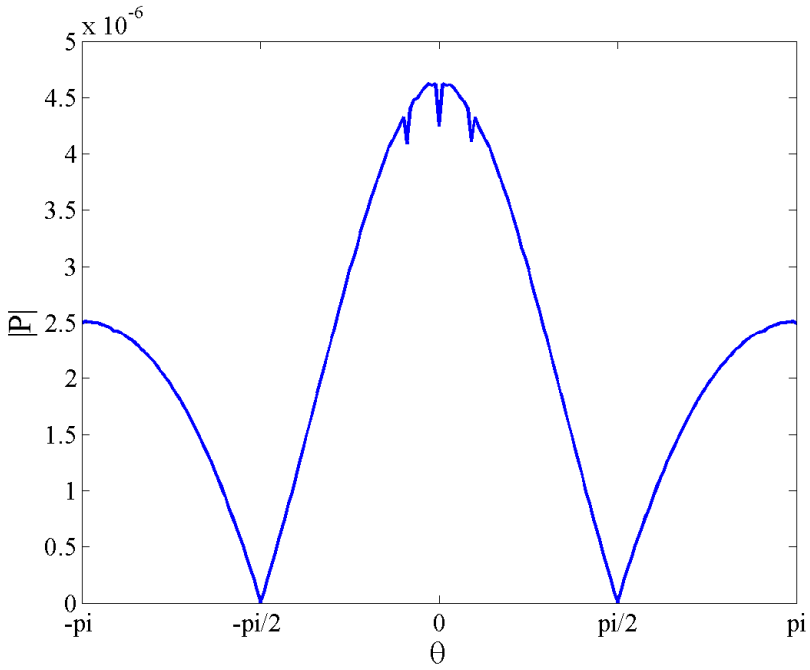

Figure 5.11(c) Scattered pressure level of the acoustic scattering problem, $\hat{p}_s$ at $r/\lambda^* = 3$ for $\lambda = 10/3$

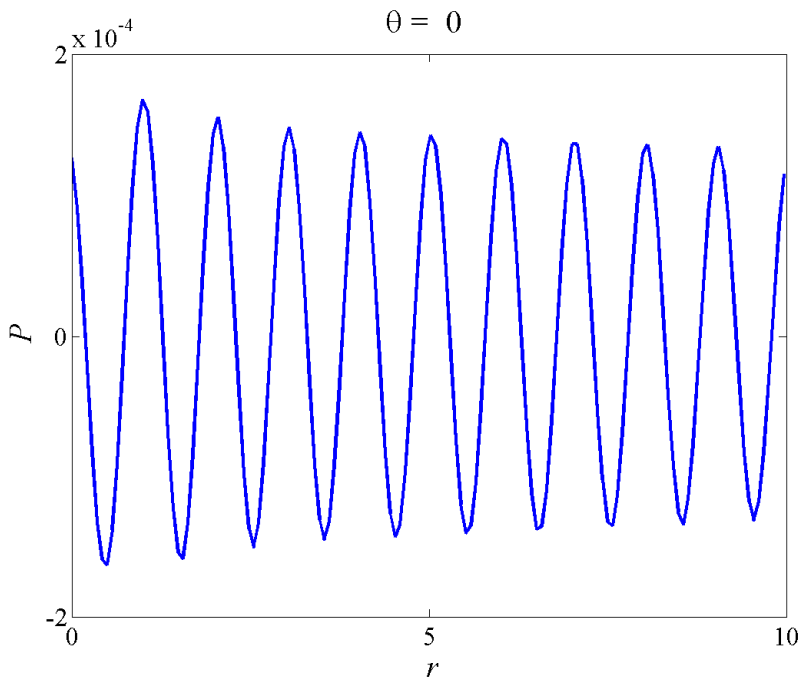

Figure 5.12(a) Scattered pressure $\hat{p}_s$ at $\theta = 0$ for $\lambda = 1/3$

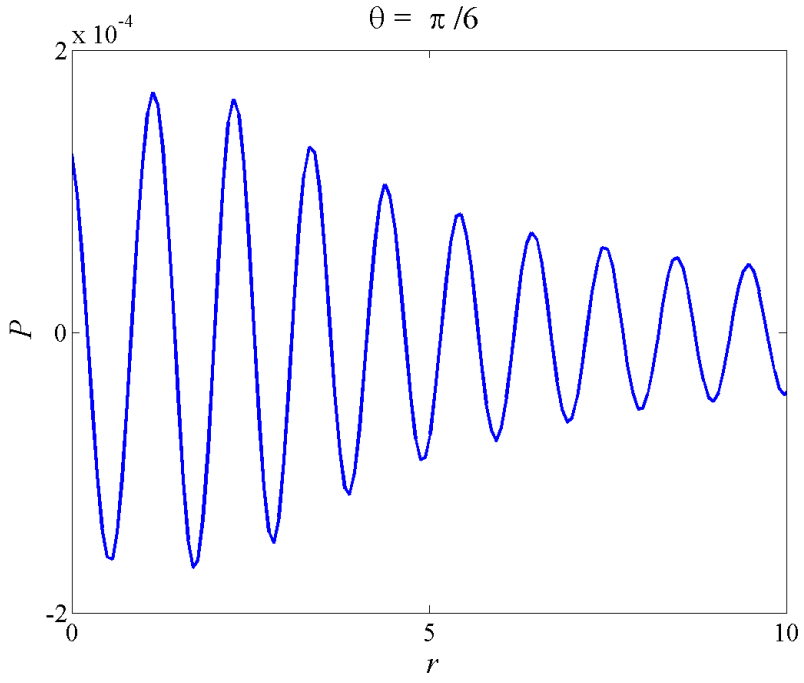

Figure 5.12(b) Scattered pressure $\hat{p}_s$ at $\theta = \pi/6$ for $\lambda = 1/3$

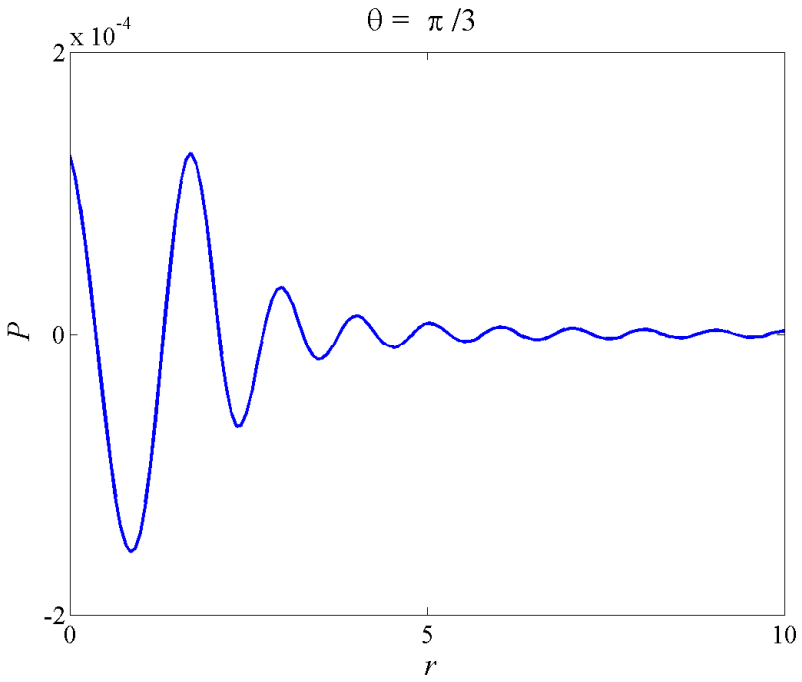

Figure 5.12(c) Scattered pressure $\hat{p}_s$ at $\theta = \pi/3$ for $\lambda = 1/3$

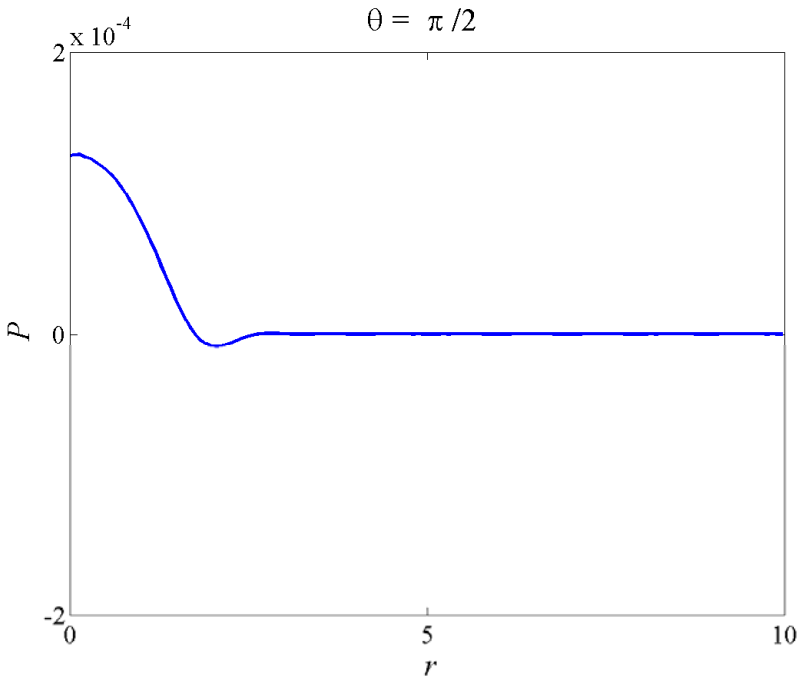

Figure 5.12(d) Scattered pressure $\hat{p}_s$ at $\theta = \pi/2$ for $\lambda = 1/3$

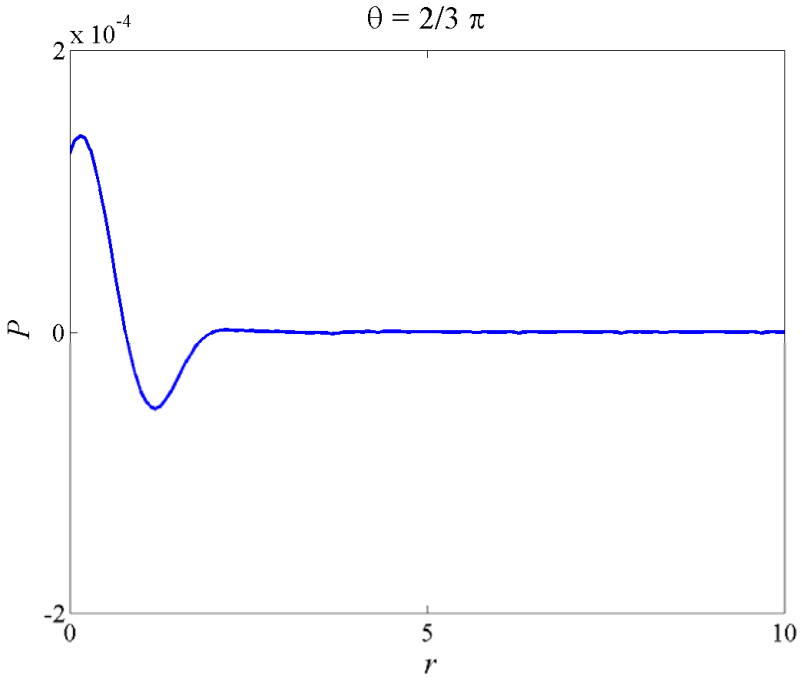

Figure 5.12(e) Scattered pressure $\hat{p}_s$ at $\theta = 2\pi/3$ for $\lambda = 1/3$

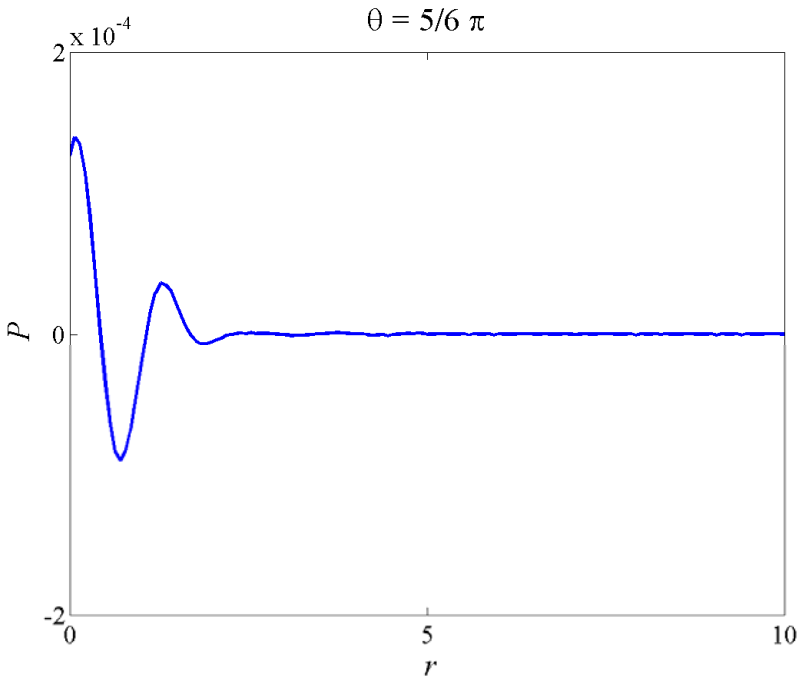

Figure 5.12(f) Scattered pressure $\hat{p}_s$ at $\theta = 5\pi/6$ for $\lambda = 1/3$

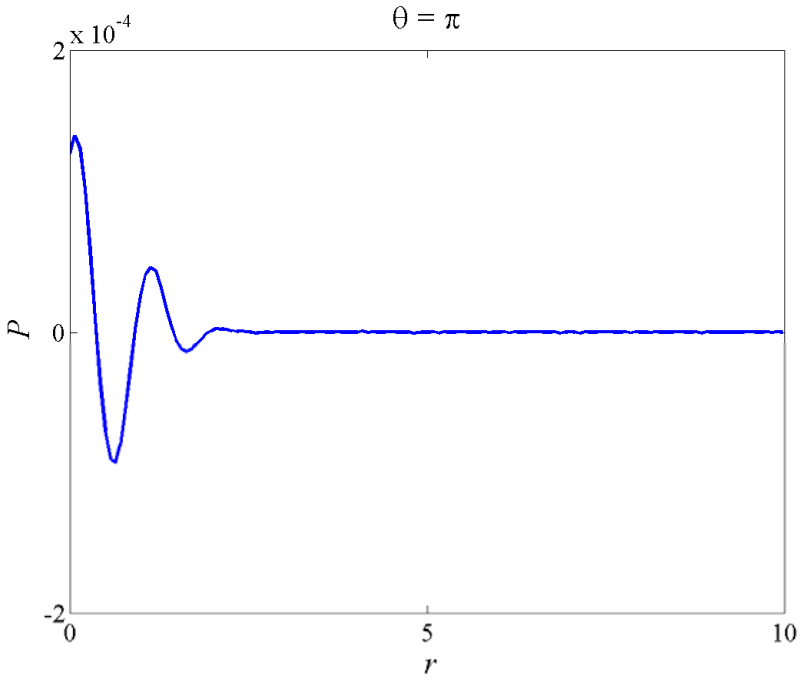

Figure 5.12(g) Scattered pressure $\hat{p}_s$ at $\theta = \pi$ for $\lambda = 1/3$

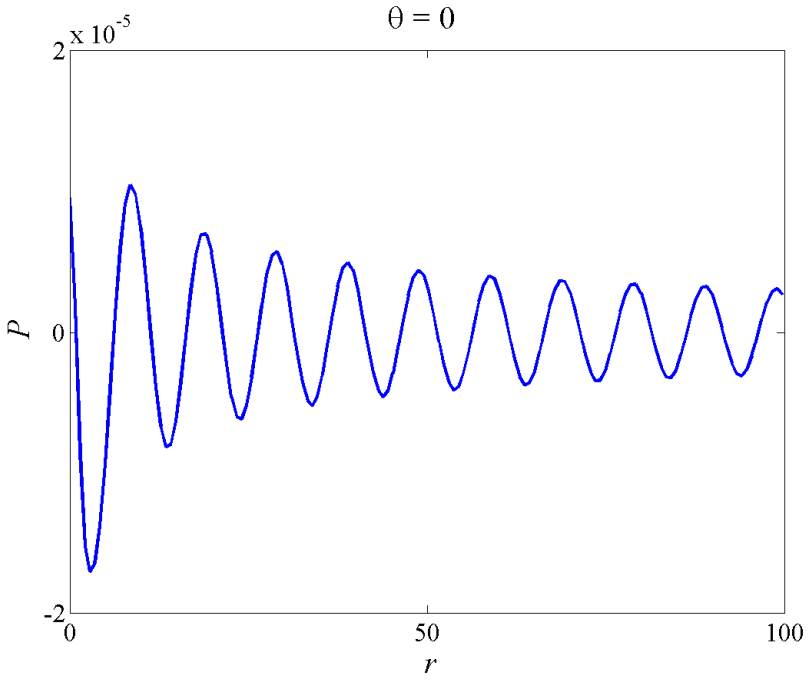

Figure 5.13(a) Scattered pressure $\hat{p}_s$ at $\theta = 0$ for $\lambda = 10/3$

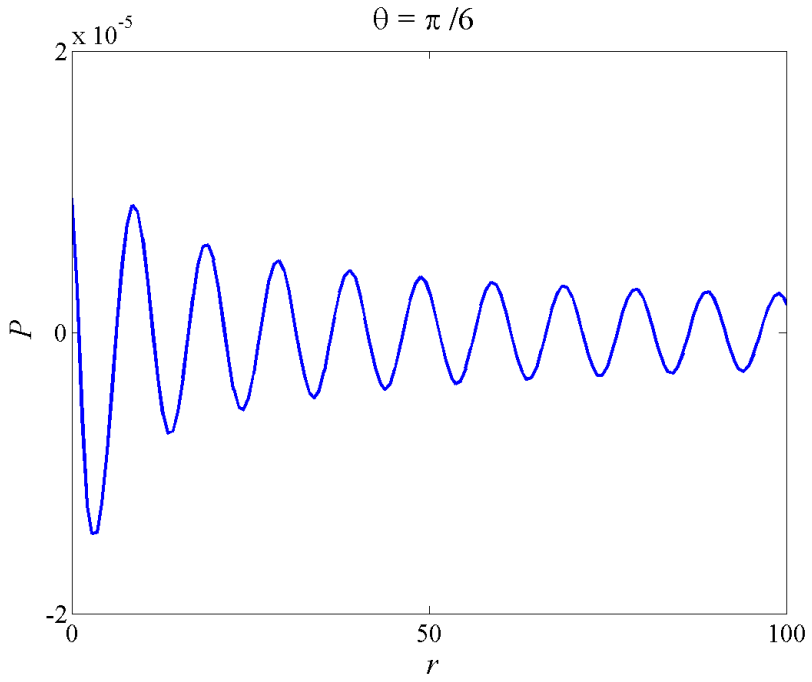

Figure 5.13(b) Scattered pressure $\hat{p}_s$ at $\theta = \pi/6$ for $\lambda = 10/3$

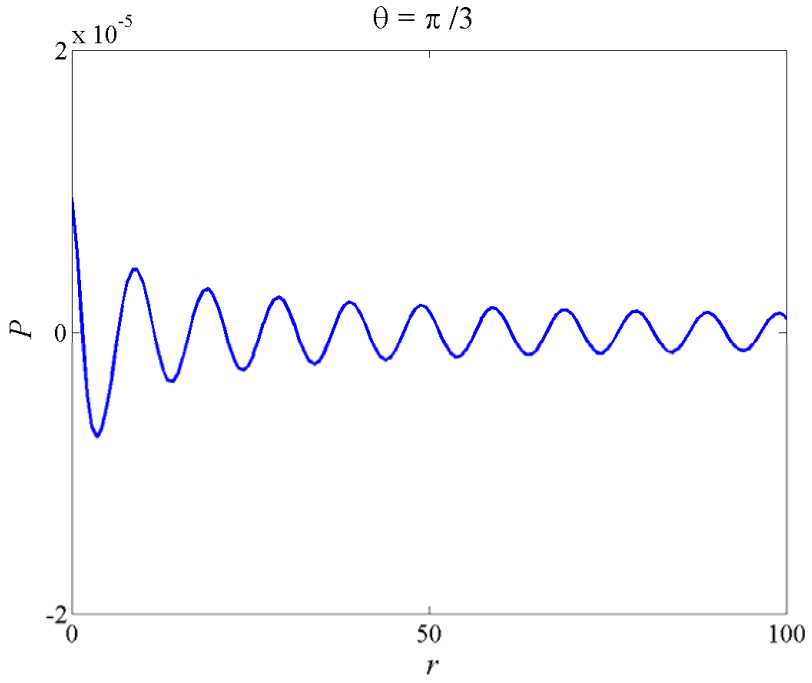

Figure 5.13(c) Scattered pressure $\hat{p}_s$ at $\theta = \pi/3$ for $\lambda = 10/3$

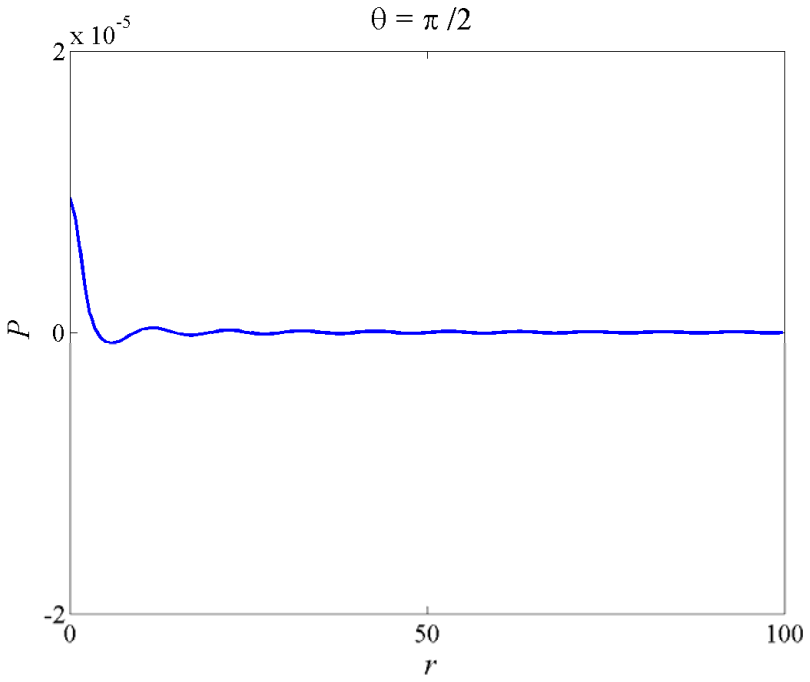

Figure 5.13(d) Scattered pressure $\hat{p}_s$ at $\theta = \pi/2$ for $\lambda = 10/3$

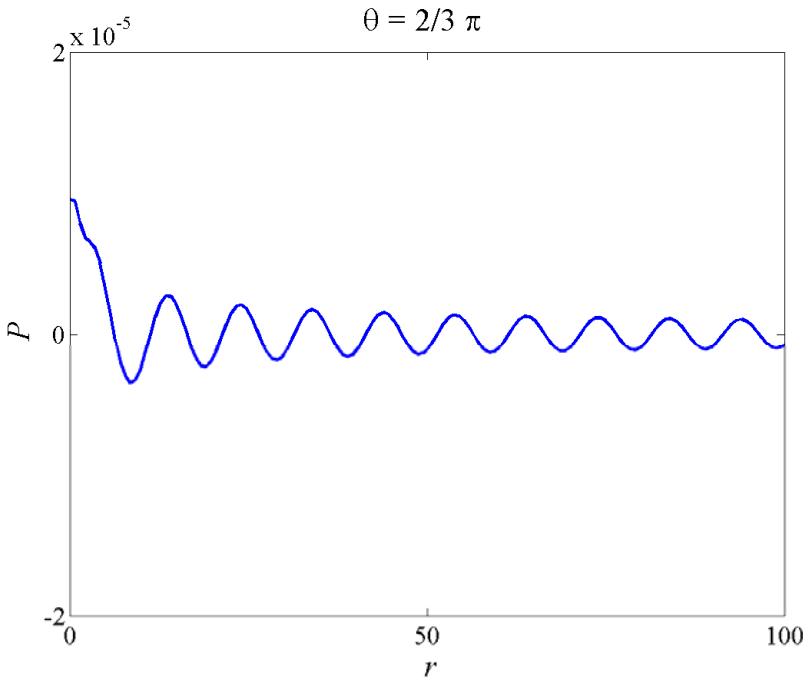

Figure 5.13(e) Scattered pressure $\hat{p}_s$ at $\theta = 2\pi/3$ for $\lambda = 10/3$

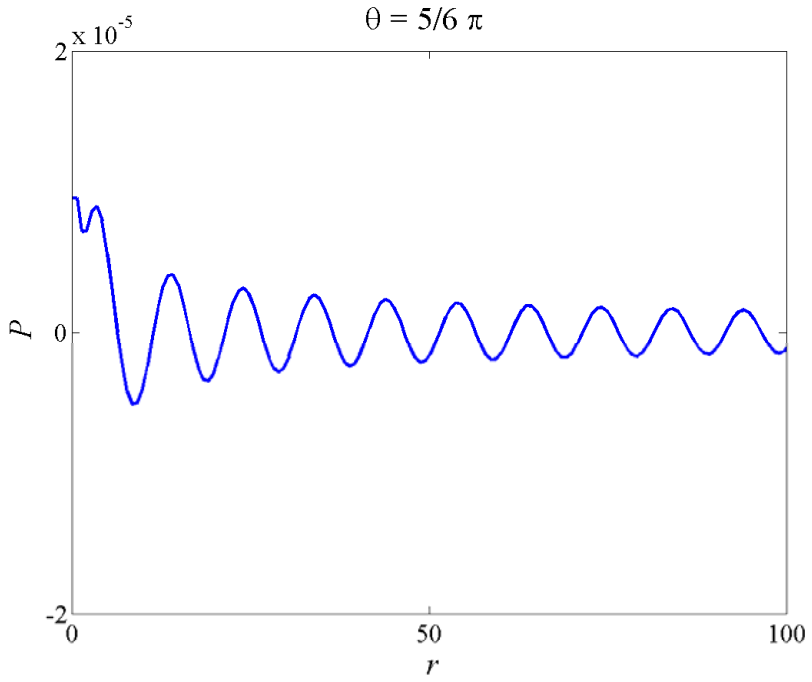

Figure 5.13(f) Scattered pressure $\hat{p}_s$ at $\theta = 5\pi/6$ for $\lambda = 10/3$

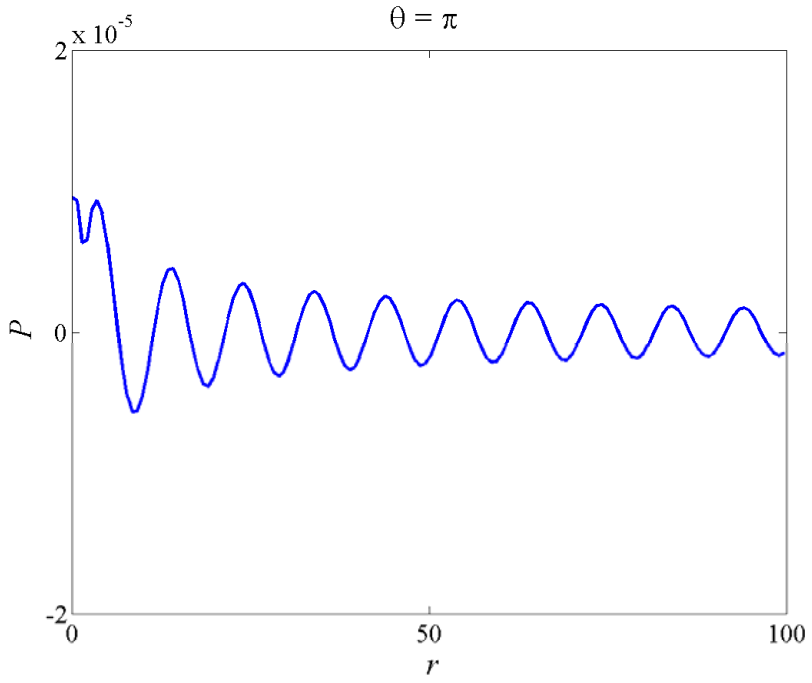

Figure 5.13(g) Scattered pressure $\hat{p}_s$ at $\theta = \pi$ for $\lambda = 10/3$

(a)

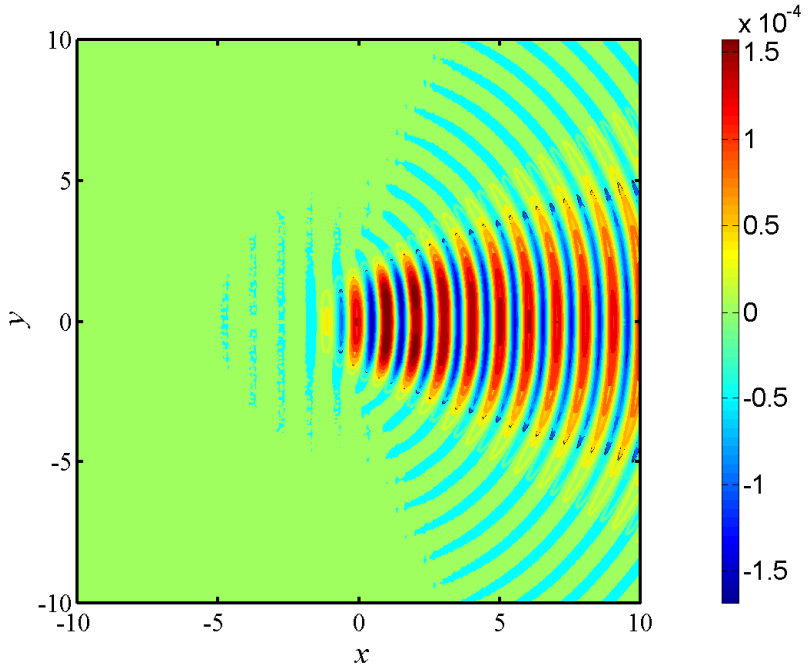

(b)

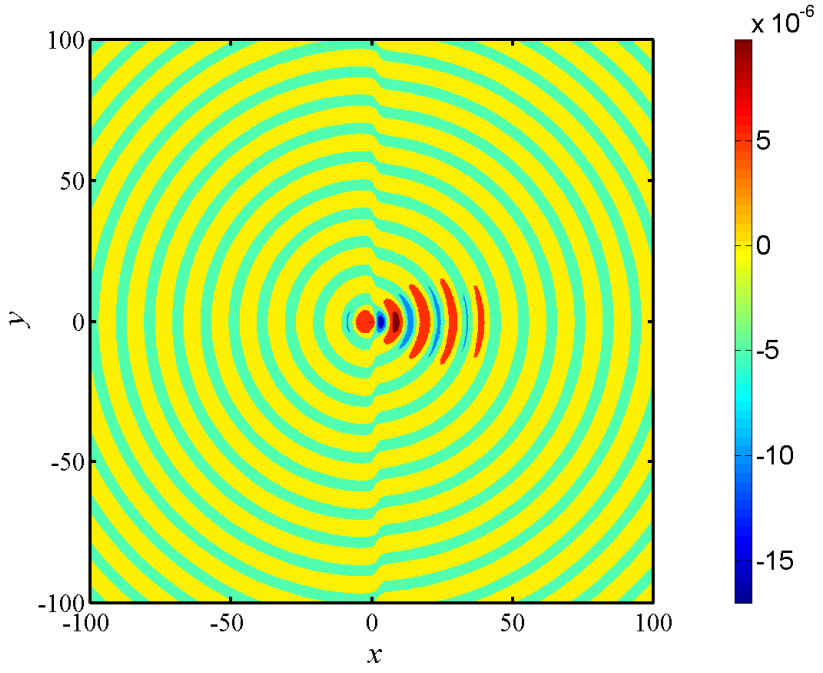

Figure 5.14 Scattered density distribution, $\hat{\rho}_s$ (2D contour) (a) $\lambda = 1/3$; (b) $\lambda = 10/3$

(a)

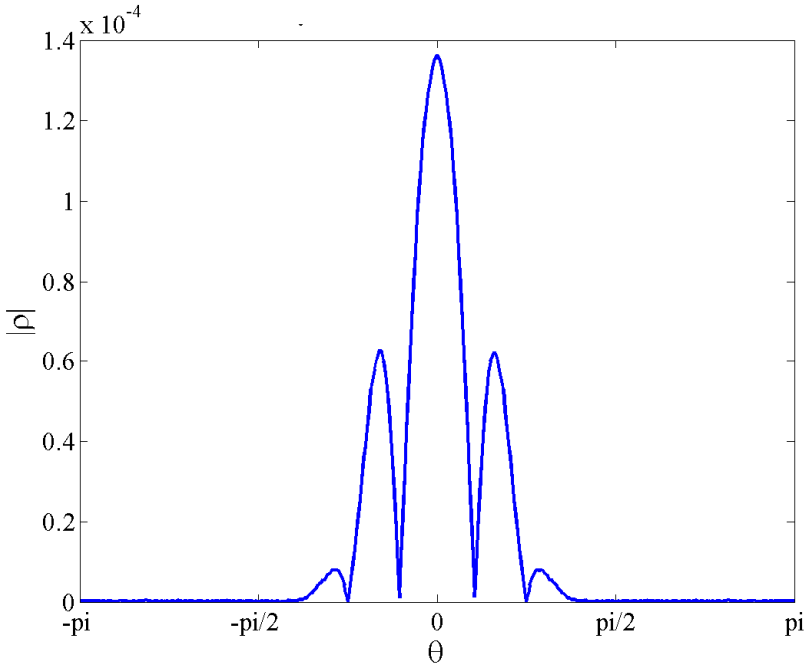

(b)

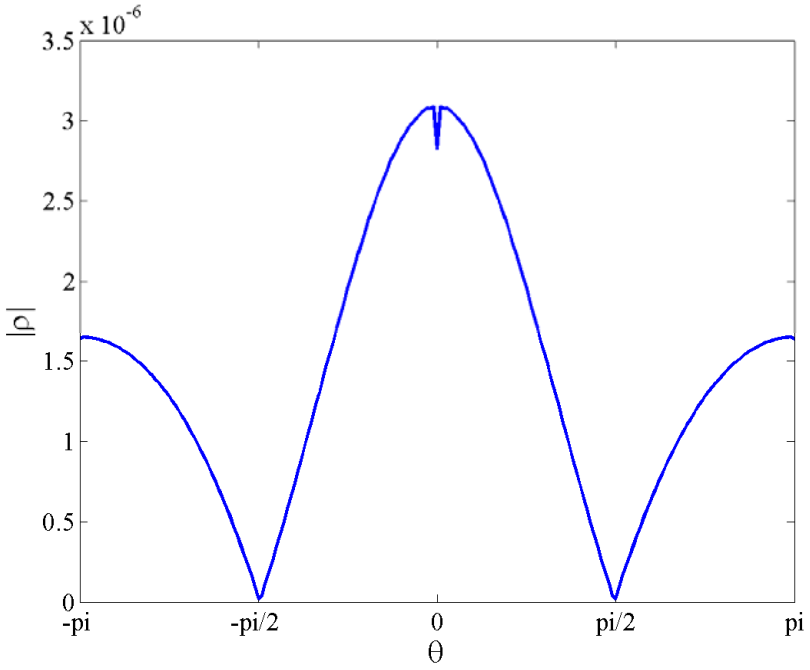

Figure 5.15 Scattered density level of the acoustic scattering problem, $\hat{\rho}_s$ at $r/\lambda^* = 7$ (a) $\lambda = 1/3$; (b) $\lambda = 10/3$

(a)

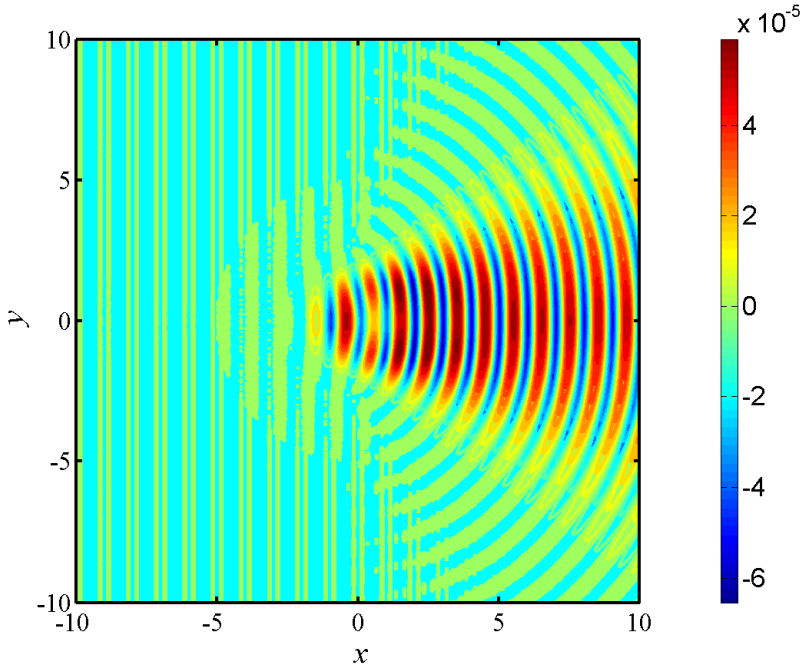

(b)

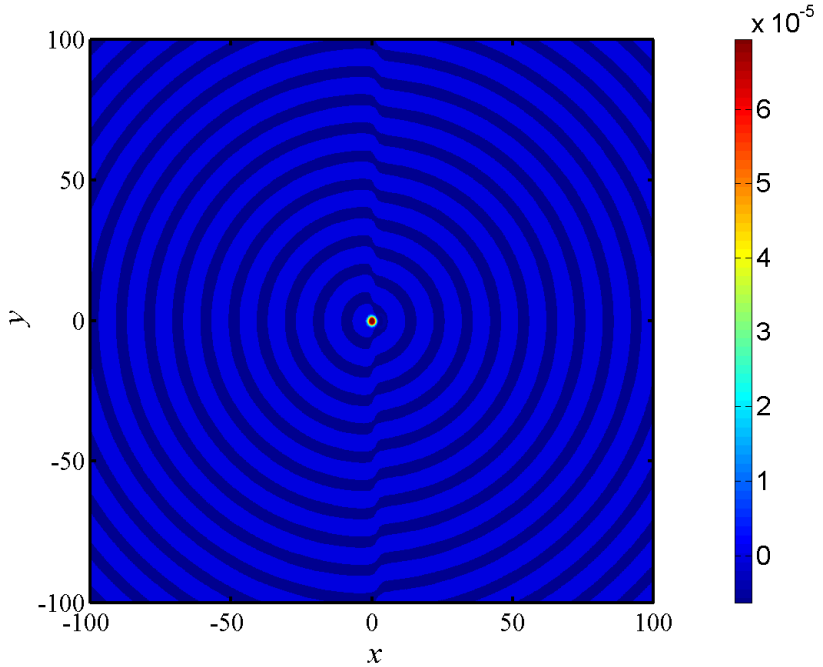

Figure 5.16 Scattered temperature distribution, $\hat{T}_s$ (2D contour) (a) $\lambda = 1/3$; (b) $\lambda = 10/3$

(a)

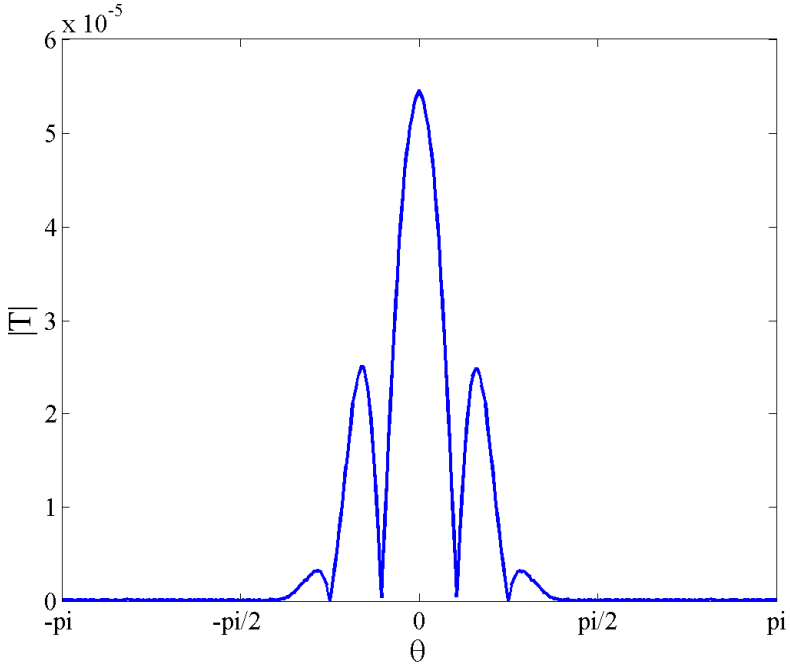

(b)

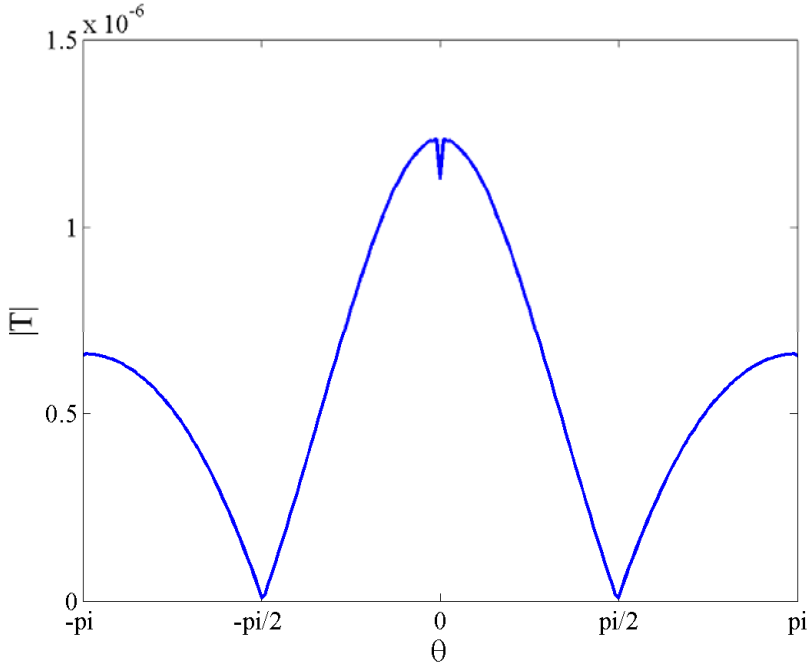

Figure 5.17 Scattered temperature level of the acoustic scattering problem, $\hat{T}_s$ at $r/\lambda^* = 7$ (a) $\lambda = 1/3$; (b) $\lambda = 10/3$

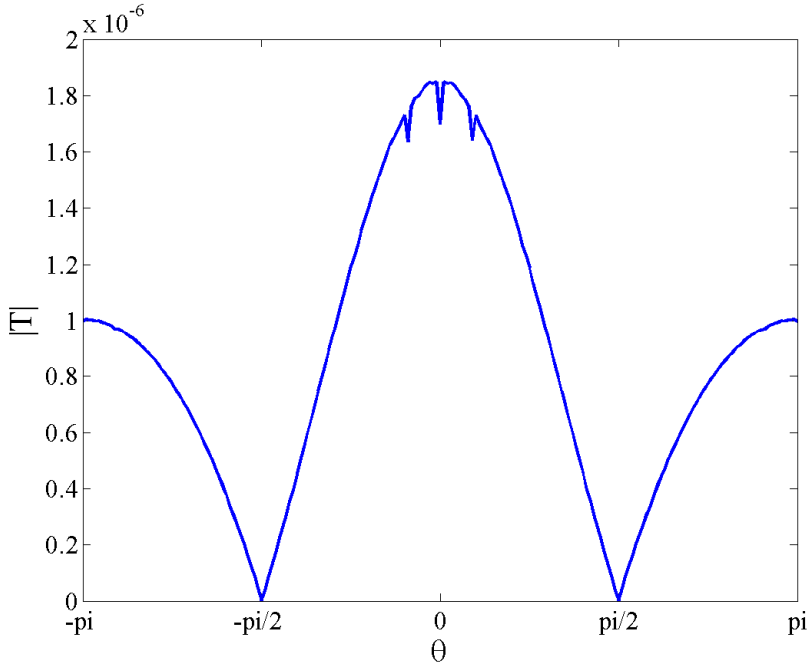

Figure 5.17(c) Scattered temperature level of the acoustic scattering problem, $\hat{T}_s$ at $r/\lambda^* = 3$ for $\lambda = 10/3$

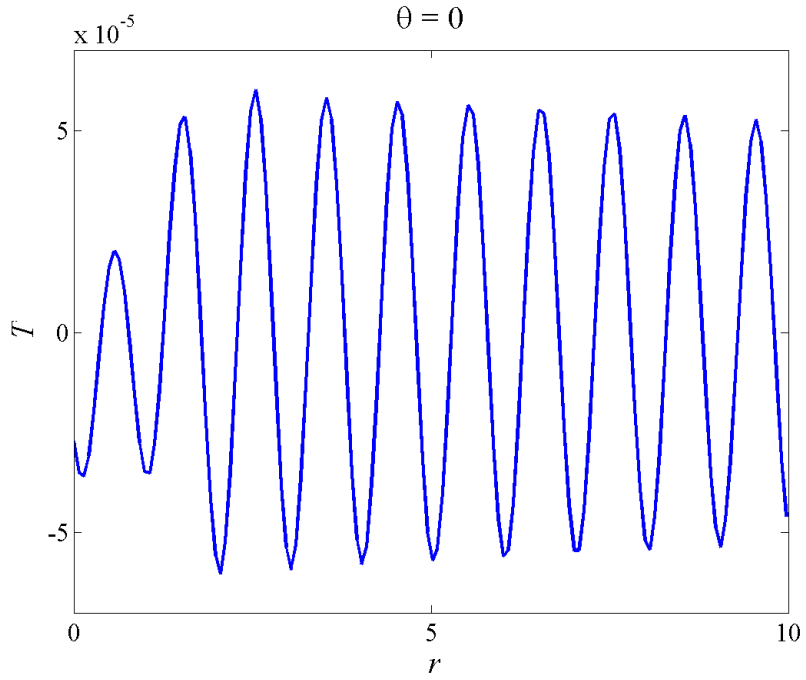

Figure 5.18(a) Scattered temperature $\hat{T}_s$ at $\theta = 0$ for $\lambda = 1/3$

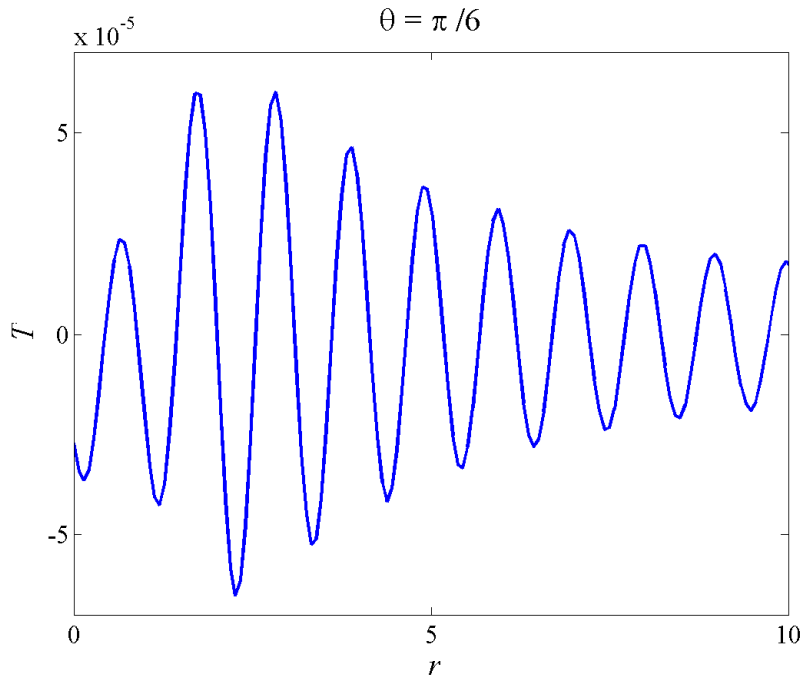

Figure 5.18(b) Scattered temperature $\hat{T}_s$ at $\theta = \pi/6$ for $\lambda = 1/3$

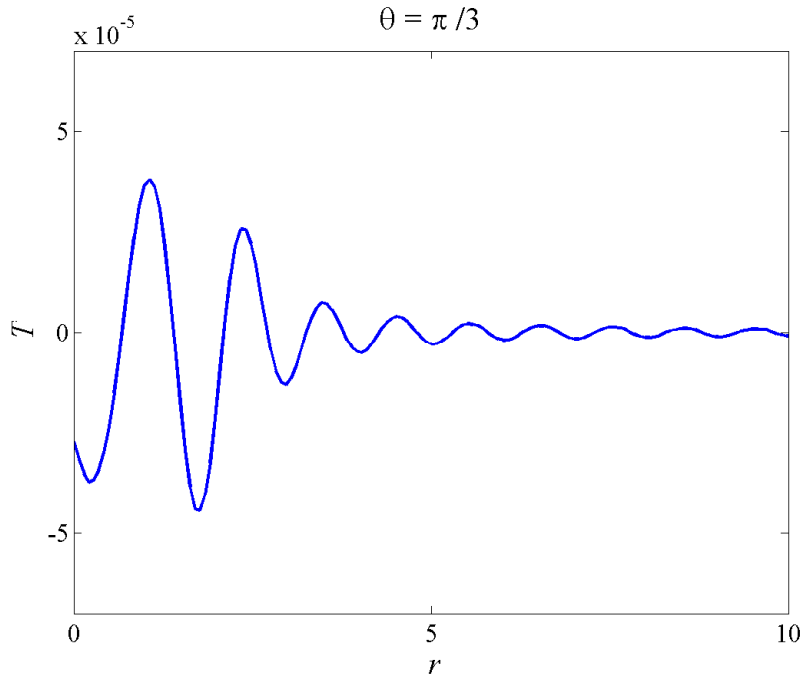

Figure 5.18(c) Scattered temperature $\hat{T}_s$ at $\theta = \pi/3$ for $\lambda = 1/3$

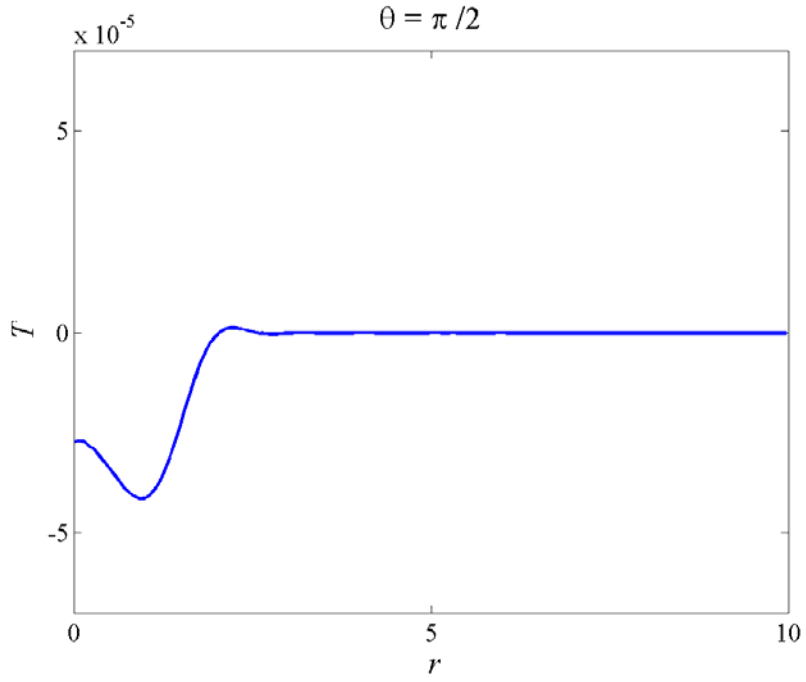

Figure 5.18(d) Scattered temperature $\hat{T}_s$ at $\theta = \pi/2$ for $\lambda = 1/3$

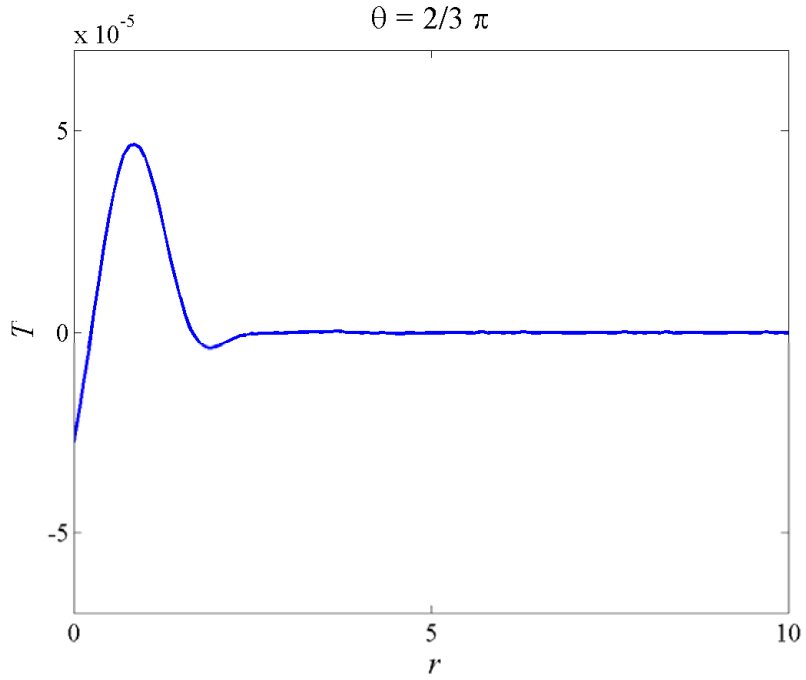

Figure 5.18(e) Scattered temperature $\hat{T}_s$ at $\theta = 2\pi/3$ for $\lambda = 1/3$

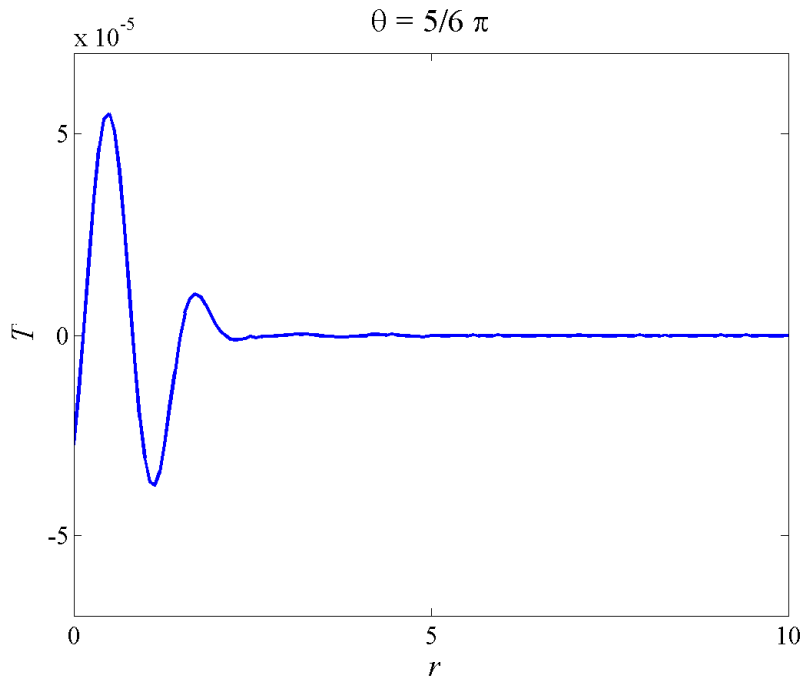

Figure 5.18(f) Scattered temperature $\hat{T}_s$ at $\theta = 5\pi/6$ for $\lambda = 1/3$

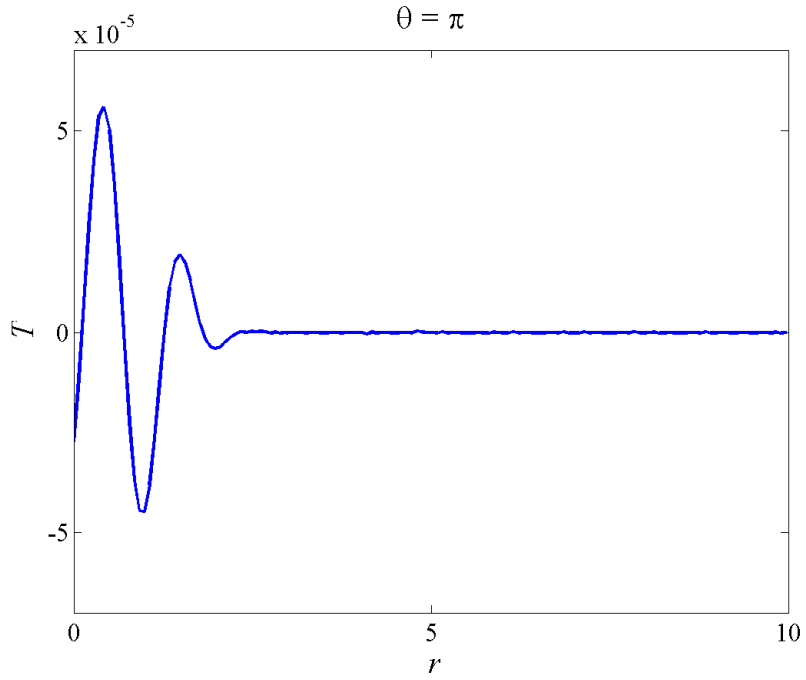

Figure 5.18(g) Scattered temperature $\hat{T}_s$ at $\theta = \pi$ for $\lambda = 1/3$

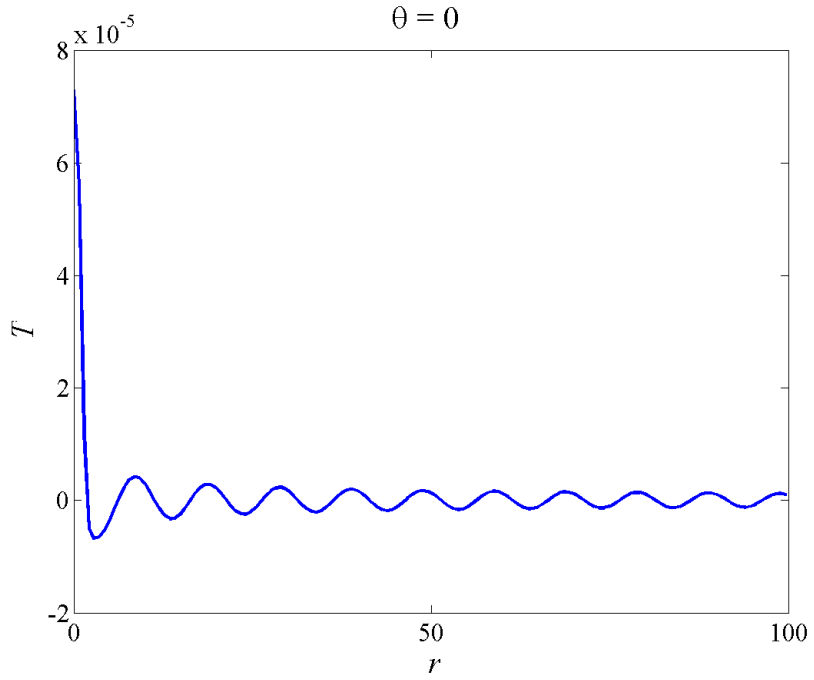

Figure 5.19(a) Scattered temperature $\hat{T}_s$ at $\theta = 0$ for $\lambda = 10/3$

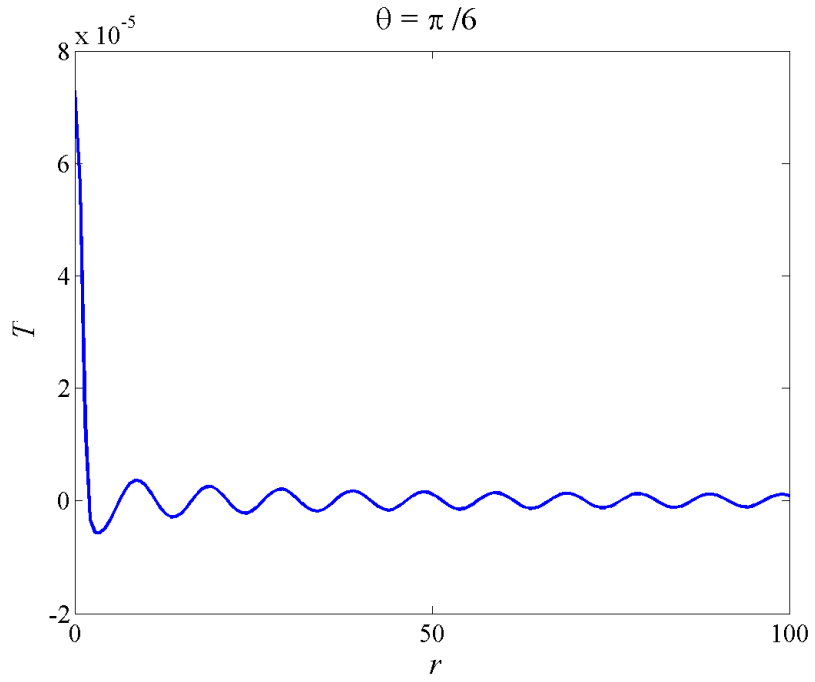

Figure 5.19(b) Scattered temperature $\hat{T}_s$ at $\theta = \pi/6$ for $\lambda = 10/3$

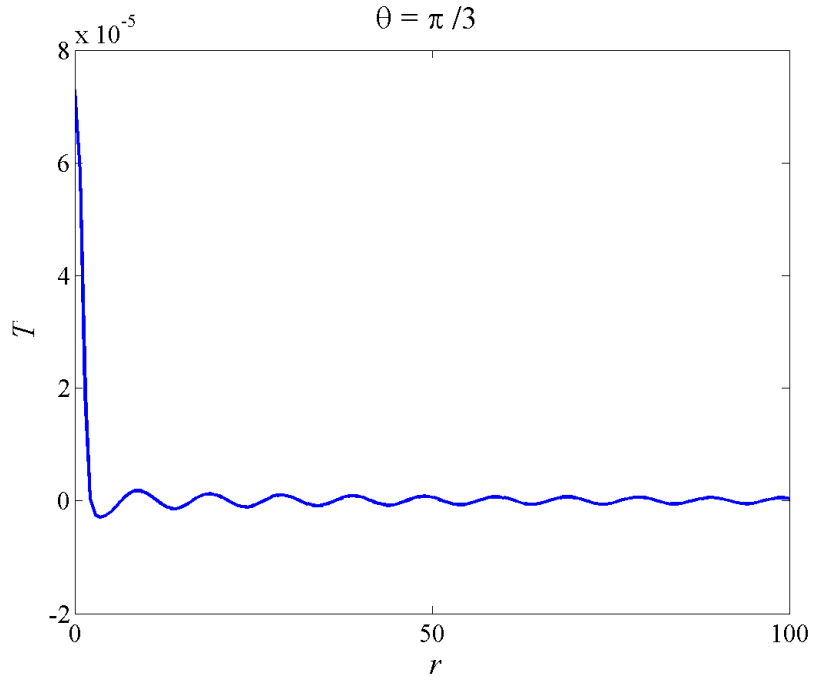

Figure 5.19(c) Scattered temperature $\hat{T}_s$ at $\theta = \pi/3$ for $\lambda = 10/3$

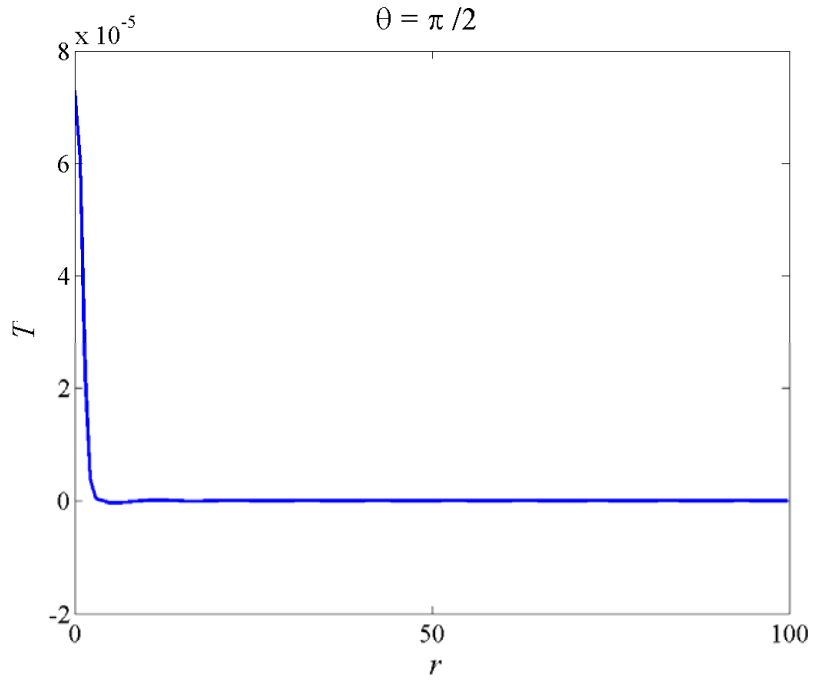

Figure 5.19(d) Scattered temperature $\hat{T}_s$ at $\theta = \pi/2$ for $\lambda = 10/3$

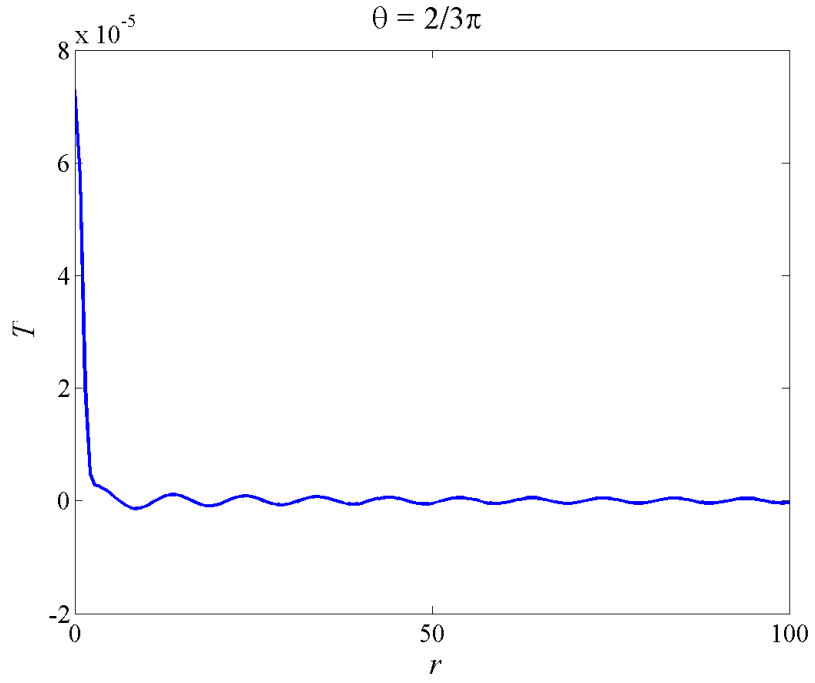

Figure 5.19(e) Scattered temperature $\hat{T}_s$ at $\theta = 2\pi/3$ for $\lambda = 10/3$

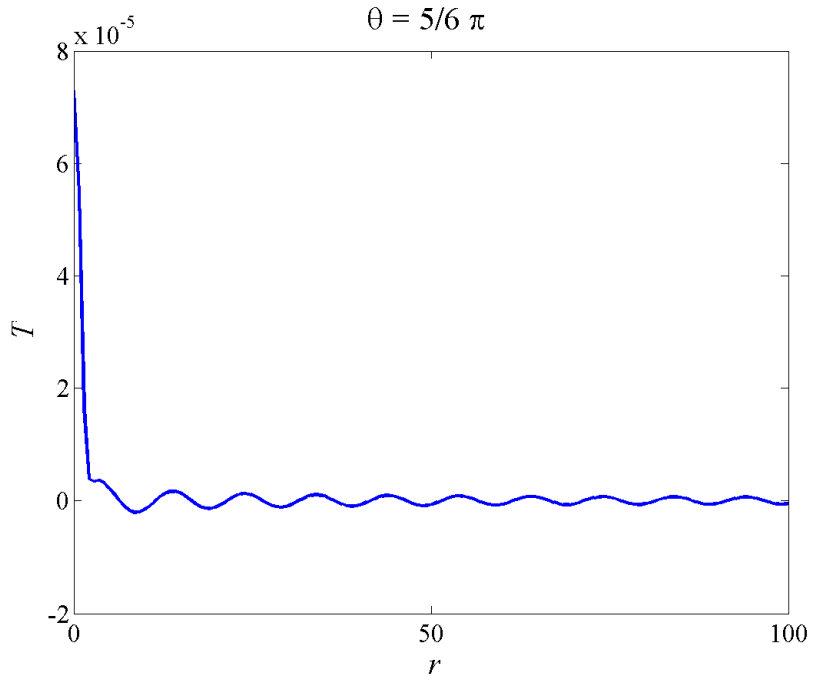

Figure 5.19(f) Scattered temperature $\hat{T}_s$ at $\theta = 5\pi/6$ for $\lambda = 10/3$

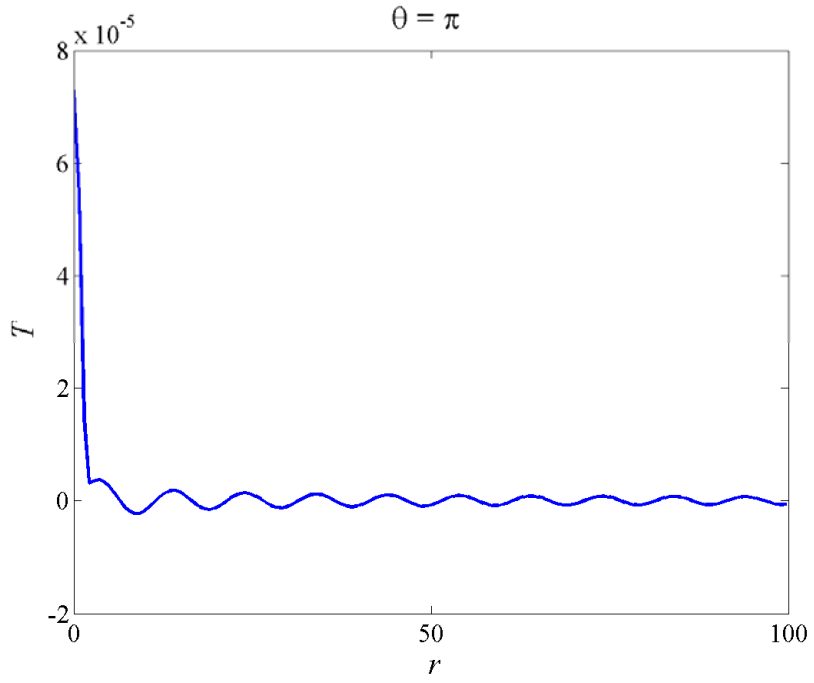

Figure 5.19(g) Scattered temperature $\hat{T}_s$ at $\theta = \pi$ for $\lambda = 10/3$

Chapter 6

Numerical Solution of Sound Scattering by a Localized Thermal Disturbance Using a Modeled BE Approach

6.1 Background

Recovery of thermal conductivity for aeroacoustic problems and the derivation of a correct thermal conductivity using Eucken's Model have been accomplished in the Chapter 4. In order to illustrate the ability to resolve thermal effect in the study of aeroacoustic problems by the modeled BE a case with thermal scattering of acoustic waves by a localized thermal disturbance has been selected for investigation. An analytical solution has been established in Chapter 5 as the basis for verification of the numerical solution, which is to be obtained by solving the modeled BE in this chapter.

As mentioned in Chapter 1, there are two common numerical schemes for solving the modeled BE, namely the lattice Boltzmann method (LBM) and the gas-kinetic scheme (GK/BE). In the preceding chapters, it has been shown that a set of unsteady NS equations was recovered with the macroscopic dimensionless numbers (*Re*, *M* and *Pr*) deduced from the numerical solution of the modeled BE. This was accomplished by invoking appropriate physical models for the transport coefficients. Although a two-relaxation-time approach based on Li et al.'s model (2006) was adopted in the recovery of a correct shear viscosity and thermal conductivity, the improved modeled BE can be solved using different numerical schemes as it is based on fundamental physical consideration. Besides, the gas-kinetic scheme has not yet been extended to tackle with any aeroacoustics problems. In view of this, the gas-

kinetic scheme is adopted to solve the improved modeled BE for the thermal acoustic scattering problem in this chapter. The numerical solution obtained by gas-kinetic scheme is therefore validated via comparison with the analytical results in the last chapter. In the following, a brief description of the gas-kinetic scheme proposed by Xu (2001) is presented. Further details are available in Xu and He (2003).

6.2 Gas-kinetic Scheme

The gas-kinetic scheme being adopted for the numerical simulation of the thermal acoustic scattering problem is based on the formulation given in Su et al. (1999) and Xu and He (2003). Due to the fact that the physical background of the gas-kinetic BGK scheme is similar to that of the LBM (both numerical schemes are developed to solve the modeled BE), focus of this section would be put on outlining the numerical details of the gas-kinetic BGK scheme.

The gas-kinetic BGK scheme is a finite volume scheme from which the mass, momentum and energy fluxes are calculated across cell interfaces. In Xu and He's model (2003), the energy equation was not solved because the formulation was intended for incompressible isothermal flow simulations. Since a significant temperature gradient is present in the thermal acoustic scattering problem, the energy equation has to be included in the gas-kinetic BGK scheme. This is accomplished by making reference to the model of Su et al. (1999) for low-speed flow simulations.

For a 2-D problem, the equilibrium distribution function of the BGK-type model in the gas-kinetic BGK scheme can be expressed as

$$f^{eq} = \rho\left(\frac{\beta}{\pi}\right)^{(K+2)/2} e^{-\beta\left[(\xi_x-u)^2+(\xi_y-v)^2+\varsigma^2\right]} \quad . \tag{6.1}$$

The expression is similar to that in equation (2.2) in Chapter 2. Here, $\beta = \frac{1}{2RT}$ and $\boldsymbol{\varsigma}$ is a vector in *K* dimensions where *K* can be regarded as the "implicit" degree of freedom. For example, for a 2-D problem with diatomic gas, the "explicit" degree of freedom is the translational ones in the *x*- and *y*-direction. The corresponding "implicit" degrees of freedom are the translational one in the *z*-direction, as well as two rotational degrees of freedom for diatomic gas. Therefore, $\boldsymbol{\chi}^2$ can be expressed as $\boldsymbol{\chi}^2 = \chi_1^2 + \chi_2^2 + ... + \chi_K^2$, where $K = 3$ for a 2-D problem with diatomic gas.

As outlined in Chapter 2, the 2-D macroscopic conservation equations are derived from the modeled BE by introducing four (for 2-D problems) collision invariants $\varphi_\alpha \quad (\alpha = 0, 1, 2, 3)$, where $\varphi_0 = 1; \varphi_{1,2} = \xi; \varphi_3 = \frac{1}{2}\left(\xi_x^2 + \xi_y^2 + \chi^2\right)$ for the 2-D gas-kinetic BGK scheme via the following equations

$$W = \begin{pmatrix} \rho \\ \rho u \\ \rho v \\ \rho e_t \end{pmatrix} = \int \varphi_\alpha f d\xi_x d\xi_y d\chi \quad . \tag{6.2}$$

The mass, momentum and energy fluxes are obtained as follows:

$$\vec{F}(W) = \begin{pmatrix} \vec{F}_\rho \\ \vec{F}_{\rho u} \\ \vec{F}_{\rho v} \\ \vec{F}_{\rho e_t} \end{pmatrix} = \int \boldsymbol{\varphi}_\alpha f d\xi_x d\xi_y d\chi \quad . \tag{6.3}$$

According to Su et al. (1999), the finite volume gas-kinetic BGK scheme is derived by integrating the modeled BE over the area of the numerical cell ($dxdy$) and further integrate the results with respect to time (dt) as follows

$$\int\left(\frac{\partial f}{\partial t}+\boldsymbol{\xi}\cdot\nabla f\right)\varphi_\alpha d\Xi=\int\left(-\frac{f-f^{eq}}{\tau}\right)\varphi_\alpha d\Xi \quad , \tag{6.4}$$

where $d\Xi=d\xi_x d\xi_y d\chi dxdydt$. For a cell Ω with boundary $\partial\Omega$, the integrating moments of f can be expressed as follows

$$\frac{d}{dt}\int_\Omega \varphi_\alpha f d\xi dV+\int_{\partial\Omega}\varphi_\alpha \xi f d\xi\cdot\boldsymbol{n}d\sigma=0 \quad . \tag{6.5}$$

where dV and $d\sigma$ represent the volume integral and the surface integral at a cell Ω with boundary $\partial\Omega$.

The resulting finite volume scheme at numerical cell Ω is constructed as

$$W_\Omega^{n+1}-W_\Omega^n=\frac{1}{\Delta S_\Omega}\sum_{k=1}^{4}\int_0^{\Delta t}\vec{F}_k\cdot\vec{l}_k dt \quad , \tag{6.6}$$

where ΔS_Ω is the area of the numerical cell Ω ; $\Delta t=t^{n+1}-t^n$; $\vec{F}_k$ is the flux across cell interfaces normal to $\vec{k}$; $\left|\vec{l}_k\right|$ is the length of the cell interface with normal direction $\vec{k}$. In order to march the macroscopic solutions from t^n to t^{n+1}, $\vec{F}_k$ in equation (6.6) should be obtained via equation (6.3). In other words, the distribution function f presents in equation (6.3) has to be determined. The corresponding calculation method based on models developed by Su et al. (1999) and Xu (2003) will be highlighted.

A formal integral solution for the distribution function in the modeled BE is expressed in the form

$$f(\boldsymbol{x},\boldsymbol{\xi},t+\Delta t)=\frac{1}{\tau}\int_{t}^{t+\Delta t} f^{eq}(\boldsymbol{x}',\boldsymbol{\xi},t')e^{-(t+\Delta t-t')/\tau}dt' + e^{-\Delta t/\tau} f_0(\boldsymbol{x}-\boldsymbol{\xi}\Delta t,\boldsymbol{\xi}), \qquad (6.7)$$

where $\boldsymbol{x}' = \boldsymbol{x} - \boldsymbol{\xi}(t+\Delta t-t')$ is the trajectory of a particle motion (Kogan 1969). In order to obtain the solution of f, the f^{eq} and f_0 on the right hand side of equation (6.6) have to be determined. Suppose there is a cell interface $x_{i+1/2}$ between two adjacent cells x_i and x_{i+1}. At the beginning of each time step Δt (assume $t=0$ for ease of demonstration), the initial distribution function $f_0(\boldsymbol{x},\boldsymbol{\xi},t=0)$ around $x_{i+1/2}$ can be expressed as

$$f_0(\boldsymbol{x},\boldsymbol{\xi},0) = f^{eq}(\boldsymbol{x}_{i+1/2},\boldsymbol{\xi},0) + f^{(1)}(\boldsymbol{x}_{i+1/2},\boldsymbol{\xi},0) + (x-x_{i+1/2})\cdot\nabla f^{eq}(\boldsymbol{x}_{i+1/2},\boldsymbol{\xi},0) \quad , \qquad (6.8)$$

where $f^{(1)} = f - f^{eq}$ is defined as the non-equilibrium distribution function. In order to solve equation (6.7), f^{eq}, $f^{(1)}$ and gradients of f^{eq} are calculated by following the procedure; the first step is to determine f^{eq} and its gradients, then the deviation distribution $f^{(1)}$ can be determined next. These procedures are briefly described below.

(1) f^{eq} and its gradients

As shown in Chapter 2, the mesoscopic distribution function can be connected with the macroscopic variables by integrating the moments of f. Due to the fact that $\int -\frac{1}{\tau}(f-f^{eq})d\xi_x d\xi_y = 0$ (compatibility condition), the connection can also be made by integrate moments of f^{eq}, i.e.,

$$\int \varphi_\alpha f^{eq} d\xi_x \xi_y d\varsigma = W_{i+1/2} = \left(\rho \quad \rho u \quad \rho v \quad \rho e_t\right)^T_{i+1/2} \quad , \tag{6.9}$$

where $W_{i+1/2}$ is the macroscopic variables at cell interface $x_{i+1/2}$. According to Xu (2003), $W_{i+1/2}$ and its gradients can be obtained from the discretized initial data W_i by a third-order central differencing interpolation scheme, i.e.

$$W_{i+1/2} = \frac{7}{12}\left(W_i + W_{i+1}\right) - \frac{1}{12}\left(W_{i-1} + W_{i+2}\right) \quad , \tag{6.10}$$

$$\left(\frac{dW}{dx}\right)_{i+1/2} = \left[\frac{5}{4}\left(W_{i+1} - W_i\right) - \frac{1}{12}\left(W_{i+2} - W_{i-1}\right)\right] / \Delta x \quad . \tag{6.11}$$

Therefore, f^{eq} is determined by substituting values from equation (6.10) into equation (6.8), using the expression of f^{eq} in equation (6.1). On the other hand, the gradients of f^{eq} is obtained by taking derivatives of equation (6.9) with values of $\left(\frac{dW}{dx}\right)_{i+1/2}$ obtained from equation (6.11) substituted into it.

(2) Determination of $f^{(1)}$

The non-equilibrium distribution function, $f^{(1)} = f - f^{eq}$ can be further expressed as

$$f^{(1)} = -\tau\left(\frac{\partial f^{eq}}{\partial t} + \boldsymbol{\xi} \cdot \nabla f^{eq}\right) = -\tau\left(a\xi_x + b\xi_y + A\right) f^{eq} \quad , \tag{6.12}$$

where $\frac{\partial f^{eq}}{\partial t} = A f^{eq}; \frac{\partial f^{eq}}{\partial x} = a f^{eq}; \frac{\partial f^{eq}}{\partial y} = b f^{eq}$ and A, a, b have expressions given by $A = A_\alpha \psi_\alpha; a = a_\alpha \psi_\alpha; b = b_\alpha \psi_\alpha$ for $\alpha = 1,2,3,4$. Furthermore, A, a, b can be determined through the following mathematical manipulation, or

$$\int \varphi_\alpha a f^{eq} d\xi_x \xi_y d\varsigma = \left(\frac{dW}{dx}\right)_{i+1/2} \quad , \tag{6.13a}$$

$$\int \varphi_\alpha b f^{eq} d\xi_x \xi_y d\varsigma = \left(\frac{dW}{dy}\right)_{i+1/2} \quad . \tag{6.13b}$$

Since

$$\int \varphi_\alpha f^{(1)} d\xi_x \xi_y d\varsigma = \int -\tau \varphi_\alpha \left(a\xi_x + b\xi_y + A\right) f^{eq} d\xi_x \xi_y d\varsigma = 0 \quad , \tag{6.13c}$$

therefore,

$$\int \varphi_\alpha A f^{eq} d\xi_x \xi_y d\varsigma = -\int \varphi_\alpha \left(a\xi_x + b\xi_y\right) f^{eq} d\xi_x \xi_y d\varsigma \quad . \tag{6.13d}$$

The coefficients A, a, b can be determined from the above relations (Xu 2001), and equation (6.8) becomes

$$f_0(\boldsymbol{x}, \xi, t) = f^{eq}\left[1 - \tau\left(a\xi_x + b\xi_y + A\right) + ax + by\right] \quad , \tag{6.14}$$

The remaining unknown in equation (6.7) is f^{eq} around the cell interface $x_{i+1/2}$ at $t = 0$. This can be determined by expanding f^{eq} about $t = 0$ as

$$f^{eq}(x, \xi, t) = f^{eq}(x_{i+1/2}, \xi, 0) + \frac{\partial f^{eq}}{\partial x} x + \frac{\partial f^{eq}}{\partial y} y + \frac{\partial f^{eq}}{\partial t} t$$

$$= f^{eq}\left(1 + ax + by + At\right) \quad . \tag{6.15}$$

Substitute equations (6.14) and (6.15) into equation (6.7), the distribution function at cell interface $x_{i+1/2}$ becomes

$$f\left(\boldsymbol{x}_{i+1/2}, \xi, t\right) = f^{eq}\left[1 - \tau\left(a\xi_x + b\xi_y + A\right) + At\right] \quad . \tag{6.16}$$

Substitue f in equation (6.16) into equation (6.3), the mass, momentum and energy fluxes across the cell interface $x_{i+1/2}$ can be calculated. Marching from $t = n$ to $t = n + 1$, equation (6.6) becomes:

$$W_{\Omega}^{n+1} = W_{\Omega}^{n}$$

$$+ \int_0^{\Delta t} \left[\frac{1}{\Delta x} \left(F(W)_{i-1/2,j} - F(W)_{i+1/2,j} \right) + \frac{1}{\Delta y} \left(F(W)_{i,j-1/2} - F(W)_{i,j+1/2} \right) \right] dt \,. \qquad (6.17)$$

Hence the density, momentum and energy inside the computational domain for every time step can be obtained.

The time matching is based on the CFL condition in accordance with Su et al. (1999). The ratio of the time step to the relaxation time is specified in the range $10 \le \Delta t / \tau_{eff} < 100$. The CFL number is set at 0.45 for the numerical simulation.

An attempt has been made to correct the Prandtl number, *Pr*, for the gas-kinetic scheme (Xu 2001). However, the approach is based on numerical consideration only. In this chapter, the gas-kinetic scheme adopted would be modified, so that the *Pr* could be corrected by invoking the Eucken model as previously outlined in Chapter 3. To avoid repetition, only the salient points for implementation of the Prandtl number correction would be highlighted.

To get a correct *Pr*, the thermal diffusivity, κ' is first corrected by the Eucken factor, f_E, based on the Eucken model using the following equation

$$\kappa' = f_E \mu = \frac{\kappa}{c_V} = f_E (\gamma - 1) \rho e \tau_{eff} \quad , \qquad (6.18)$$

where $f_E \approx 1.96$ for air. The *Pr* for air is therefore obtained via its relation to f_E and the result is

$$Pr = \frac{\mu c_P}{\kappa} = \frac{\mu \gamma c_V}{\kappa} = \frac{\gamma}{f_E} \approx 0.71 \quad . \qquad (6.19)$$

The thermal acoustic scattering problem investigated in this chapter only has open boundary; therefore, non-reflecting boundary conditions are required for its successful simulation. Since the gas-kinetic scheme and the LBM are different numerical schemes, non-reflecting boundary conditions should be tailored for each numerical scheme, respectively. Effect of different non-reflecting boundary conditions on the simulated results has been thoroughly investigated in Chapter 4 for the LBM. In this chapter, however, the main purpose is to demonstrate the thermal effect resolving ability of the modeled BE. Consequently, detailed studies on the appropriate non-reflecting boundary conditions would not be conducted. Instead, a viable non-reflecting boundary condition based on the one-dimensional Riemann invariants would be adopted for the incoming and outgoing boundaries on the left and right hand sides of the computational domain, while a zero-order extrapolation method would be applied to the upper and lower boundaries.

6.3 Numerical Simulation of Thermal Acoustic Scattering Problem

In order to make meaningful comparison with the theoretical results presented in Chapter 5, a sound scattering problem by a distributed thermal disturbance with the same problem specifications as in Chapter 5 (Figure 5.1) is studied. Numerical simulations for both the short wavelength limit (WKB limit) and the long wavelength limit (Born limit) are conducted using the gas-kinetic scheme described above and the simulated results are compared with the analytical solutions obtained in Chapter 5. Therefore, numerical solutions for the thermal acoustic scattering problem are obtained with amplitude of the incident acoustic wave given by $A = 1 \times 10^{-4}$, and the dimensions and

properties of the distributed thermal disturbance are taken to be the same as those specified in Chapter 5 (Figures 5.2, 5.3 and 5.4).

6.3.1 Case (1) $\lambda = 1/3$

The grid sizes are given by $\Delta x = \Delta y = 5\times10^{-2}$ with 400×400 grid points in the computational domain. This specification is equivalent to a physical domain with size given by $-10 \le x \le 10; -10 \le y \le 10$. The incident acoustic wave is specified at $x = -10$. The pressure and density of the incident acoustic waves, $\hat{p}_i$ and $\hat{\rho}_i$, can be referred to Figure 5.5(a) and 5.6(a), respectively.

As mentioned in Chapter 5, this case can be regarded as the short wavelength or WKB limit. The contours of the fluctuating pressure $\hat{p}$, density $\hat{\rho}$ and temperature $\hat{T}$ are shown in Figures 6.1(a), 6.2(a) and 6.3(a), respectively. A shape-edged shadow is clearly shown in the wake region behind the distributed thermal disturbance. The two-dimensional contour of the scattered pressure $\hat{p}_s$ deduced by taking the difference between the pressure fluctuation $\hat{p}$ and the pressure of the incident acoustic waves $\hat{p}_i$ is shown in Figure 6.4(a). As shown in Figure 6.5(a), peak scattering occurs along the *x*-axis behind the distributed thermal disturbance. This is accompanied by secondary peaks at approximately $\theta = \pm\frac{\pi}{6}$. The results show good agreement with the analytical solutions presented in the last chapter. However, the amplitude of the peak and the secondary peak scattering are 1.25×10^{-4} and 0.58×10^{-4}, respectively, and are smaller than

the corresponding values deduced from the analytical solution (1.38×10^{-4} and 0.62×10^{-4}, see Figure 5.11(a)). The reduction in scattering amplitude can be explained by the non-linear interaction between the incident acoustic waves and the distributed thermal disturbance. The modulation of the amplitude of the scattering waves, resulting from the non-linear thermal-acoustic interaction, is revealed by this one-step aeroacoustics simulation obtained by solving the improved modeled BE. On the other hand, the distributed thermal disturbance is assumed to have negligible effect on the incident sound waves for the theoretical analysis.

Apart from the good agreement of peak scattering with the analytical solution, numerical error in the form of high frequency oscillations is detected in Figure 6.5(a). This numerical error can be explained by the fact that the non-reflecting boundary condition based on Riemann invariants is not truly non-reflecting for scattered waves with any angle of incidence approaching the outgoing boundaries. In fact, the Riemann invariants are most effective for outgoing waves that are normal to the open boundaries only. In this $\lambda = 1$ case, most of the scattered waves are concentrated at the wake region of the distributed thermal disturbance. As a result, most of the scattered waves exit the outgoing boundary at small angles of incidence; this means that the Riemann invariants are approximately valid and the scattering field is not much altered by the small amount of reflected waves bouncing back from the open boundaries.

The corresponding variation of scattering amplitude from θ equals to 0 to π along radius originated from the center of the thermal disturbance is

illustrated in Figures 6.6(a) to 6.6(g). This dissection of scattered field with respect to different θ shows clearly the modulation of scattering amplitude by the non-linear thermal-acoustic interaction and the numerical errors detected with increasing θ.

The scattered density, $\hat{\rho}_s$, is obtained from $\hat{\rho}_s = \hat{\rho} - \hat{\rho}_i$ and is shown in Figure 6.8(a). Theoretically, the amplitude of $\hat{\rho}_s$ should be the same as $\hat{p}_s$, due to the isentropic relation $(\hat{p}_i + \hat{p}_s) = a_\infty^2 (\hat{\rho}_i + \hat{\rho}_s)$, where $\hat{p}_i$ and $\hat{\rho}_i$ have the same amplitude. Despite the numerical error resulting from the reflection of scattered waves by the open boundaries, the amplitude of $\hat{\rho}_s$ in Figure 6.9(a) matches with $\hat{p}_s$ in Figure 6.6(a). Therefore, the isentropic relation between $\hat{p}$ and $\hat{\rho}$ is preserved by the gas-kinetic scheme.

The scattered temperature $\hat{T}_s$ is evaluated from the equation of state, once $\hat{p}_s$ and $\hat{\rho}_s$ are known. The corresponding 2-D contour and the directivity plot are shown in Figures 6.10(a) and 6.11(a), respectively. Again, the alteration of scattering amplitude due to the non-linear thermal-acoustic interaction is replicated as that shown by $\hat{p}_s$ and $\hat{\rho}_s$, with numerical error detected starting at $\theta \geq \frac{\pi}{18}$.

6.3.2 Case (2) $\lambda = 10/3$

The grid size for this case is again chosen to be $\Delta x = \Delta y = 5 \times 10^{-2}$ with the same number of grid points, i.e. 400×400, in the computational domain. By re-scaling the size of the distributed thermal disturbance just as in Case (2) of the theoretical analysis, physically the computational domain

represents a size given by $-100 \le x \le 100; -100 \le y \le 100$. The incident acoustic wave is specified at $x = -100$. The pressure and density of the incident acoustic waves, $\hat{p}_i$ and $\hat{\rho}_i$ can be deduced from Figure 5.5(b) and 5.6(b), respectively.

Since the radius of the distributed thermal disturbance is 0.3 times the incident acoustic waves, it can be regarded as the long wavelength or Born limit. The contours of the fluctuating pressure $\hat{p}$, density $\hat{\rho}$ and temperature $\hat{T}$ are shown in Figures 6.1(b), 6.2(b) and 6.3(b), respectively. No shape-edged shadow is detected, instead the scattering waves spread out more or less uniformly at about $-\frac{7\pi}{18} \le \theta \le \frac{7\pi}{18}$. As shown in Figure 6.4(b) for the scattered pressure, $\hat{p}_s$, the fundamental scattering field is replicated by the gas-kinetic scheme. However, a significant reflection of the scattered waves is detected and captured in these 2-D contours, as well as in the directivity plot in the succeeding Figure 6.5(b). Since the scattered waves enclosed a much wider angle ($-\frac{7\pi}{18} \le \theta \le \frac{7\pi}{18}$) compared to Case (1), the angle of incidence for the scattered wave exiting the open boundaries is too large. Therefore, Riemann invariants are not sufficient to guarantee true "non-reflecting" boundary conditions for the scattered waves, and the scattered field is therefore superimposed by the reflected waves from the boundaries. As a result, the fundamental scattering pattern can be recognized but the amplitude of the scattered waves is contaminated by numerical noise. The phenomenon is revealed clearly by the variation of scattering amplitude for θ ranging from

0 to π along radii originated from the center of the thermal disturbance (Figures 6.7(a) to 6.7(g)).

The 2-D contours and directivity plots for the scattered density $\hat{\rho}_s$ are shown in Figures 6.8(b) and 6.9(b), respectively. Since the scattered field is contaminated by the reflected waves from the boundaries, only the basic scattering pattern can be replicated but not the scattered amplitudes. Consequently, the isentropic relation cannot be deduced from the figures.

Again, the scattering pattern can be seen from the 2-D contours for the scattered temperature $\hat{T}_s$, while the scattering waves are superimposed with numerical noise as shown in Figure 6.11(b). The same phenomenon can be seen from the variation of scattering amplitude for θ ranging from 0 to π along radii originated from the center of the thermal disturbance (Figures 6.13(a) to 6.13(g)).

6.4 Summary

The thermal effect resolving ability of the modeled BE is demonstrated by an investigation of a thermal acoustic scattering problem. Two limiting cases $\lambda = 1/3$ (short wavelength limit) and $\lambda = 10/3$ (long wavelength limit) are studied. The gas-kinetic scheme was adopted as the numerical scheme used to solve the modeled BE. The scheme is improved so that the Prandtl number, *Pr*, is corrected by invoking the Eucken model as highlighted in Chapter 3. Open boundary conditions based on Riemann invariants (left and right boundaries) and zero-order extrapolation method (upper and lower

boundaries) are invoked for the numerical simulations. The numerical results obtained are compared with the analytical solutions obtained in chapter 5.

For the $\lambda = 1/3$ case, the results show good agreement with the theoretical solutions. Also, the non-linear thermal-acoustic interaction between the distributed thermal disturbance and the incident acoustic waves are appropriately revealed by this one-step aeroacoustic simulation, whereas the corresponding thermal-acoustic interaction is not considered in the analytical solutions, or any other two-step numerical schemes for aeroacoustic simulations. The computational boundaries based on Riemann invariants are sensitive to the angle of incidence of the exiting waves. Since the scattering waves are concentrated in the wake region of the distributed thermal disturbance, most of the scattered waves are exiting the non-reflecting boundaries with small angle of incidence at the open boundaries. Therefore, both the scattering pattern and the amplitudes are preserved, and the discrepancy in scattering amplitudes between the numerical and the theoretical results could be attributed to the different physics embodied in the assumptions of the two approaches.

For the $\lambda = 10/3$ case, due to the large obliqueness of the scattered waves propagating towards the exiting boundaries, only the fundamental scattering pattern is recognized, while the scattering amplitudes cannot be compared with that obtained from theoretical analysis as they are superimposed with the reflected waves from the open boundaries.

So far only qualitative comparison has been made between the theoretical and numerical solutions obtained by GKS. Quantitative

comparison between these two solutions are not suitable, unless an appropriate boundary condition is applied to the numerical scheme, such that the difference between two results are solely due to the non-linear effect accounted for by the one-step method, while it is neglected in theoretical solution by solving the linearized Euler equations.

(a)

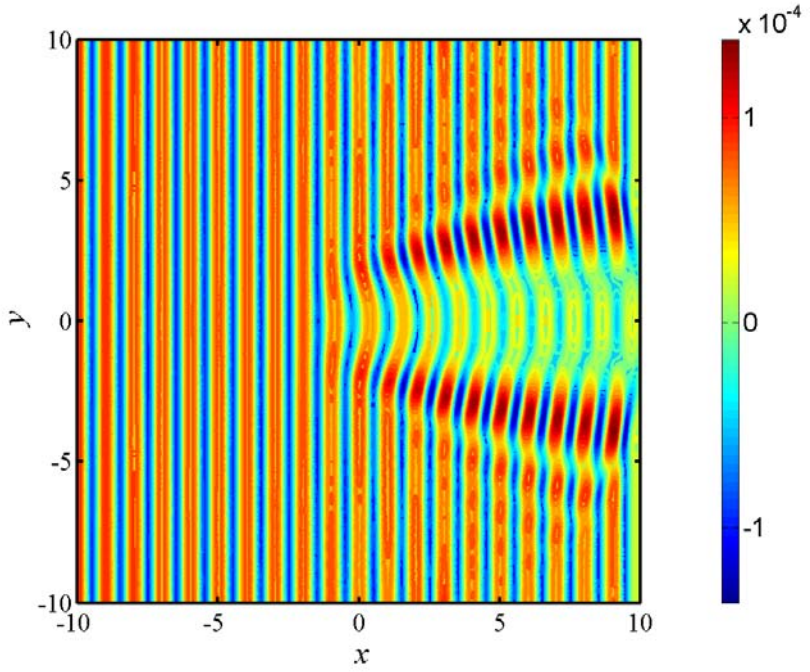

(b)

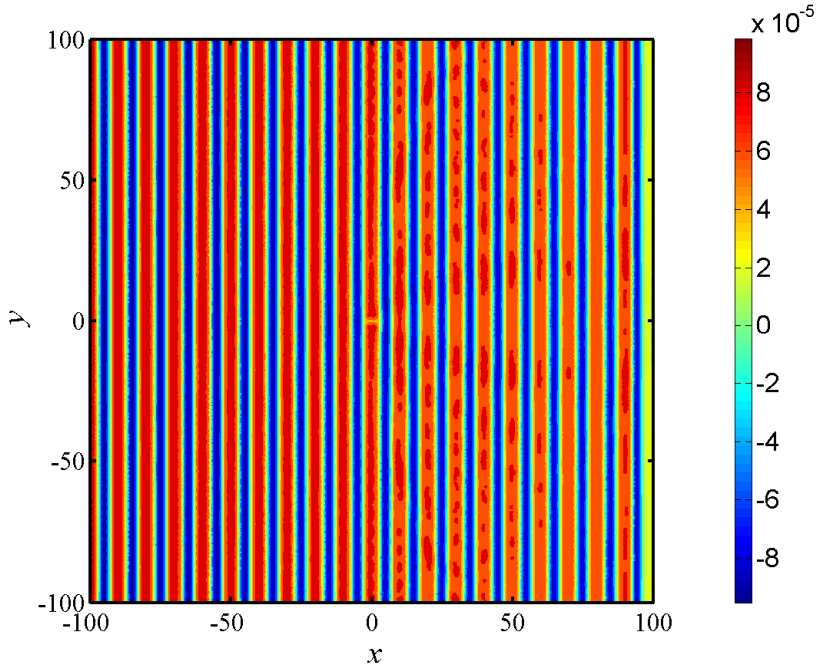

Figure 6.1 Pressure fluctuation of the acoustic scattering problem, $\hat{p}$ (a) $\lambda = 1/3$; (b) $\lambda = 10/3$

(a)

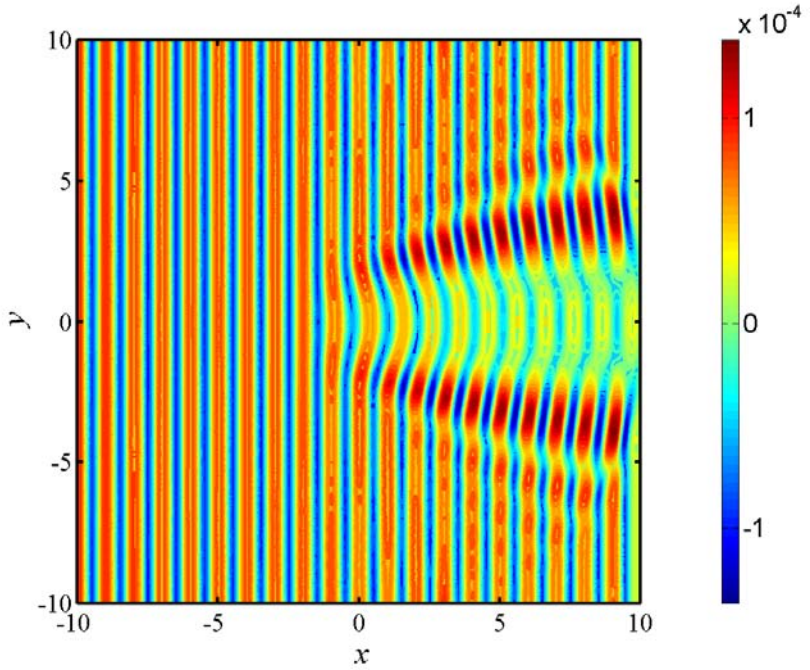

(b)

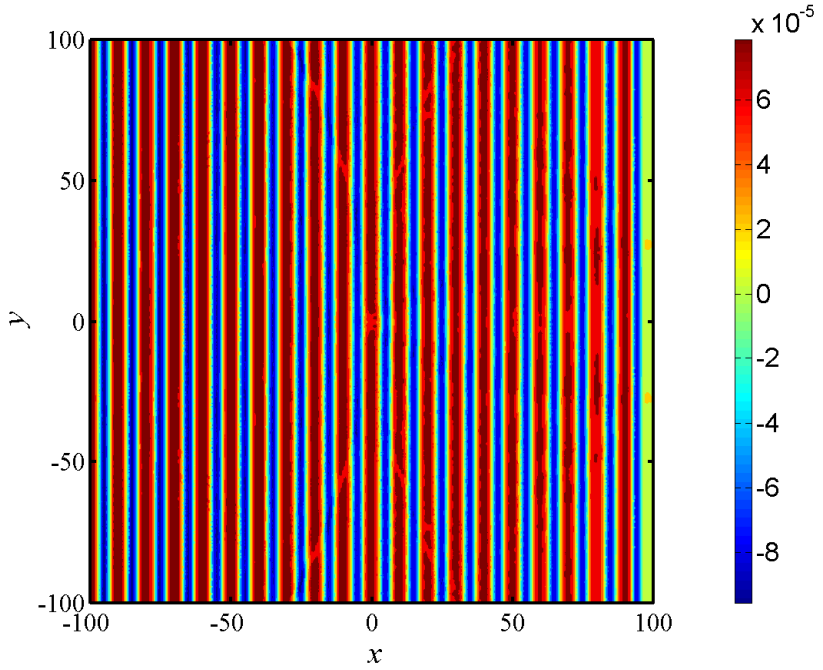

Figure 6.2 Density fluctuation of the acoustic scattering problem, $\hat{\rho}$ (a) $\lambda = 1/3$; (b) $\lambda = 10/3$

(a)

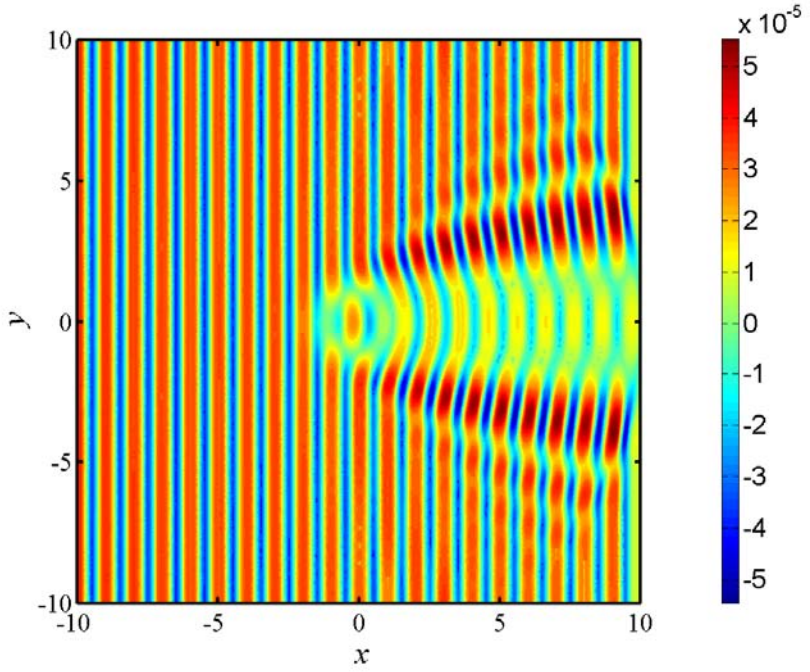

(b)

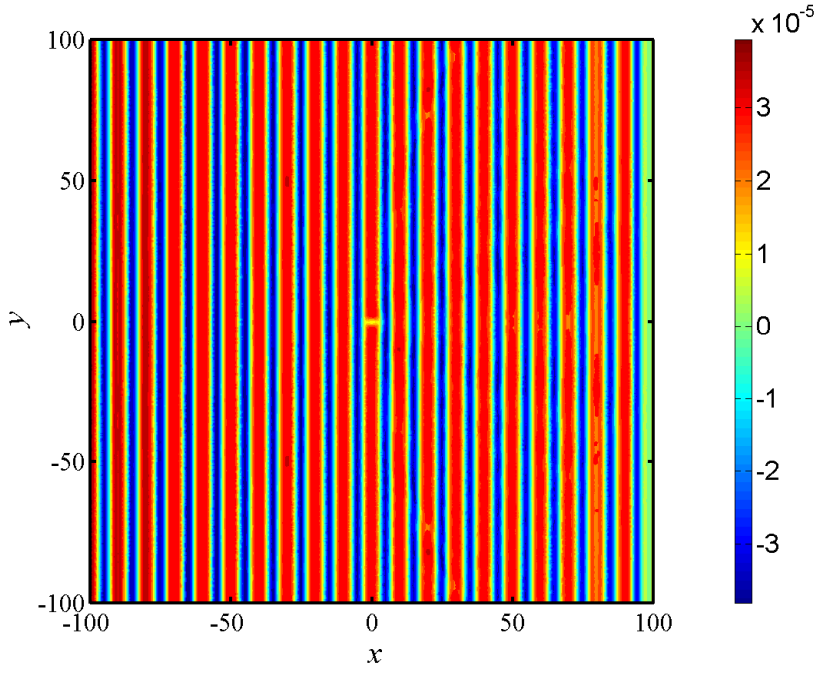

Figure 6.3 Temperature fluctuation of the acoustic scattering problem, $\hat{T}$ (a) $\lambda = 1/3$; (b) $\lambda = 10/3$

(a)

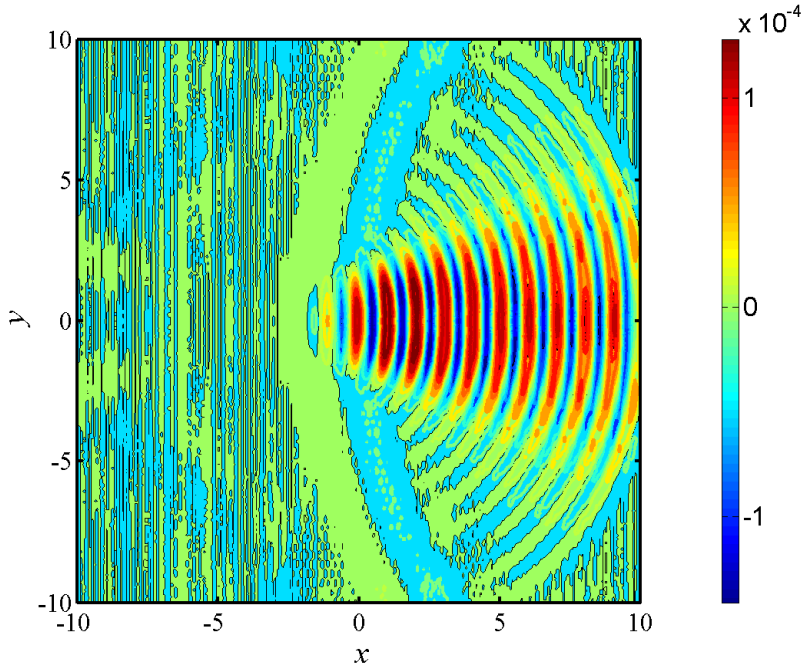

(b)

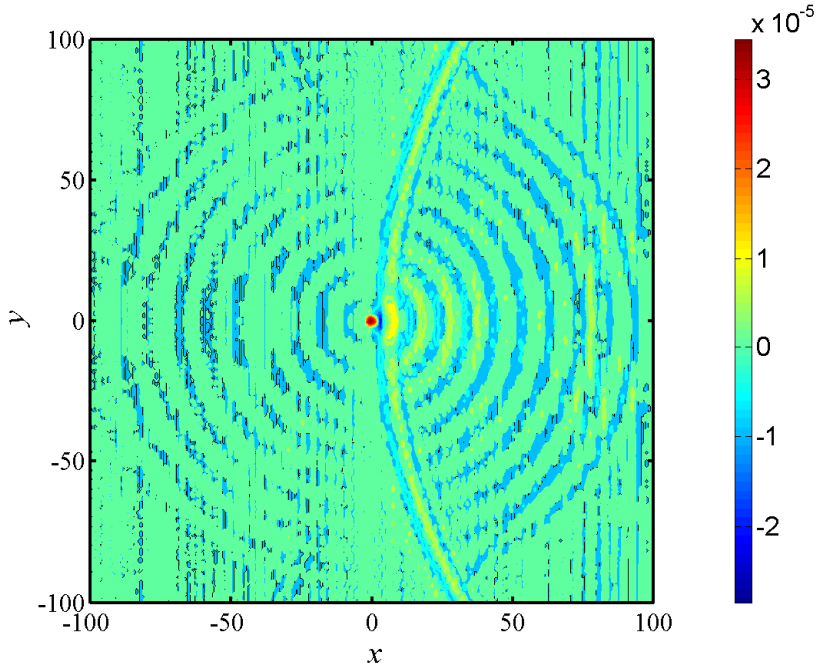

Figure 6.4 Scattered pressure distribution (2D contour), $\hat{p}_s$ (a) $\lambda = 1/3$; (b) $\lambda = 10/3$

(a)

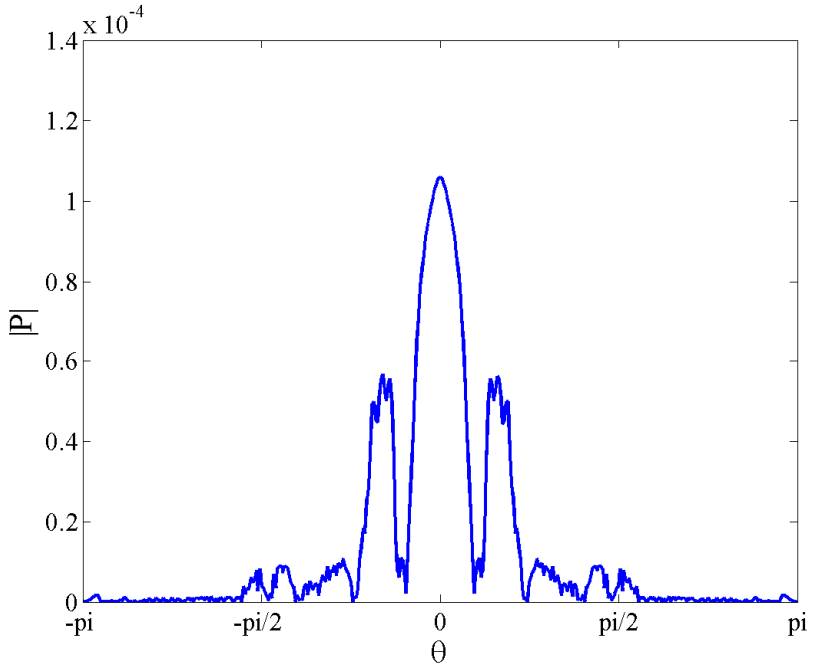

(b)

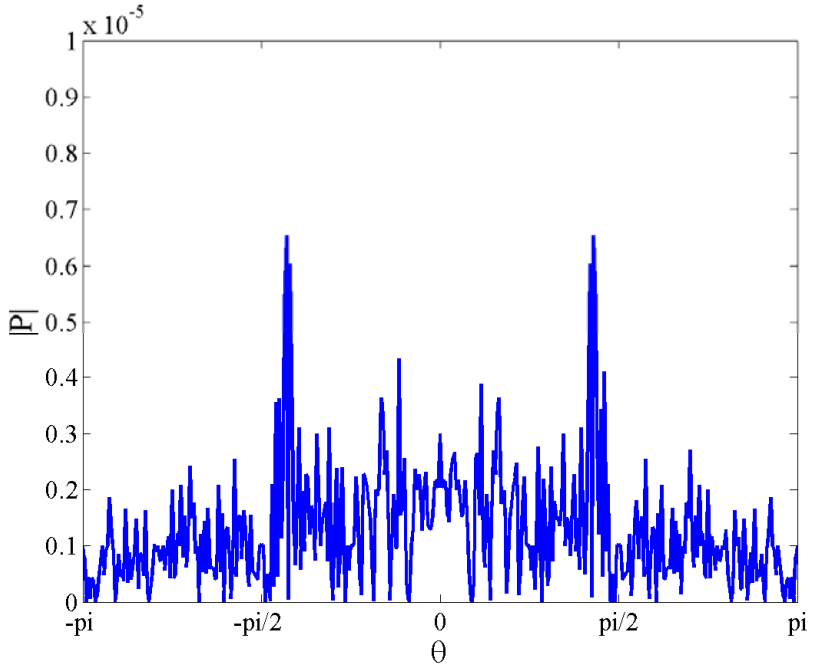

Figure 6.5 Scattered pressure level of the acoustic scattering problem, $\hat{p}_s$ at $r/\lambda^* = 7$ (a) $\lambda = 1/3$; (b) $\lambda = 10/3$

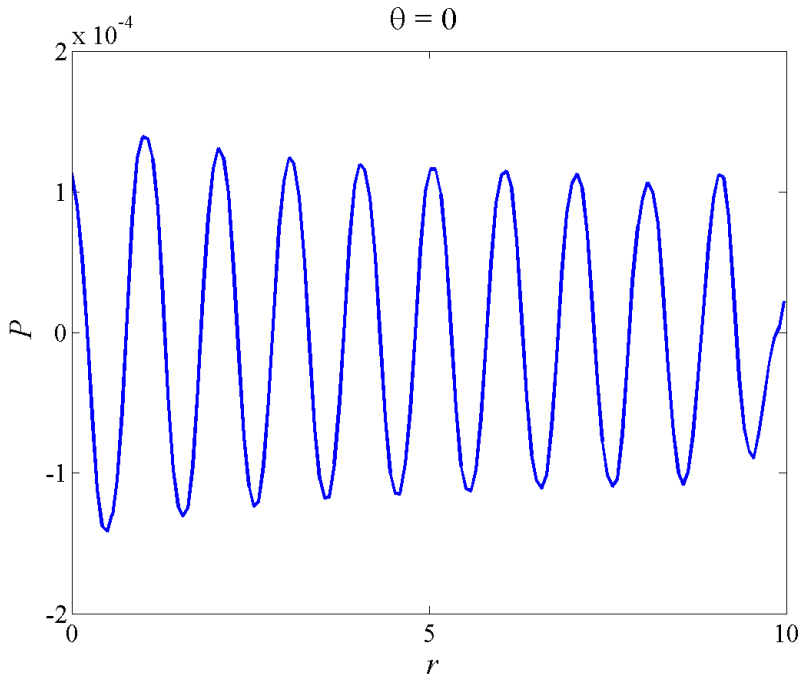

Figure 6.6(a) Scattered pressure $\hat{p}_s$ at $\theta = 0$ for $\lambda = 1/3$

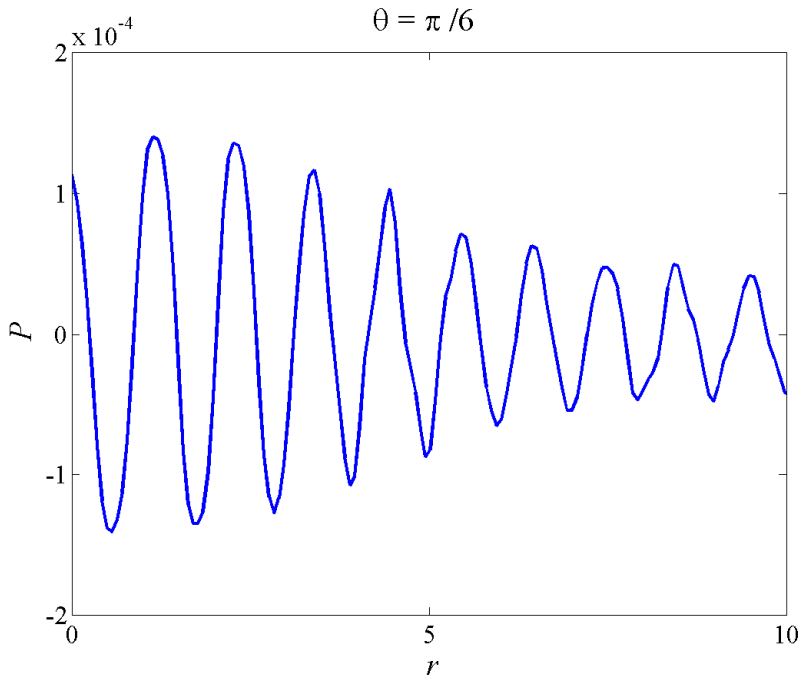

Figure 6.6(b) Scattered pressure $\hat{p}_s$ at $\theta = \pi/6$ for $\lambda = 1/3$

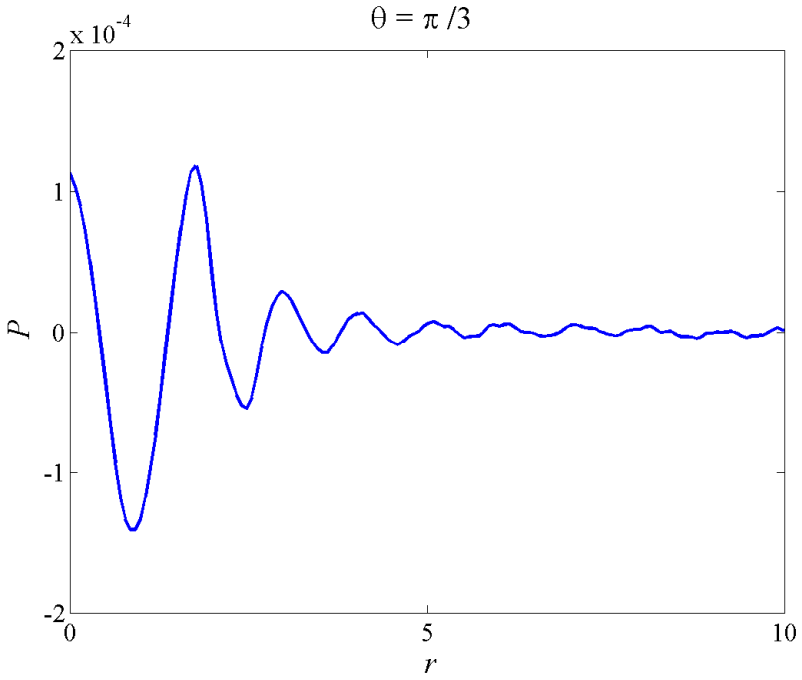

Figure 6.6(c) Scattered pressure $\hat{p}_s$ at $\theta = \pi/3$ for $\lambda = 1/3$

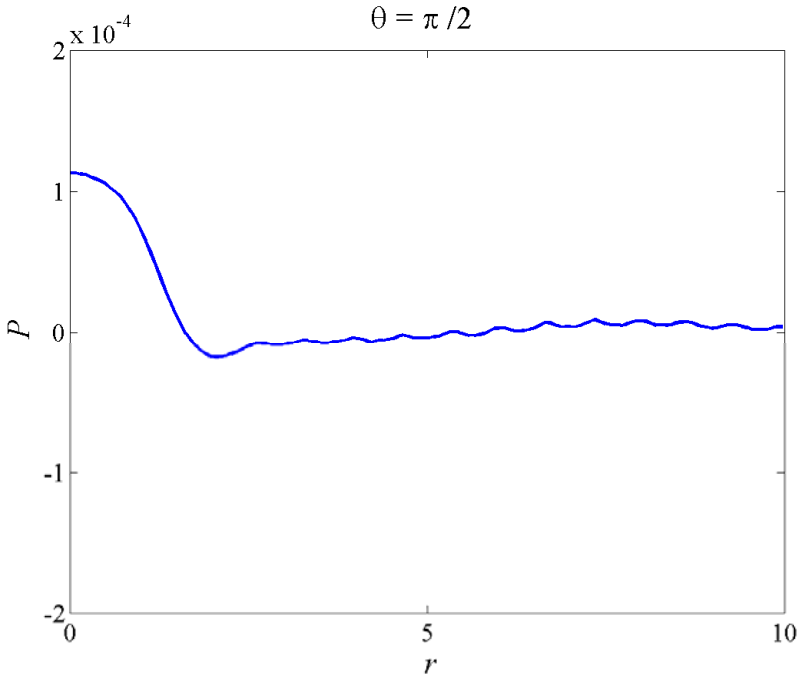

Figure 6.6(d) Scattered pressure $\hat{p}_s$ at $\theta = \pi/2$ for $\lambda = 1/3$

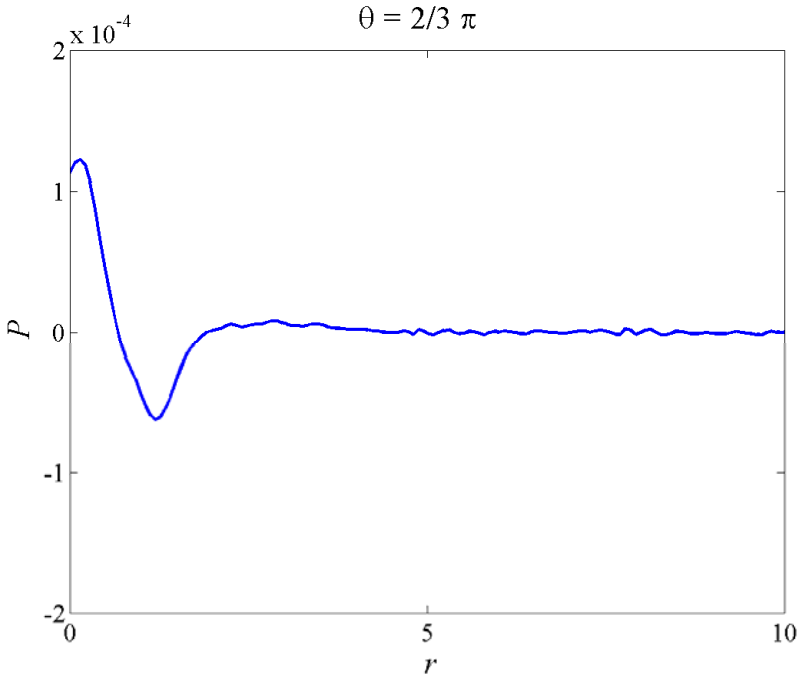

Figure 6.6(e) Scattered pressure $\hat{p}_s$ at $\theta = 2\pi/3$ for $\lambda = 1/3$

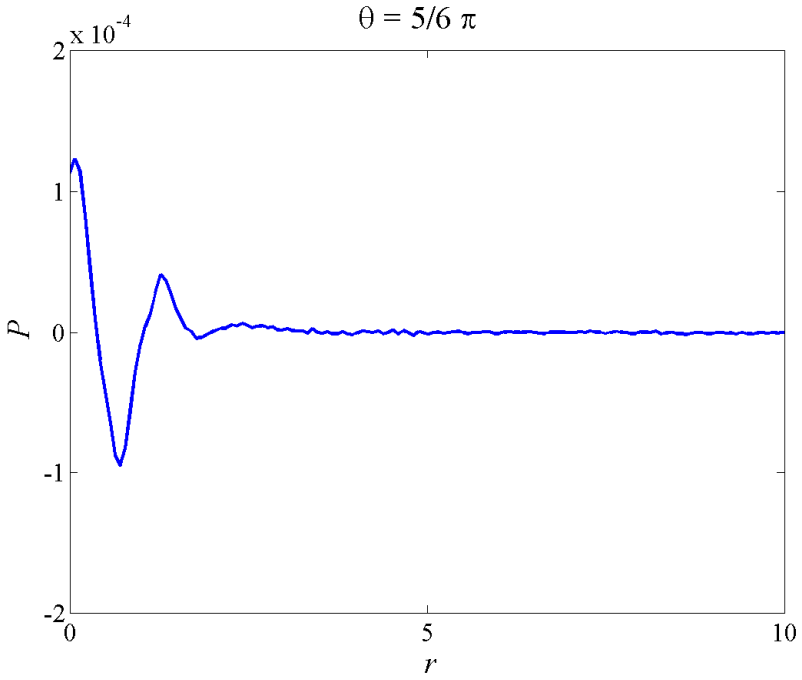

Figure 6.6(f) Scattered pressure $\hat{p}_s$ at $\theta = 5\pi/6$ for $\lambda = 1/3$

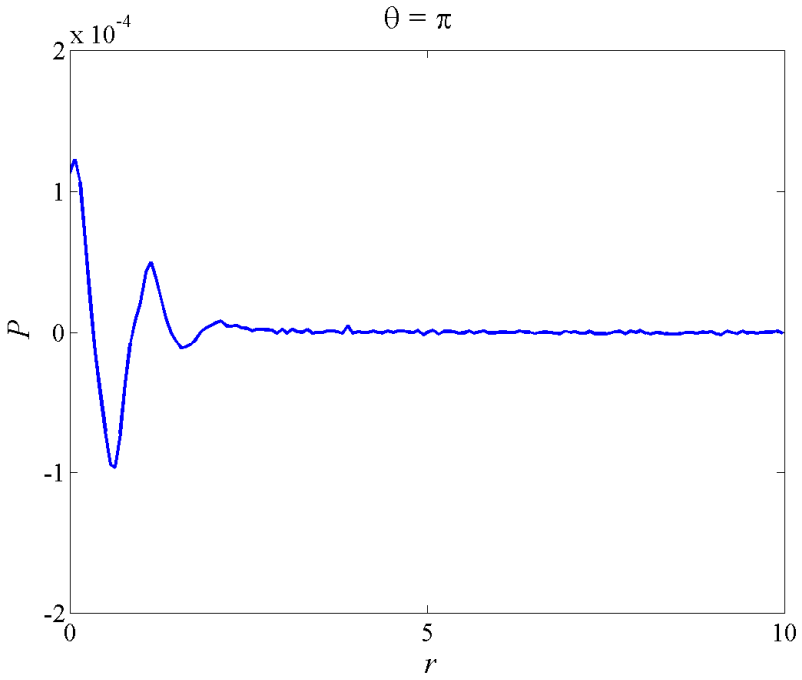

Figure 6.6(g) Scattered pressure $\hat{p}_s$ at $\theta = \pi$ for $\lambda = 1/3$

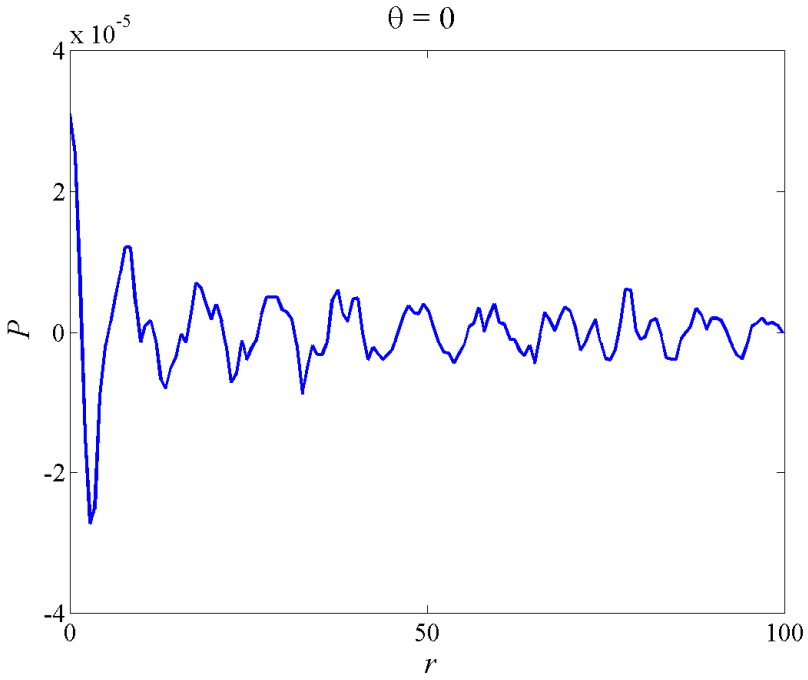

Figure 6.7(a) Scattered pressure $\hat{p}_s$ at $\theta = 0$ for $\lambda = 10/3$

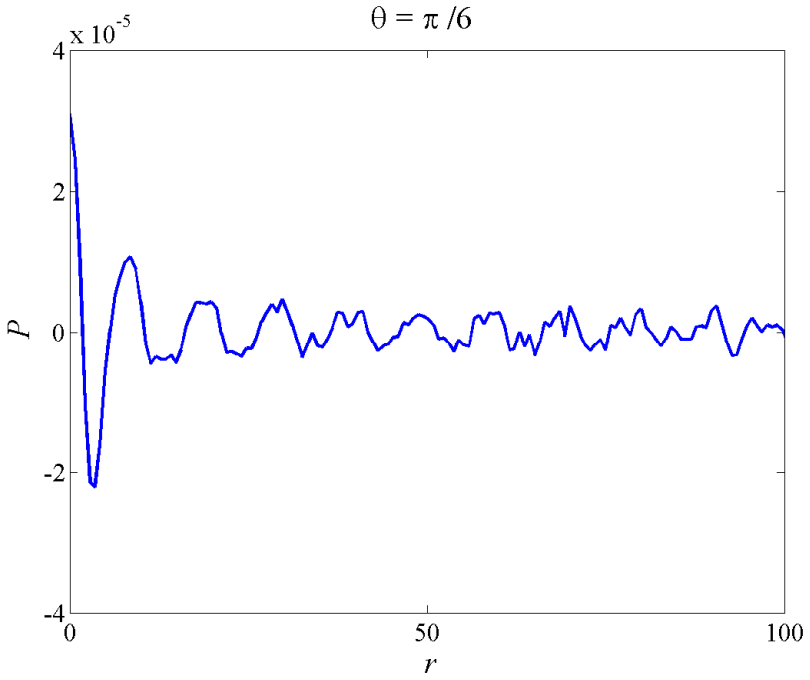

Figure 6.7(b) Scattered pressure $\hat{p}_s$ at $\theta = \pi/6$ for $\lambda = 10/3$

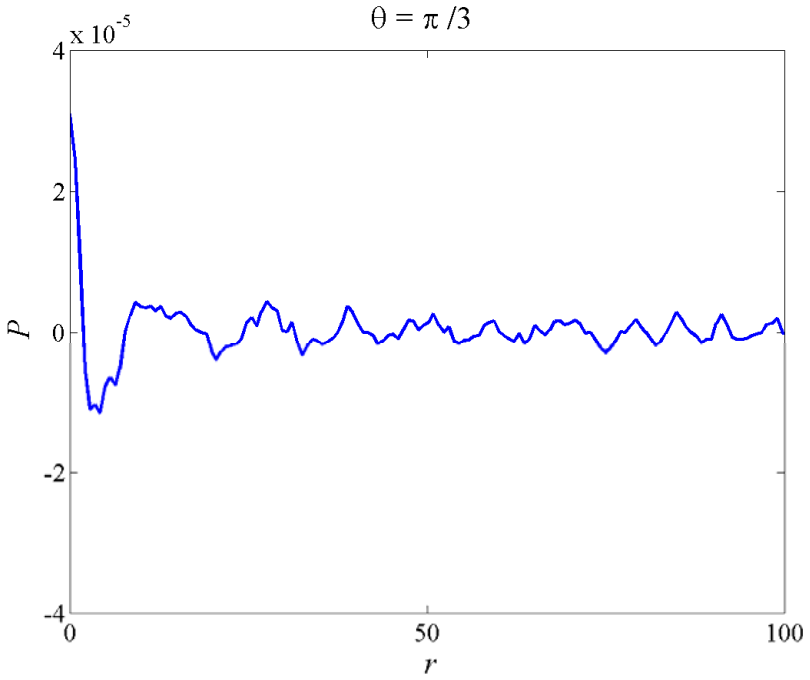

Figure 6.7(c) Scattered pressure $\hat{p}_s$ at $\theta = \pi/3$ for $\lambda = 10/3$

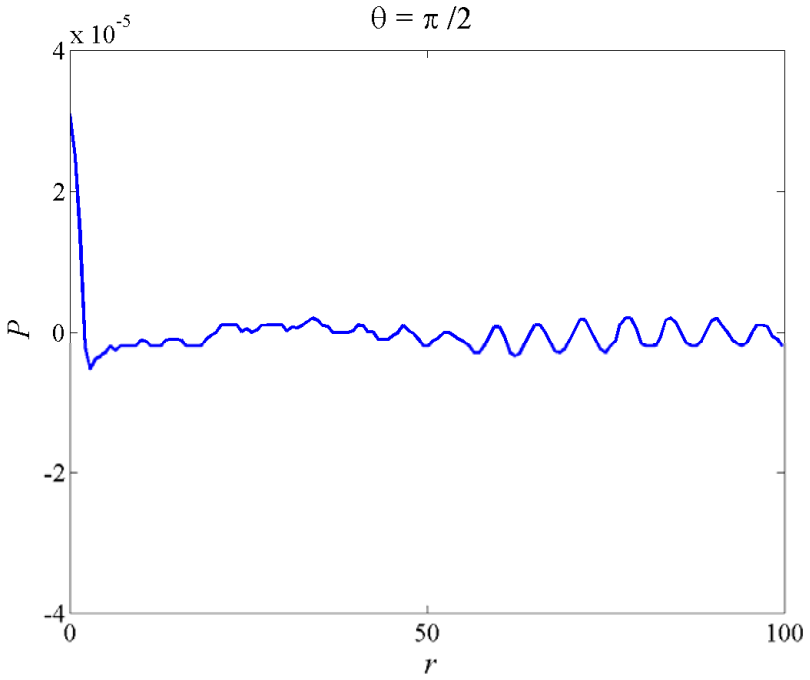

Figure 6.7(d) Scattered pressure $\hat{p}_s$ at $\theta = \pi / 2$ for $\lambda = 10/3$

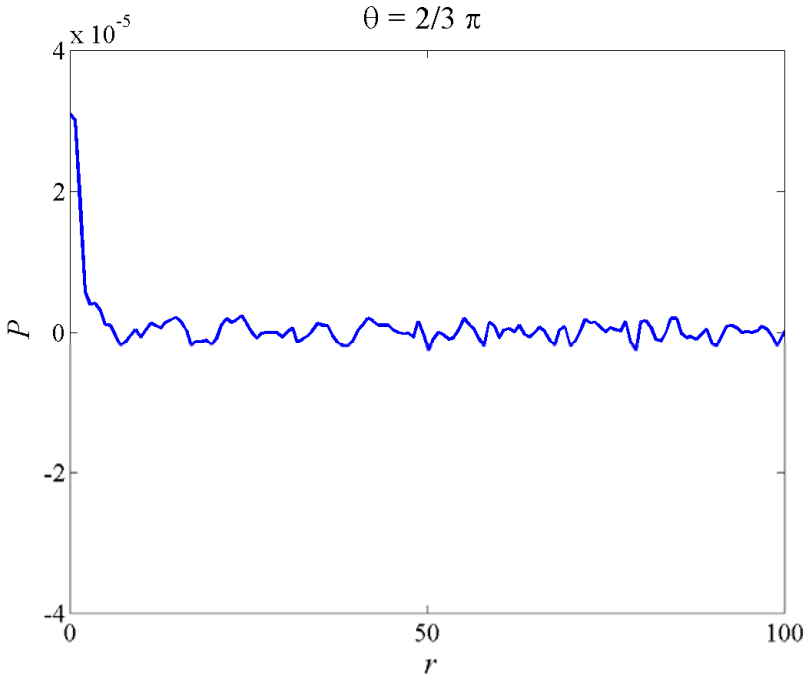

Figure 6.7(e) Scattered pressure $\hat{p}_s$ at $\theta = 2\pi / 3$ for $\lambda = 10/3$

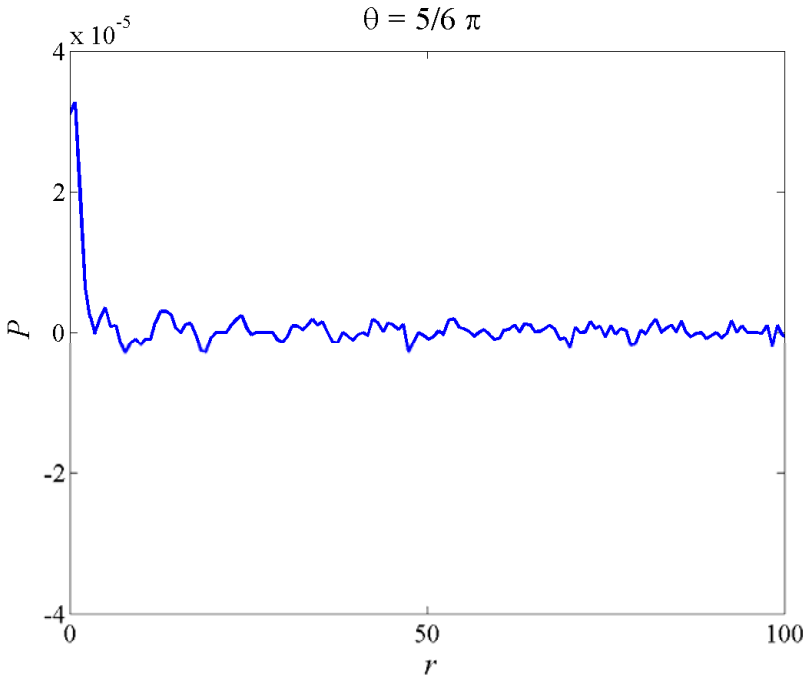

Figure 6.7(f) Scattered pressure $\hat{p}_s$ at $\theta = 5\pi/6$ for $\lambda = 10/3$

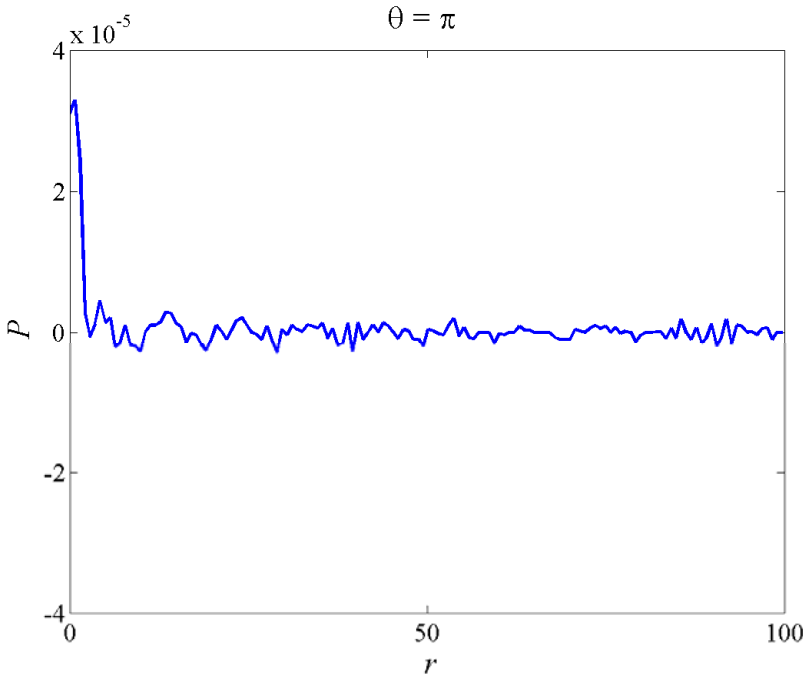

Figure 6.7(g) Scattered pressure $\hat{p}_s$ at $\theta = \pi$ for $\lambda = 10/3$

(a)

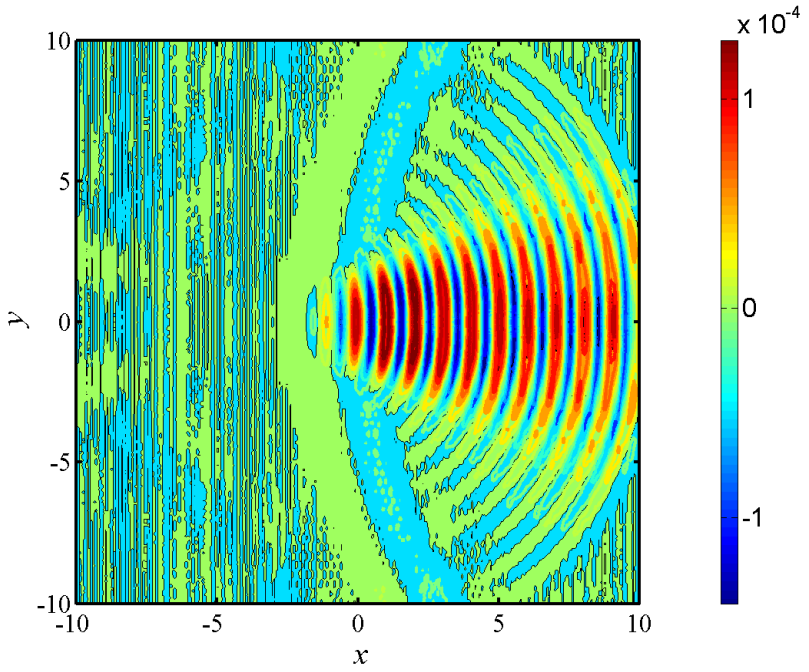

(b)

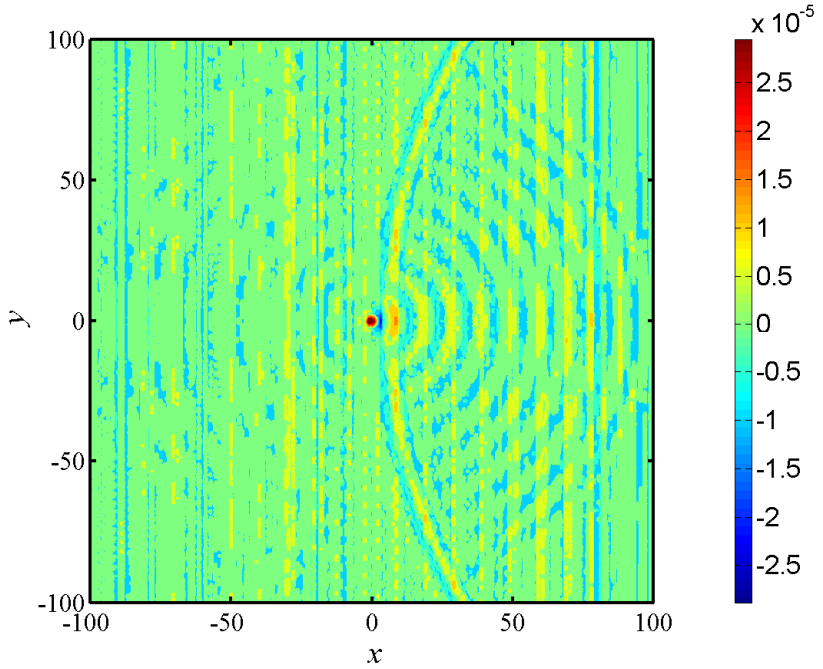

Figure 6.8 Scattered density distribution (2D contour), $\hat{\rho}_s$ (a) $\lambda = 1/3$; (b) $\lambda = 10/3$

(a)

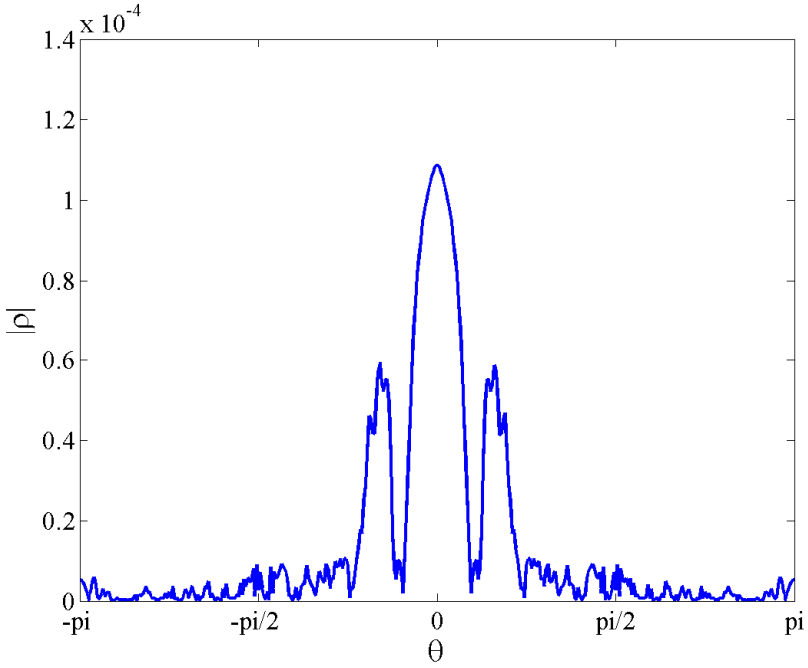

(b)

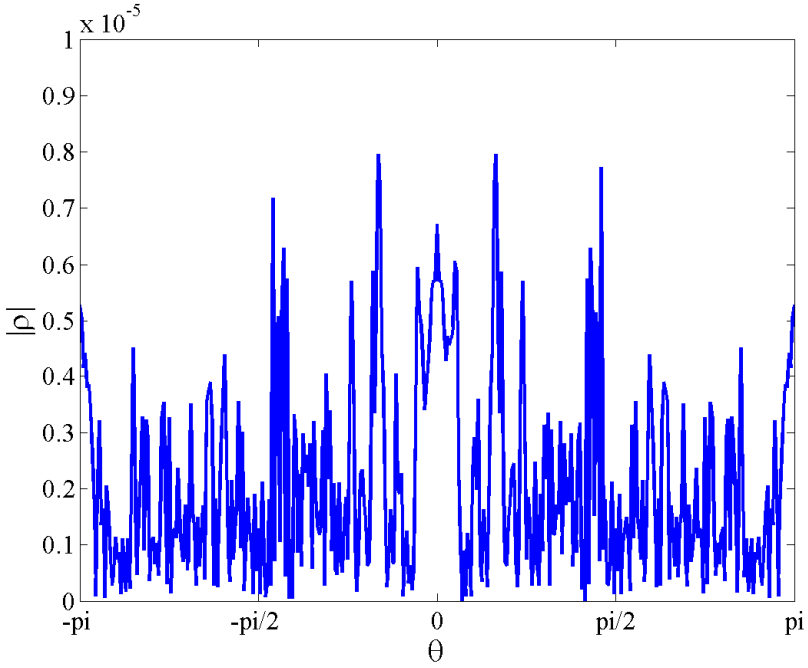

Figure 6.9 Scattered density level of the acoustic scattering problem, $\hat{\rho}_s$ at $r/\lambda^* = 7$ (a) $\lambda = 1/3$; (b) $\lambda = 10/3$

(a)

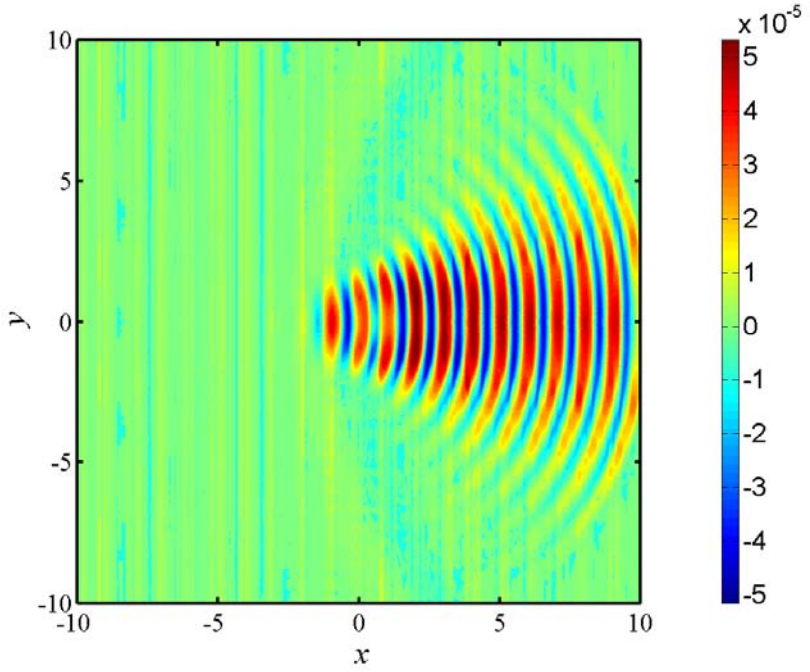

(b)

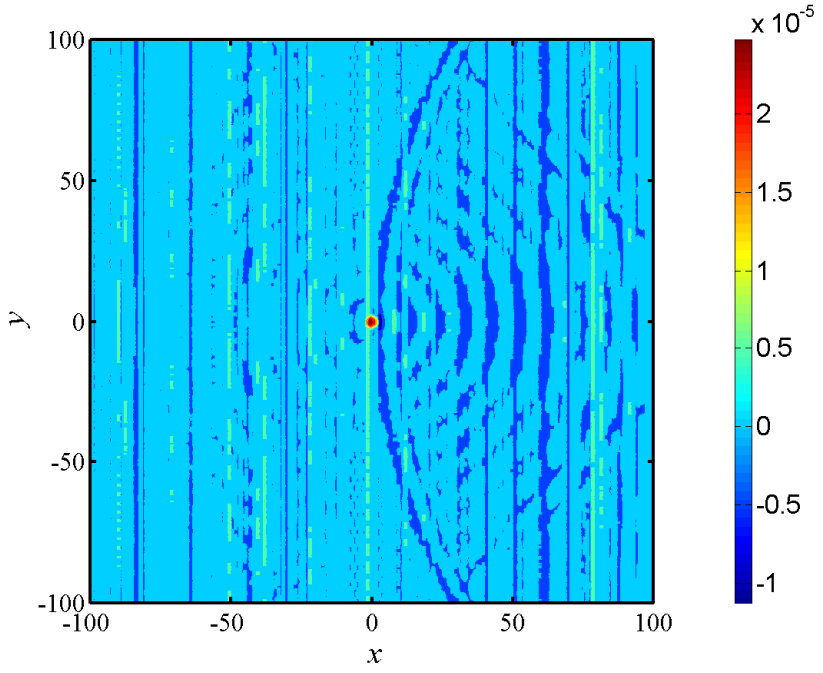

Figure 6.10 Scattered temperature distribution (2D contour), $\hat{T}_s$ (a) $\lambda = 1/3$;

(b) $\lambda = 10/3$

(a)

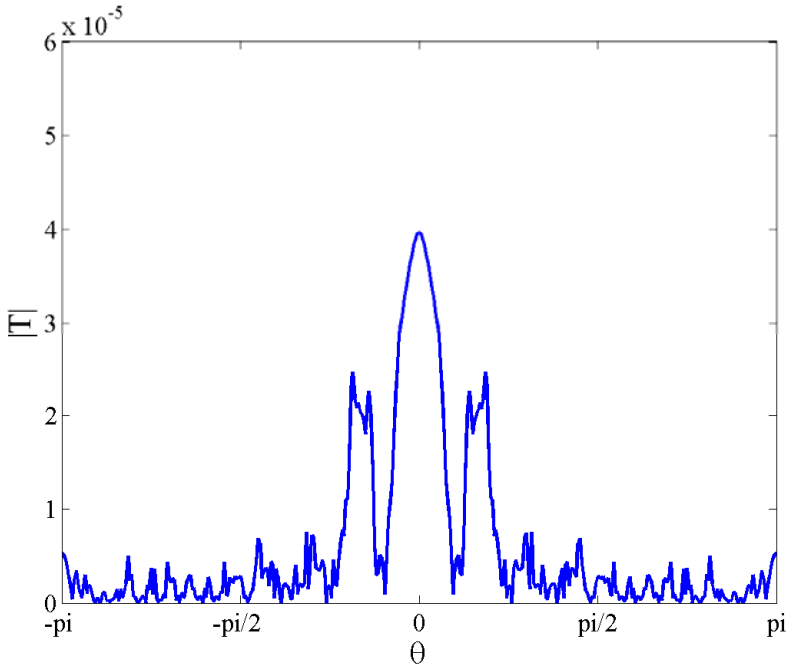

(b)

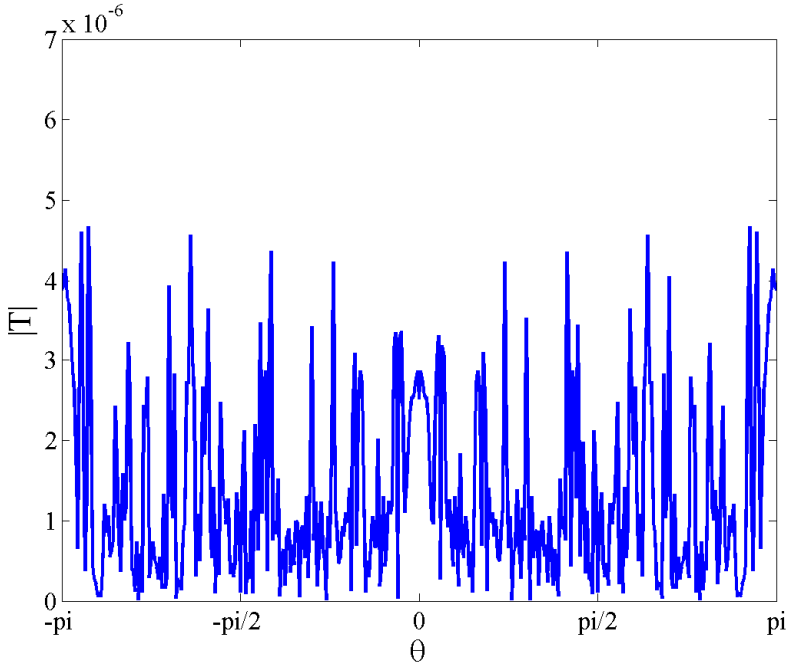

Figure 6.11 Scattered temperature level of the acoustic scattering problem, $\hat{T}_s$ at $r/\lambda^* = 7$ (a) $\lambda = 1/3$; (b) $\lambda = 10/3$

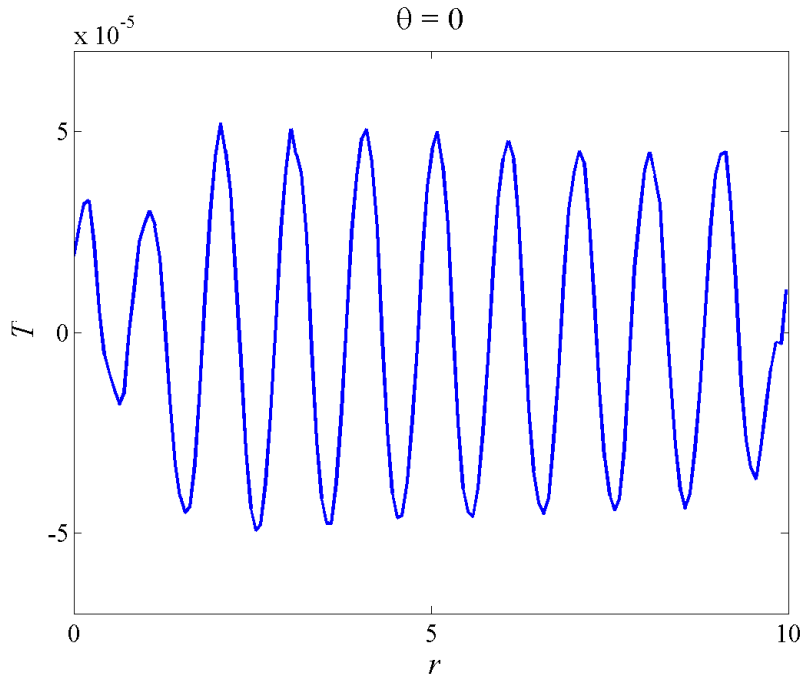

Figure 6.12(a) Scattered $\hat{T}_s$ at $\theta = 0$ for $\lambda = 1/3$

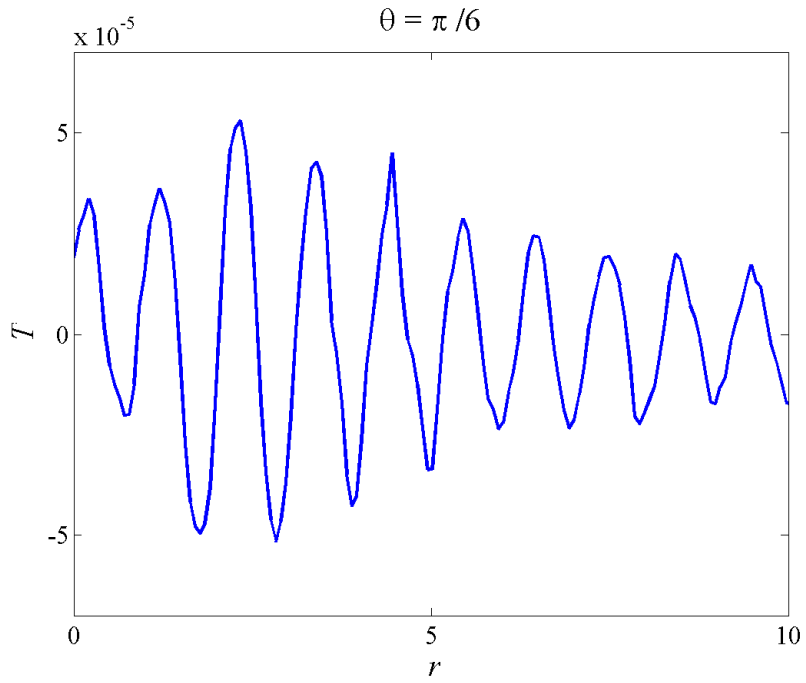

Figure 6.12(b) Scattered temperature $\hat{T}_s$ at $\theta = \pi/6$ for $\lambda = 1/3$

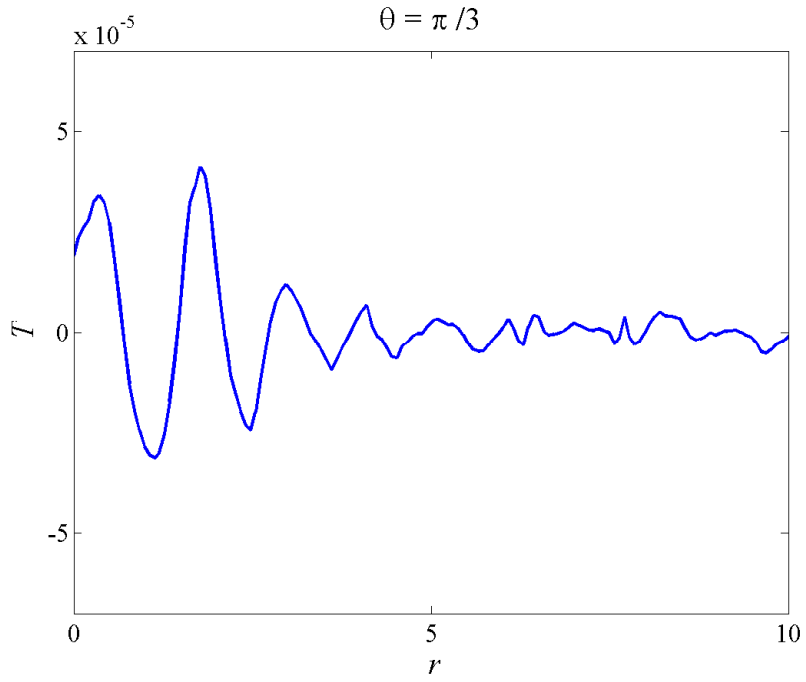

Figure 6.12(c) Scattered temperature $\hat{T}_s$ at $\theta = \pi/3$ for $\lambda = 1/3$

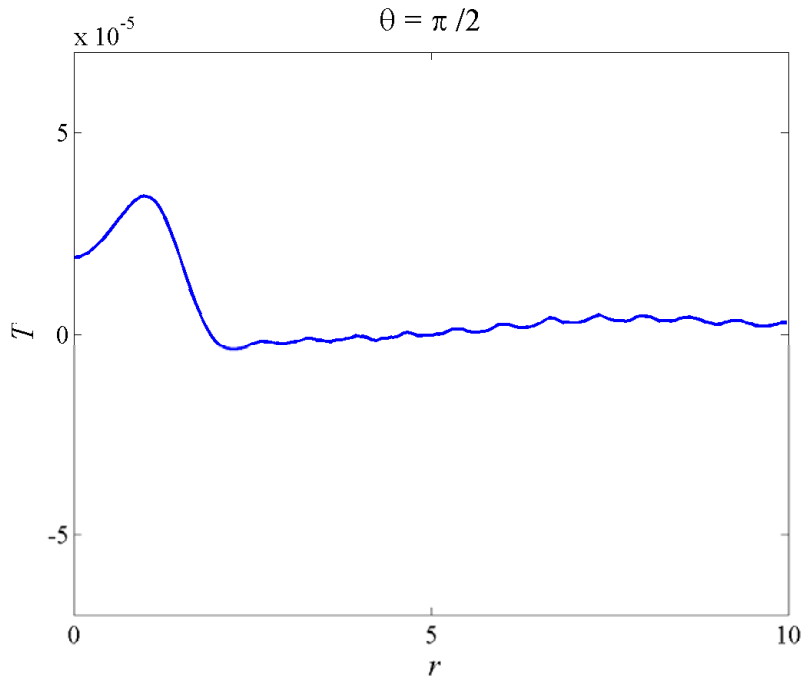

Figure 6.12(d) Scattered temperature $\hat{T}_s$ at $\theta = \pi/2$ for $\lambda = 1/3$

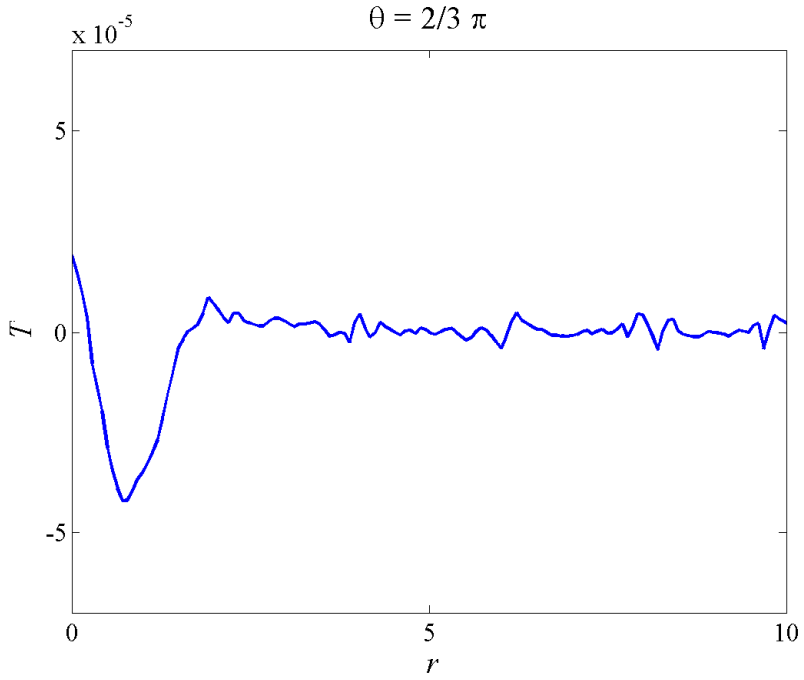

Figure 6.12(e) Scattered temperature $\hat{T}_s$ at $\theta = 2\pi/3$ for $\lambda = 1/3$

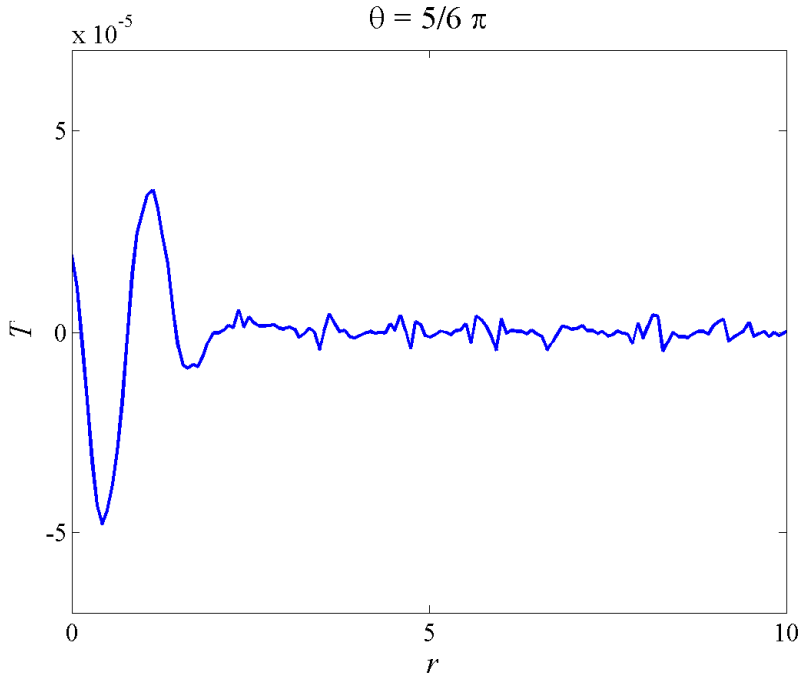

Figure 6.12(f) Scattered temperature $\hat{T}_s$ at $\theta = 5\pi/6$ for $\lambda = 1/3$

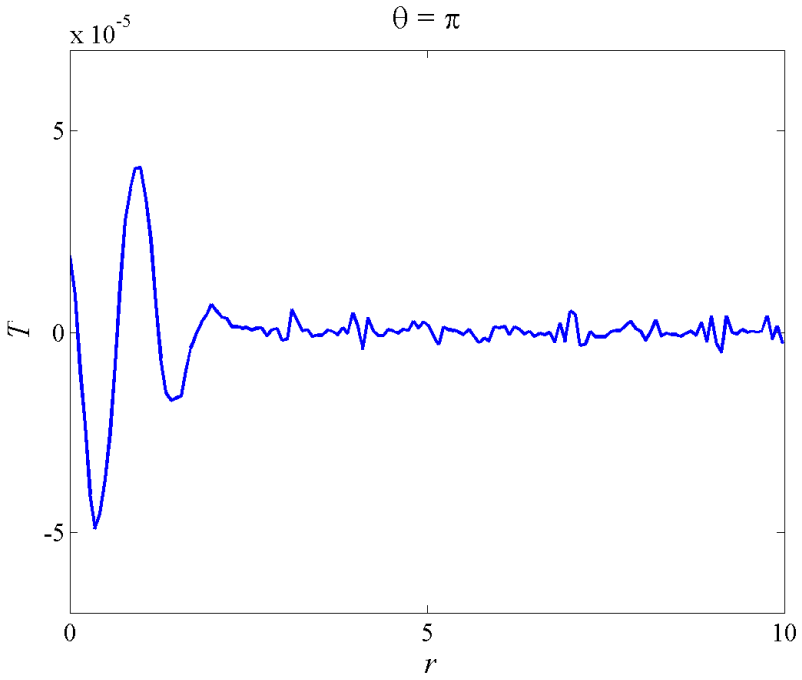

Figure 6.12(g) Scattered temperature $\hat{T}_s$ at $\theta = \pi$ for $\lambda = 1/3$

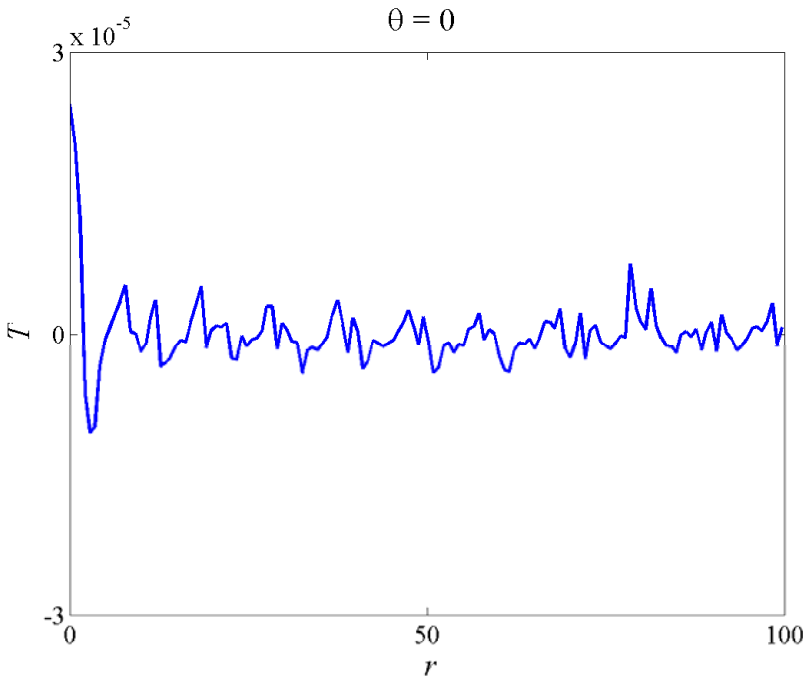

Figure 6.13(a) Scattered temperature $\hat{T}_s$ at $\theta = 0$ for $\lambda = 10/3$

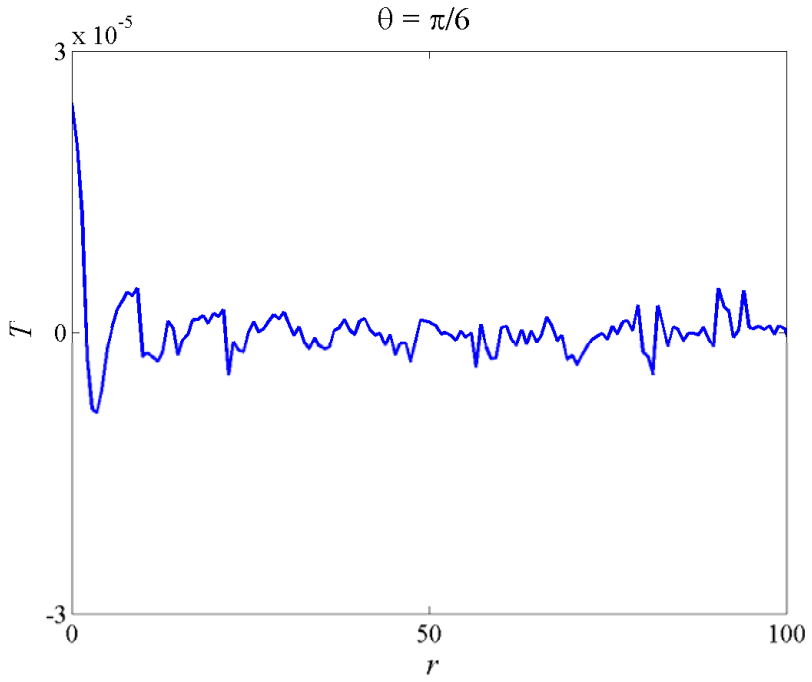

Figure 6.13(b) Scattered temperature $\hat{T}_s$ at $\theta = \pi/6$ for $\lambda = 10/3$

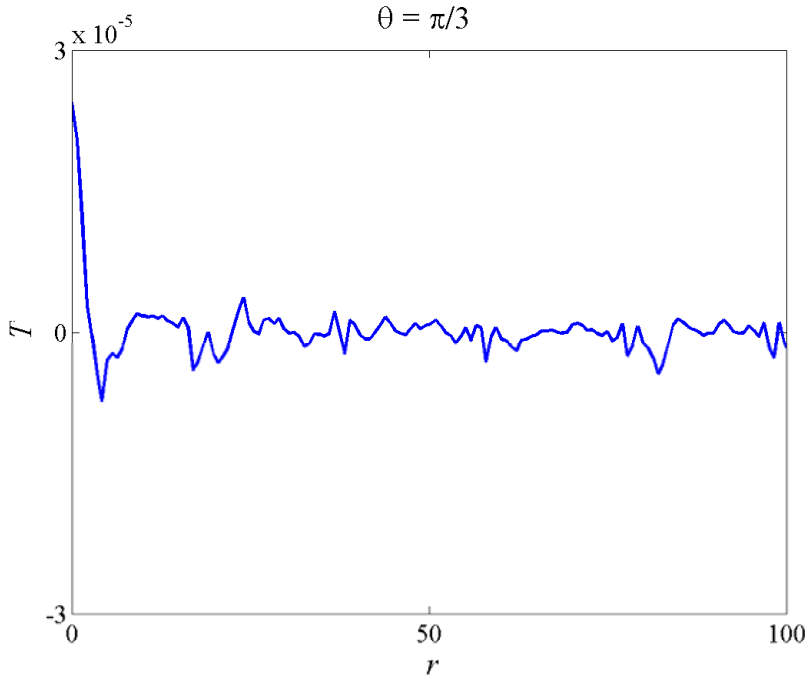

Figure 6.13(c) Scattered temperature $\hat{T}_s$ at $\theta = \pi/3$ for $\lambda = 10/3$

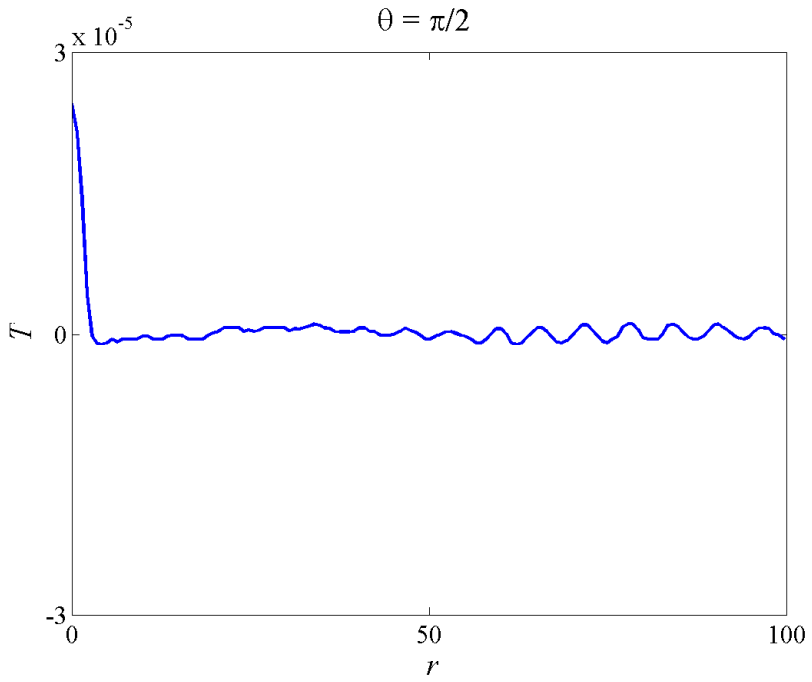

Figure 6.13(d) Scattered temperature $\hat{T}_s$ at $\theta = \pi/2$ for $\lambda = 10/3$

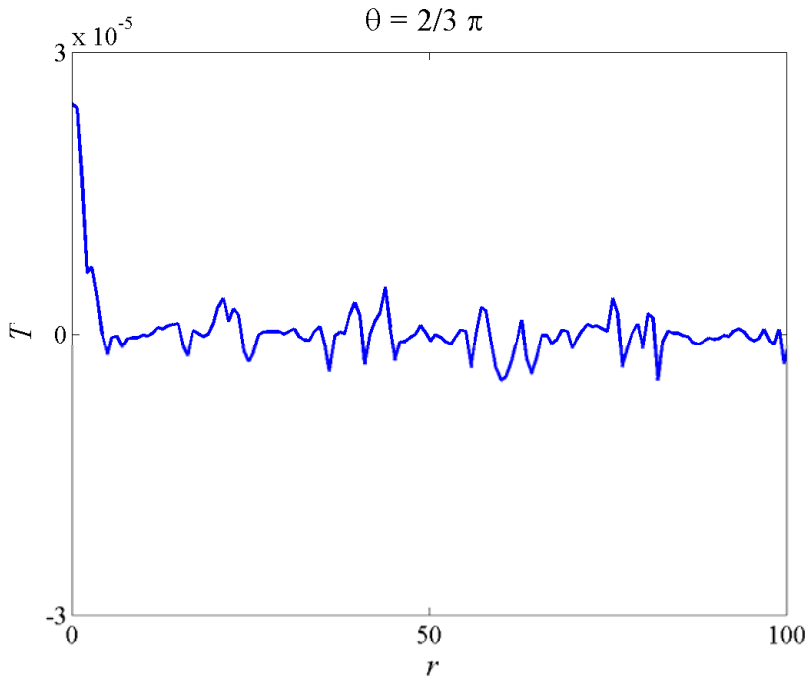

Figure 6.13(e) Scattered temperature $\hat{T}_s$ at $\theta = 2\pi/3$ for $\lambda = 10/3$

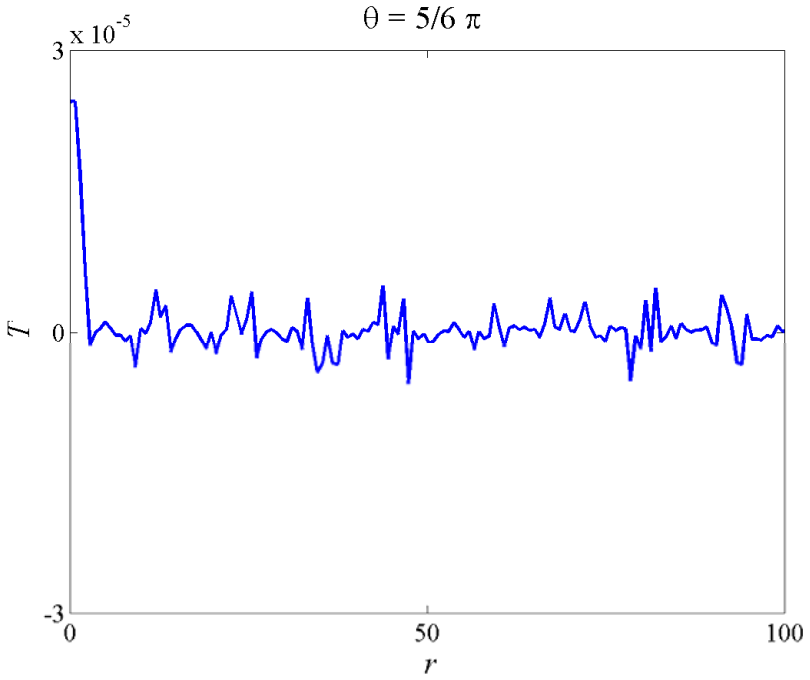

Figure 6.13(f) Scattered temperature $\hat{T}_s$ at $\theta = 5\pi/6$ for $\lambda = 10/3$

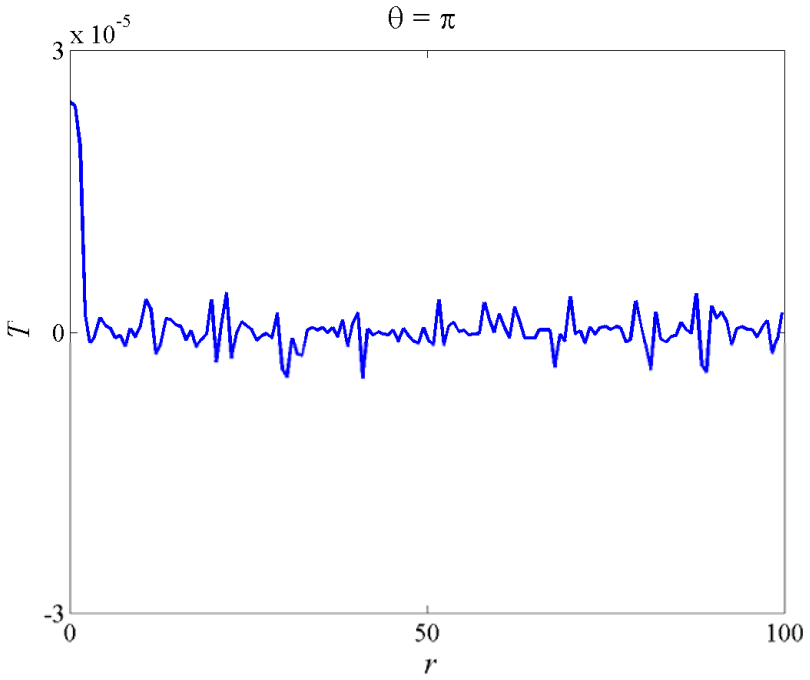

Figure 6.13(g) Scattered temperature $\hat{T}_s$ at $\theta = \pi$ for $\lambda = 10/3$

Chapter 7

Conclusions and Future Work

7.1 Summary and Conclusions

The main objective of this study is to extend the modeled Boltzmann equation (BE) to tackle direct aeroacoustic simulation (DAS) problems. In order to conduct one-step aeroacoustic simulations with the modeled BE, the unsteady Navier-Stokes (NS) equations have to be recovered from the modeled BE. On the other hand, a truly non-reflecting boundary condition should be implemented into the numerical scheme for computational aeroacoustic (CAA) studies.

Recovery of the NS equations from the modeled BE involves proper evaluation of transport coefficients including the specific heat ration, the dynamic shear viscosity and the thermal conductivity, γ, μ and κ, respectively. A two-relaxation-time model for one-step CAA studies has been proposed by Li et al. (2006), with remedies to allow the recovery of the NS equations from the modeled BE. Thus formulated, their model allows γ and μ to be recovered correctly; hence, the Mach number and the Reynolds number were correctly calculated. In order to complete the recovery of the full set of NS equations from the modeled BE, κ and the Prandtl number have to be recovered correctly, thus allowing the thermal effect to be replicated correctly by the modeled BE.

In this thesis, a modified two-relaxation-time modeled BE was put forward and a thorough study on two important issues has been carried out; (1)

an extensive examination of different non-reflecting boundary conditions (NRBC) for the modeled BE, and (2) inclusion of thermal effect in the modeled BE by invoking the Eucken model to properly account for heat transfer effect in non-isothermal flow problems. This latter investigation requires the solution of a benchmark problem on acoustic scattering by a distributed thermal disturbance, which is solved analytically by making appropriate approximations and the solution used to validate the improved modeled BE.

(1) An extensive examination of NRBC for the modeled BE

Four different methods for the NRBC have been implemented to a numerical scheme used to solve the modeled BE; namely, the lattice Boltzmann method (LBM). Since not many NRBC methods that are specific to the BE are available, other NRBCs that are commonly used in direct numerical simulation (DNS) schemes for DAS were tested in addition to the limited NRBC methods for the modeled BE. The NRBC methods commonly used in DNS studies of DAS are the zero-order extrapolation method (EM0), the first-order extrapolation method (EM1), the C^1 continuity method and the absorbing boundary condition (ABC) method. On the other hand, methods that are specific to the modeled BE are the zero f gradient method and the zero first derivative of f method. Two aeroacoustic problems were chosen as benchmarks to test the performance of these different NRBC methods. The calculated results were compared with those deduced from DNS assuming a relatively large computational domain and with no boundary treatments. Among all NRBCs tested, the ABC was found to be most effective in its

treatment of the exiting waves and the numerical results are in good agreement with the reference DNS solutions obtained with a large computational domain with no boundary treatment. This part of the thesis work indicates that for DAS studies using a modeled BE, it is not necessary to invoke NRBC designed specifically for the modeled BE. Rather, the ABC, which is designed for DAS studies using NS equations, is found to be equally applicable for the modeled BE.

(2) Inclusion of thermal effect in the modeled BE

Based on the two-relaxation-time model proposed by Li et al. (2006), the set of Navier-Stokes equations were recovered by invoking Eucken model. Thus formulated, κ as well as γ and μ were recovered correctly and therefore the dimensionless numbers *M*, *Re* and *Pr* in the NS equations were predicted correctly as solutions of the modeled BE.

The improved modeled BE is used to solve a thermal-acoustic scattering problem in order to demonstrate its ability to resolve thermal effect. Instead of using the LBM to solve the improved modeled BE, an alternative numerical scheme was adopted; this is the the gas-kinetic scheme of Xu (2003). The thermal-acoustic scattering problem attempted is a relatively simple problem where a plane pressure pulse was scattered by a distributed thermal disturbance. Only the two-dimensional problem was considered. This is due to the fact that for this simplified version of the scattering problem an analytical solution could be obtained by asymptotic analysis for validation of the numerical solution of the improved modeled BE. One key simplifying assumption of the analytical solution is the decoupling of the acoustic

propagation from the heat conduction problem. This assumption was not necessary in the gas-kinetic scheme used to solve the modeled BE. Therefore, it is expected that the interaction behavior could be resolved by the modeled BE approach. Two limiting cases, a short ($\lambda = 1$) and a long ($\lambda = 10$) wavelength limit case, were studied. The numerical solutions were compared to the analytical solutions obtained by asymptotic analysis. Due to the limited time frame of this thesis work, detailed study on the NRBC for the gas-kinetic scheme could not be conducted. Only the well known Riemann invariants method was adopted as the NRBC in the scattering study.

It is found that, for the short wavelength limit, the modeled BE and analytical results were in very good agreement with each other. The gas-kinetic scheme revealed not only the thermal resolving ability, but also the non-linear thermal-acoustic interaction which can only be resolved by one-step aeroacoustic simulations. However, due to the fact that the NRBC based on Riemann invariants is only transparent to outgoing waves propagating perpendicularly towards the open boundaries, the numerical solutions for the long wavelength limit were contaminated by reflected waves from the numerical boundaries. The fundamental scattering pattern for this long wavelength case was revealed but quantitative comparison could not be made.

7.2 Future Work

In this thesis, the modeled BE has been made capable of recovering the unsteady Navier-Stokes equations with correct transport coefficients and thus the corresponding dimensionless numbers. This is accomplished by invoking physical models, such as Sutherland law and Eucken model. The improved

modeled BE as a one-step aeroacoustic simulation scheme has been verified by several benchmark problems, where its ability to resolve aeroacoustic waves, as well as thermal-acoustic interaction have been validated.

If the modeled BE were to be extended to practical CAA studies, several improvements on this modeled BE should be implemented.

1. The gas-kinetic scheme used to solve the modeled BE in the present study is able to resolve thermal-acoustic interaction for short wavelength acoustic waves; however, its ability to resolve long wavelength cases was limited because the simulated acoustic field was contaminated by the reflected wave from the open boundary based on Riemann invariants. The reason is that the Riemann invariants boundary condition is not truly non-reflecting for incident waves that have substantial deviation from normal waves. Despite the fact that an extensive study for different non-reflecting boundary conditions (NRBC) has been carried out for the LBM (one of the numerical scheme solving modeled BE), an equivalent study has not been conducted for the gas-kinetic scheme. Therefore, it is suggested that a thorough NRBC study should be carried out for the gas-kinetic scheme. Up to this level of understanding of the gas-kinetic scheme, the conventional open boundary conditions can be extended for this scheme. For example, absorbing boundary conditions (Engquist and Majda 1977, Ta'asan and Nark 1995, Freund 1997). The reason is that the primary governing equations to be solved in the gas-kinetic scheme is the macroscopic transport equations (see chapter 6),

although the mesoscopic variable, the distribution function is involved in the gas-kinetic scheme.

2. As mentioned in Chapter 5, there are three fundamental modes of motion in a slightly disturbed heat conducting gas. So far the modeled BE has only been validated against a thermal-acoustic interaction problem. It should be further tested against other thermal-aero-acoustic interaction problems.

3. Theoretically, the NS equations are recovered from the modeled BE with correct transport coefficients and the associated dimensionless numbers. At present, only cases with moderate *M, Re* and *Pr* have been investigated. More cases with a wide range of *M, Re,* and *Pr* should be carried out for the modeled BE to further validate the proposed scheme.

4. So far only simple problems in two-dimensions have been studied. Based on the validated 2-D scheme, it should be feasible to extend the modeled BE to a 3-D scheme, in order to tackle more complicated problems, e.g. aeroacoustic problems near airports, etc.

5. A proper wall boundary condition should be included for investigation of realistic CAA problems with simple and complex geometries.

References

Abe, T., "Derivation of the Lattice Boltzmann Method By Means of Discrete Ordinate Method for the Boltzmann Equation," *Journal of Computational Physics*, Vol. 131, 1997, pp.241-246.

Abramowitz, M. and Stegun, I. A., *Handbook of Mathematical Functions*, Dover, 1965.

Alexander, F. J., Chen, S. and Sterling, J. D., "Lattice Boltzmann Thermohydrodynamics," *Physical Review E*, Vol. 47, No. 4, April 1993, 2249-2252.

Bass, H. E., "Absorption of Sound by Air: High Temperature Prediction," *The Journal of Acoustical Society of America*, Vol. 69, No. 1, 1981, pp. 124-138.

Bennett, A. F., Taylor, J. R., and Chua, B. S., "Lattice Boltzmann Open Boundaries for Hydrodynamic Models," *Journal of Computational Physics*, Vol. 203, No. 1, 2005, pp. 89–111.

Berthet , R., Astruc, D. and Estivalèzes, J. L., "Assessment of Numerical Boundary Conditions for Simulation of Sound Scattering by Vorticity," *6th AIAA/CEAS Aeroacoustics Conference and Exhibition,* AIAA-2000-2005, Lahaina, HI, U.S., 2000.

Bhatnagar, P., Gross, E. P., and Krook, M. K., "A Model for Collision Processes in Gases, I. Small Amplitude Processes in Charged and Neutral One-Component Systems," *Physical Review*, Vol. 94 No. 3, 1954, pp. 515-525.

Bogey, C., Baily, C., and Juvé, D., "Computation of Flow Noise Using Source Terms in Linearized Euler's Equation," *AIAA Journal*, Vol. 40, No. 2 2002, pp. 235-243.

Candel, S. M., "Numerical Solution of Wave Scattering Problems in the Parabolic Approximation," Journal of Fluid Mechanics, Vol. 90, No. 2, 1979, pp. 465–507.

Cercignani, C., *The Boltzmann Equation and its Applications*, Springer-Verlag, New York, 1988.

Chapman, S., "On the Law of Distribution of Molecular Velocities, and on the Theory of Viscosity and Thermal Conduction, in a Non-Uniform Simple Monatomic Gas," *Philosophical Transactions of the Royal Society of London. Series A*, Vol. 216, 1916, pp. 279-348.

Chapman, S., "On the Kinetic Theory of a Gas. Part II: A Composite Monatomic Gas: Diffusion, Viscosity, and Thermal

Conduction," *Philosophical Transactions of the Royal Society of London. Series A*, Vol. 217, 1918, pp. 115-197.

Chapman, S., and Cowling, T. G., *The Mathematical Theory of Non-Uniform Gases*, Camridge University Press, Cambridge England, U.K., 1970.

Chen, H., Chen, S., and matthaeus, W. H., "Recovery of the Navier-Stokes Equations Using a Lattice-Gas Boltzmann Method," *Physical Review A: General Physics*, Vol. 45, 1992, pp. 5339-5342.

Chen, S., and Doolen, G. D., "Lattice Boltzmann Method for Fluid Flows," *Annual Review of Fluid Mechanics*, Vol. 30, 1998, pp. 329-364.

Chen, S., Martinez, D. and Mei, R., "On Boundary Conditions in Lattice Boltzmann Methods," *Physics of Fluids*, Vol. 8, 1996, pp. 2527–2536.

Chen, Y., Ohashi, H and Akiyama, M., "Thermal Lattice Bhatnagar-Cross-Krook Model without Nonlinear Deviations in Macrodynamic Equations," *Physics Review E*, Vol. 50, No. 4, October 1994, pp. 2776-2783.

Colonius, T. and Lele, S. K., "Computational aeroacoustics: progress on nonlinear problems of sound generation," *Progress in Aerospace Sciences*, Vol. 40, 2004, pp. 345-416.

Colonius, T., Lele, S. K., and Moin, P., "Boundary Conditions for Direct Computation of Aerodynamic Sound Generation," *AIAA Journal*, Vol. 31, No. 9, 1993, pp. 1574–1582.

Colonius, T., Lele, S. K., and Moin, P.,"The Scattering of Sound Waves by a Vortex: Numerical Simulations and Analytical Solutions," *Journal of Fluid Mechanics*, Vol. 260, 1994, pp. 271-298.

Cornubert, R., d'Humières, D and Levermore, D.,"A Knudsen Layer Theory for Lattice Gases," *Physica D*, Vol. 47, 1991, pp. 241-259.

Danforth, A. L., and Long, L. N., "Nonlinear Acoustic Simulations Using Direct Simulation Monte Carlo," *Journal of the Acoustical Society of America*, Vol. 116, No. 4, 2004, pp. 1948–1955.

Engquist, B., and Majda, A., "Absorbing Boundary Conditions for the Numerical Simulation of Waves," *Mathematics of Computation*, Vol. 31, July 1977, pp. 629–651.

Enskog, D., "Kinetische Theorie der Vorgänge in Mässig Verdünnten Gasen," Doctoral dissertation, Uppsala University, Uppsala, Sweden, 1917.

Eu, B. C., "Relations between Transport Coefficients and Their Density and Temperature Dependence," *The Journal of Physical Chemistry A*, Vol. 110, No. 3, 2006, pp.831-842.

Eucken, A, "Über das Wärmeleitvermögen, die spezifische Wärme und die innere Reibung der Gase," *Physikalische Zeitschrift*, XIV, 1913. pp. 324-332.

Farouk, B., Oran, E. S. and Fusegi, T., "Numerical Study of Thermoacoustic Waves in an Enclosure," *Physics of Fluids*, Vol. 12, No. 5, 2000.

Ferziger, J. H., and Kaper, H. G., *Mathematical Theroy of Transport Processes in Gases*, North-Holland, Amsterdam, 1972.

Ferziger, J. H., "Low-Frequency Acoustic Scattering from a Trailing Vortex," *The Journal of Acoustical Society of America*, Vol. 56, 1974, pp. 1705-1707.

Ffowcs Williams, J. E., and Hawkings, D. L., "Sound Generation by Turbulence and Surfaces in Arbitrary Motion," *Philosophical Transactions of Royal Society of London, Series A: Mathematical and Physical Sciences*, Vol. 264, No. 1151, 1969, pp. 321-342.

Ford, R. and Llewellyn Smith, S. G., "Scattering of Acoustic Waves by a Vortex," *Journal of Fluid Mechanics*, Vol. 386, 1999, pp. 305-328.

Freund, J. B., "Proposed Inflow/Outflow Boundary Condition for Direct Computation of Aerodynamic Sound," *AIAA Journal*, Vol. 35, 1997, pp. 740–742.

Frisch, U., d'Humières, D., Hasslacher, B., Lallemand, P., Pomeau, Y., and Rivet, J. -P.,"Lattice Gas Hydrodynamics in Two and Three Dimensions," *Complex Systems*, Vol. 1, 1987, pp. 649-707.

Frisch, U., Hasslacher, B., and Pomeau, Y., "Lattice-Gas Automata for the Navier-Stokes Equation," *Physical Review Letters*, Vol. 56, No. 14, 1986, pp. 1505-1508.

Gaitonde, D. V. and Visbal, M. R., "*Further Development of a Navier- Stokes Solution Procedure Based on Higher-Order Formulas*," AIAA Paper 99-C0557, 1999.

Georges, T. M., "Acoustic Ray Paths through a Model Vortex with a Viscous Core," *The Journal of Acoustical Society of America*, Vol. 51, 1972, pp. 206-209.

Ghia, U., Ghia, K. N., Shin, C. T., "High Resolution for incompressible flow Using the Navier-Stokes Equations and a Multigrid Method," *Journal of Computational Physics*, Vol. 48, Issue 3, 1982, pp. 387-411.

Giles, M. B., "Nonreflecting Boundary Conditions for Euler Equation Calculations," *AIAA Journal*, Vol. 28, No. 12, 1990, pp. 2050–2058.

Guo, Z., and Zhao, T. S., "Explicit Finite-Difference Lattice Boltzmann Method for Curvilinear Coodinates," *Physical Review E (Statistical Physics, Plasmas, Fluids, and Related Interdisciplinary Topics)*, Vol. 67, No. 6, 2003, pp. 1–12.

Hardin, J. C., and Pope, D. S., "An Acoustic/Viscous Splitting Technique for Computational Aeroacoustics," *Theoretical and Computational Fluid Dynamics*, Vol. 6, No. 5-6, 1994, p. 323-340.

Harris, S., *An Introduction to the Theory of the Boltzmann Equation*, Dover, New York, 1999.

He, X., and Luo, L. S.,"A priori derivation of the lattice Boltzmann equation," *Physical Review E*, Vol. 55, 1997, pp. 6333-6336.

Howe, M. S., "Contributions to the Theory of Aerodynamic Sound, with Application to Excess Jet Noise and the Theory of the Flute," *Journal of Fluid Mechanics*, Vol. 71, 1975, pp. 625-673.

Hu, F. Q., "A Stable, Perfectly Matched Layer for Linearized Euler Equations in Unsplit Physical Variables," *Journal of Computational Physics*, Vol. 173, No. 2, 2001, pp. 455–480.

Inamuro, T., Yoshino, M. and Ogino, F., "A Non-Slip Boundary Condition for Lattice Boltzmann Simulations," *Physics of Fluids*, Vol. 7, 2928-2930.

Kang, H. –K., Ro, K.-D., Tsutahara, M., and Lee, Y. –H., "Numerical Prediction of Acoustic Sounds Occuring by the Flow Around a Circular Cylinder," *KSME International Journal*, Vol. 17, No. 8, 2003, pp. 1219-1225.

Kim, J. W. and Lee, D. J., "Generalized Characteristic Boundary Conditions for Computational Aeroacoustics," *AIAA Journal*, Vol. 38, 2000, pp. 2040-2049.

Kogan, M. N., *Rarefied Gas Dynamics*, New York Plenum Press, 1969.

Lallemand, P., and Luo, L.-S., "Theory of the Lattice Boltzmann Method: Dispersion, Dissipation, Isotropy, Galilean Invariance, and Stability," *Physical Review E (Statistical Physics, Plasmas, Fluids, and Related Interdisciplinary Topics)*, Vol. 61, No. 6, 2000, pp. 6546–6562.

Lallemand, P. and Luo, L. S.," Theory of the Lattice Boltzmann Method: Acoustic and Thermal Properties in Two and Three Dimensions," *Physical Review E*, Vol. 68, 2003, Paper no. 036703.

Lele, S. K., "Compact finite schemes with spectral-like resolution," *Journal of Computational Physics*, Vol. 103, No. 1, 1992, pp. 16-42.

Landa, P. S., *Nonlinear Oscillations and Waves in Dynamical Systems*, Kluwer Academic Publishers, Netherlands, 1996.

Leung, R. C. K., Li, X. M., and So, R. M. C. "Comparative Study of Nonreflecting Boundary Condition for One-Step Duct Aeroacoustic Simulation," *AIAA Journal*, Vol. 44, No. 3, 2006, pp. 664–667.

Li, X. M., "Computational Aeroacoustics Using Lattice Boltzmann Method," Ph.D. Thesis, Dept. of Mechanical Engineering, Hong Kong Polytechnic University, Hong Kong, 2006.

Li, X. M., Leung, R. C. K., and So, R. M. C., "One-Step Aeroacoustics Simulation Using Lattice Boltzmann Method," *AIAA Journal*, Vol. 44, No. 1, 2006, pp. 78-89.

Li, X. M., So, R. M. C., and Leung, R. C. K., "Propagation Speed, Internal Energy and Direct Aeroacoustic Simulation Using LBM," *AIAA Journal*, Vol. 44, No. 12, 2006, pp. 2896–2903.

Lighthill, M. J., "On Sound Generated Aerodynamically:I. General Theory," *Proceedings of the Royal Society of London, Series A: Mathematical and Physical Sciences*, Vol. 211, No. 1107, 1952, pp. 564-587.

Loh, C. Y., "On a Non-Reflecting Boundary Condition for Hyperbolic Conservation Laws," *AIAA Paper* 2003-3975, 2003.

Loh, C. Y., and Jorgenson, P. C. E., "A Robust Absorbing Boundary Condition for Compressible Flows," *AIAA Paper* 2005-4716, 2005.

Maier, R., Bernard, R. S. and Grunau, D. W., "Boundary Conditions for the Lattice Boltzmann Method," *Physics of Fluids*, Vol. 8, 1996, pp. 1788–1801.

Mallick, S., Shock, R., and Yakhot, V., "Numerical Simulation of the Excitation of a Helmholtz Resonator by a Grazing Flow," *Journal of the Acoustical Society of America*, Vol. 114, No. 4, 2003, pp. 1833–1840.

Mandal, J. C., and Deshpande, S. M., "Kinetic Flux Vector Splitting for Euler Equations," *Computers and Fluids*, Vol. 23, No. 2, 1994, pp. 447-478.

Mawardi, O. K., "Aero-Thermoacoustics - The Generation of Sound by Turbulence and by Heat Processes," *Reports on Progress in Physics*, Vol. 19, 1956, pp. 156-187.

Maxwell, J. C., "On the Dynamical Theory of Gases," *Philosophical Transactions of the Royal Society of London*, Vol. 157, 1867, pp.49-88.

McNamara, G. R., Garcia, A. L. and Alder, B. J., "Stabilization of Thermal Lattice Boltzmann Models," *Journal of Statistical Physics*, Vol. 81, 1995, pp. 395-408.

McNamara, G. R., and Zanetti, G.,"Use of the Boltzmann Equation to Simulate Lattice-Gas Automata," *Physical Review Letters*, Vol. 61, 1988, pp.2332-2335.

Morse, P. M. and Uno Ingard, K., *Theoretical Acoustics*, McGraw-Hill, USA, 1968.

Müller, E. A. and Matschat, K. R.," The Scattering of Sound by a Single Vortex and By Turbulence," *Technical Reports – Max-Planck-Institut für Strömungsforschung, Göttingen*, 1959.

Noble, D. R., Chen, S., Georgiadis, J. G. and Buckius, R. O., " A Consistent Hydrodynamic Boundary Condition for the Lattice Boltzmann Method," *Physics of Fluids*, Vol. 7, 1995, pp. 203-209.

O'Shea, S., "Sound Scattering by a Potential Vortex," *Journal of Sound and Vibration*, Vol. 43, 1975, pp. 109-116.

Pamler, B. J., and rector, D. R., "Lattice Boltzmann Algorithm for Simulating Thermal Flow in Compressible Fluids," *Journal of Computational Physics*, Vol. 161, No. 1, 2000, pp. 6546-6562.

Philippi, P. C., Hegele, L. A., dos Santos, L. O. E., and Surmas, R., "From the Continuous to the Lattice Boltzmann Equation: The Discretization Problem and Thermal Models," *Physical Review E (Statistical Physics, Plasmas, Fluids, and Related Interdisciplinary Topics)*, Vol. 73, May 2006, p. 056702.

Poinsot, T. J. and Lele, S. K., "Boundary Conditions for Direct Simulations of Compressible Viscous Flows," *Journal of Computational Physics*, Vol. 101, 1992, pp. 104–129.

Prendergast, K. H., and Xu, K., "Numerical Hydrodynamics from Gas-Kinetic Theory," *Journal of Computational Physics*, Vol. 109, 1993, pp. 53-66.

Pullin, D. I., "Direct Simulation Methods for Compressible Inviscid Ideal-Gas Flow," *Journal of Computational Physics*, Vol. 34, 1980, pp. 231-244.

Qian, Y. H., d'Humières, D., and Lallemand, P., "Lattice BGK Models for Navier-Stokes Equation," *Europhysics Letters*, Vol. 17, No. 6, 1991, pp. 479-484.

Rah, K. and Eu, B. C., "Theory of Thermal Conductivity of Dense Simple Fluids," *Journal of Chemical Physics,* Vol. 115, No. 20, 2001, pp. 9370-9381.

Rayleigh, J. W. S., *The Theory of Sound*, Dover Publisher, New York, 1945.

Reider, M. B., and Sterling, J. D., "Accuracy of Discrete-Velocity BGK Models for the Simulation of the Incompressible Navier-Stokes Equations," *Computers and Fluids*, Vol. 24, No. 4, 1995, pp. 459-467.

Ricot, D., Maillard, V., and Bailly, C., "Numerical Simulation of Unsteady Cavity Flow Using Lattice Boltzmann Method," *AIAA Paper* 2002-2532, 2002.

Rijke, P. L.**,** "Notiz über eine neue Art, die in einer an beiden Enden offenen Röhre enthaltene Luft in Schwingungen zu versetzen," *Annalen der Physik*, Vol. 183, Issue 6, 1859, pp. 339-343.

Roe, P. L., "Characteristic-Based Schemes for the Euler Equations," *Annual Review of Fluid Mechanics*, Vol. 18, 1986, pp. 337–365.

Shan, X., "Simulation of Rayleigh-Bénard Convection Using a Lattice Boltzmann Method," *Physical Review E*, Vol. 55, No.3, 1997, pp. 2780-2788.

Shen, W. Z., and Sorensen, J. N., "Aeroacoustic Modeling of Low-Speed Flows," *Theoretical and Computational Fluid Dynamics*, Vol. 13, No. 4, 1999, pp. 271-289.

Skordos, P. A., "Initial and Boundary Conditions for the Lattice Boltzmann Method," *Physical Review E*, Vol. 48, No. 6, 1993, pp. 4823-4842.

Su, M., Xu, K., and Ghidaoui, M. S., "Low-Speed Flow Simuation by the Gas-Kinetic Scheme," *Journal of Computational Physics*, Vol. 150, 1999, pp. 17-39.

Succi, S., *The lattice Boltzmann Equation for Fluid Dynamics and Beyond*, Oxford University Press, New York, 2001.

Sun, C., "Lattice Boltzmann Models for High Speed Flow," *Physical Review E*, Vol. 58, 1998, pp. 7283-7287.

Ta'asan, S. and Nark, D. M., "An Absorbing Buffer Zone Technique for Acoustic Wave Propagation," *AIAA Paper* 95–0146, 1995.

Tam, C. K. W., and Webb, J. C., "Dispersion-Relation-Preserving Finite Difference Schemes for Computational Acoustics," *Journal of Computational Physics*, Vol. 107, No. 2, 1993, pp. 262–281.

Teixeira, C., Chen, H. and Freed., D. M., "Multi-Speed Thermal Lattice Boltzmann Method Stabilization via Equilibrium Under-Relaxation," *Computer Physics Communications*, Vol. 129, 2000, pp. 207-226.

Trilling, L.," On Thermally Induced Sound Fields," *The Journal of the Acoustical Society of America*, Vol. 27, No. 3, 1955, pp. 425-431.

Tsutahara, M., Kataoka, T., Takada, N., Kang, H. –K., and Kurita, M.," Simulations of Compressible Flows by Using the lattice Boltzmann and the Finite Difference Lattice Boltzmann Methods," *Computational Fluid Dynamics Journal*, Vol. 11, No. 1, 2002, pp. 486-493.

Visbal, M. R., and Gaitonde, D. V., "*Very High-Order Spatially Implicit Schemes for Computational Acoustics on Curvilinear Meshes*," *Journal of Computational Acoustics*, Vol. 9, No. 4, 2001, pp. 1259–1286.

White, F. M., *Viscous Fluid Flow*, McGraw-Hill, New York, 1991.

Wilde, A., "Calculation of Sound Generation and Radiation from Instationary Flows," *Computers and Fluids*, Vol. 35, Nos. 8–9, 2006, pp. 986–993.

Wolfram, S., "Cellular Automation Fluids. 1: Basic Theory," *Journal of Statistical Physics*, Vol. 45, 1986, pp. 471-526.

Wolf-Gladrow, D. A., *Lattice-Gas Cellular Automata and lattice Boltzmann Models. An Introduction*, Springer, New York, 2000.

Woods, L. C., *An Introduction to Kinetic Theory of Gases and Magnetoplasmas,* Oxford University Press, New York, 1993.

Xu, K., "A Gas-kinetic BGK Scheme for the Navier-Stokes Equations, and Its Connection with Artificial Dissipation and Godunov Method," *Journal of Computational Physics*, Vol. 171, 2001, pp. 289-335.

Xu, K. and He, X.Y., "Lattice Boltzmann method and gas-kinetic BGK scheme in the low-Mach number viscous flow simulations," *Journal of Computational Physics*, Vol. 190, Issue 1, 2003, pp. 100-117.

Yates, J. E., "Application of the Bernoulli Enthalpy Concept to the Study of Vortex Noise and Jet Impingement Noise," *NASA Contractor Report 2987*, 1978.

Yu, D., Mei, R., and Shyy, W., "Improved Treatment of the Open Boundary in the Method of Lattice Boltzmann Equation: General Description of the Method," *Progress in Computational Fluid Dynamics*, Vol. 5, Nos. 1–2, 2005, pp. 3–12.

Ziegler, D. P., ”Boundary Conditions for Lattice Boltzmann Simulations,” *Journal of Statistical Physics*, Vol. 71, Nos. 5/6, 1993, pp. 1171-1177.

Zou, Q. and He, X., ”On Pressure and Velocity Boundary Conditions for the Lattice Boltzmann BGK Model,” *Physics of Fluids*, Vol. 9, No. 6, 1997, pp. 1591-1598.